NOVEL METHODS OF QUANTIFYING CURING INFLUENCE AND FREEZE THAW CYCLES IN THE FIELD

By

LICHUN CHEN

Bachelor of Science in Civil Engineering
Shanghai Jiao Tong University
Shanghai, China
2013

Master of Engineering in Civil Engineering
Shanghai Jiao Tong University
Shanghai, China
2016

Submitted to the Faculty of the
Graduate College of the
Oklahoma State University
in partial fulfillment of
the requirements for
the Degree of
DOCTOR OF PHILOSOPHY
May, 2022

NOVEL METHODS OF QUANTIFYING CURING INFLUENCE AND FREEZE THAW CYCLES IN THE FIELD

Dissertation Approved:

Dr. M. Tyler Ley

Dissertation Adviser

Dr. Bruce Russell

Dr. Nicholas F. Materer

Dr. Mohamed Soliman

Dr. Qiang Li

ACKNOWLEDGEMENTS

Throughout my time at Oklahoma State University, I have encountered many people that have influenced my drive to study higher education. One of the most influential is professor Dr. Tyler Ley. Dr. Ley has been my academic advisor and mentor throughout my doctoral degrees, and I want to thank him for challenging me and helping me to achieve goals within my academic career and my personal development. Thank you to my committee members, Dr. Qiang Li, Dr. Bruce Russell, Dr. Mohamed Soliman, and Dr. Nicholas F. Materer who generously agreed to serve on my doctoral committee and support the growth of this study. The professional knowledge and encouragement that they shared were truly helpful. I would also like to extend my gratitude to all my colleagues and to all the graduate and undergraduate students that helped me during my doctoral research. Lastly, thank you to my husband, Ligang Shen for supporting me in this journey.

Name: LICHUN CHEN

Date of Degree: MAY, 2022

Title of Study: NOVEL METHODS OF QUANTIFYING CURING INFLUENCE AND FREEZE THAW CYCLES IN THE FIELD

Major Field: CIVIL ENGINEERING

Abstract: This work developed a flexible resistivity sensor that provides a novel perspective to develop a deep understanding of two important problems for concrete, i.e. curing influence on concrete hydration and freeze-thaw cycles of concrete in the field. First, the resistivity sensor is designed to quantify the influence of different curing methods on hydration and subsequent related properties of the fresh concrete. A correlation between resistivity and degree of saturation (DOS), tensile strength, and porosity was established based on measured data. The work also provides guidance on the allowable delay in applying the wet curing before the properties of the concrete are compromised. The same resistivity sensor network is modified to measure the DOS, temperature, and the ice formation of concrete in the field condition. A series of samples were sent out to different field sites with various weather conditions. An equation for calculating the temperature when ice forms and thaws for samples with different DOS was obtained. The designed sensor was proven to provide a practical approach to making widespread measurements of the number of effective freeze-thaw cycles of concrete in the field. These new electrical observations offer powerful insights into liquid water movement, chemical bonding in hydration products, and the phase change with temperature.

TABLE OF CONTENTS

Chapter Page

Chapter Page

LIST OF TABLES

Table Page

Table Page

LIST OF FIGURES

Figure Page

Figure Page

Figure Page

Figure Page

CHAPTER I

INTRODUCTION

1.1 Introduction

This work developed a new data logger and flexible electrical sensors that are used to gain new insights into two important problems for concrete. First, the sensor network is used to quantify the influence of different curing methods on the moisture content, hydration, and subsequent properties of the fresh concrete, and the same sensor network is modified to measure the degree of saturation (DOS) and the ice formation in 7 field sites in 4 different states. In all of these cases, the sensor network gives us powerful insights into liquid water movement, chemical bonding in hydration products, and the phase change with temperature. These new electrical observations are combined with other traditional methods to gain even greater insights.

Curing impacts many properties of concrete such as porosity, permeability, strength, and creep [1–5]. Multiple curing methods are used in the field, however, there is not a standard and easy way to quantify the influence of curing methods. Curing impacts many properties of concrete such as porosity, permeability, strength, and creep [1–5]. Multiple curing methods are used in the field, however, there is not a standard and easy way to quantify the influence of curing methods. For example, previous studies examined the compression strength, durability, and resistance to chloride transport on hardened concrete to evaluate the curing impacts [3, 6–10].

Those examinations are time-consuming, labor-intensive, and are normally applied when concrete is over 28 days old. Although this information is useful, these methods cannot provide useful information before the concrete has been set. If these issues are caught early then they can be corrected. If there is a moisture gradient during hydration then this will generate nonuniform hydration [11]. The ability to control and avoid this would greatly benefit the concrete industry.

Pairs of electrodes were installed at 12.7 mm from the surface and then every 12.7 mm until 89 mm from the surface. This allowed a resistivity gradient to be measured to examine how the concrete would perform differently with different curing applications and in different evaporation rate environments. The change in porosity, DOS, splitting tensile strength, and diffusion coefficient were also investigated on the same mixture at comparable depths to the resistivity measurements so that direct comparisons could be made between the resistivity and physical measurements. The results suggest that the sample's DOS, porosity, and tensile strength can be correlated to resistivity. This means that resistivity measurements could be used to provide insights into the properties of the sample.

Concrete can be damaged when there is a high DOS and freeze-thaw cycles occur. Previous freeze-thaw studies have shown that critical DOS exists (78%-91%), above which freeze-thaw damage will begin to initiate [12, 13]. The DOS and freezing times are determined by the weather condition in the field. This indicates that not all weather conditions impact the concrete equally. However, lab experiments such as ASTM C666 [14] are typically conservative but they do not accurately represent the DOS and freezing rate of structures in the field. This work aims to monitor the freeze-thaw cycles of concrete in different field environments and correlates the weather condition of different regions to concrete freeze-thaw cycles. This work uses a similar sensor setup to the curing test but it measures the DOS, temperature, and ice formation simultaneously of concrete in 7 field sites in 4 states. The data obtained in this work is useful because the weather is not the same everywhere and this research provides information on how

different types of weather affect freeze-thaw cycles in the field. The work can be extended to make many practical tools to tailor the design of concrete according to real weather conditions and to create improved freeze-thaw models.

1.2 Research Objectives

The main tasks are:

- Chapter 2: Measuring the impact of air, sealed, and wet curing on mortar samples at different depths over the first 72h of hydration using electrical resistivity. The resistivity correlates with the porosity, DOS, and tensile strength test results and provides new insights into different methods of curing that have never been observed.
- Chapter 3: Investigating the influence of wet curing on concrete applied at different times in different evaporative environments using resistivity, porosity, DOS, and diffusion coefficient, to determine the allowable delay in applying the wet curing on the concrete surface before the concrete performance is compromised.
- Chapter 4: This chapter uses the developed sensor network to simultaneously measure the DOS, ice formation, and temperature of mortar samples placed at two locations with different weather conditions in the state of Oklahoma. The effective freeze-thaw cycles of the two locations were evaluated and summarized in the time range from Nov. 2019 to April 2020. This chapter established the methods to determine effective freeze-thaw cycles and makes some important observations that are used in chapter 5.
- Chapter 5: The effective freeze-thaw cycles of the concrete specimens in 7 fields in 4 states were summarized and compared in the time range from 2020 to 2021. The weather station information was combined with the sensor measurements to determine the freeze-thaw cycles of the field samples. This chapter set up the method of using the weather station information to evaluate freeze-thaw cycles.

CHAPTER II

USING ELECTRICAL RESISTIVITY TO PREDICT EARLY AGE DOS AND TENSILE STRENGTH OF MORTAR

2.1 Introduction

The hydration reaction dissolves materials, consumes water, releases heat, and creates solid material through chemical reactions. This work examines how curing in dry air, sealed conditions, and wet curing changes the degree of saturation or moisture level as well as the tensile strength of the concrete. This is determined by measuring the electrical bulk resistivity from an alternating current of a known frequency. This work investigates changes caused by drying by comparing the resistivity at different distances from the surface. These differences in resistivity correlate to changes in the measured porosity, degree of saturation, and tensile strength. This shows that resistivity is an elegant, non-destructive, economical, rapid, and quantitative measurement that provides important insights into curing mortar mixtures for controlled systems.

The purpose of curing is to minimize moisture loss and retain enough heat to promote the hydration reaction [1, 2]. Curing impacts the formation of hydration products and the development of the microstructure. The microstructure is essential to the physical properties such as porosity, permeability, strength, shrinkage, and creep [3–5]. As a result, it would be valuable to have a low-cost method that could be used to evaluate the effectiveness of curing.

Studies have investigated the influence of different curing methods such as wet curing and air curing on the compression strength, durability, and resistance to chloride transport [3, 6–10, 15]. A study by Hajibabaee [10] has shown that wet curing increases the resistance to ingress of external chemicals compared with air curing or curing compounds. However, those studies were carried out on concrete samples after 28 d of hydration. While this work is useful, more information is needed about changes in the first 72 h of hydration. Also, more information is needed to determine how curing impacts the sample over the depth with time. Studies have shown that a moisture gradient forms with a drying surface of the sample and this moisture difference will further generate non-uniform hydration and therefore a different microstructure of the material [11]. As a result, the influence of curing at the surface is of great importance to the ultimate properties of the materials.

Many studies have used electrical resistivity to measure the process of cement hydration [16–21]. Previous work monitored the electrical resistivity of cement paste during the first 30 h of hydration and showed that resistivity could be used to follow the stages of hydration of cement paste and also give insights into hydration product formation [18]. A study by Xiao shows that electrical resistivity is sensitive to the pore structure change as measured by mercury intrusion porosimetry (MIP) at 2h and 24h of hydration [20]. Since the measurement of electrical resistivity is flexible, effective, and nondestructive, it may be able to be used to make continuous measurements of a sample in a simple low-cost manner [18–21]. As a result, electrical resistivity has the potential to examine curing methods and the corresponding impacts on the concrete microstructure and properties. Besides measuring the resistivity directly, the overall resistivity of composite material can also be described by the general effective media (GEM) model [22, 23] and calculated using the capillarity porosity, percolation threshold, formation factor, magnificent coefficient, for the cementitious material in question [24], however, these measurements are not

easy to obtain and at this time these measurements have not been generalized for a wide range of materials.

The goal of this study is to use electrical resistivity to make direct measurements of the influence of different curing methods on hydration and material properties over the first 72 h of hydration. The change in the porosity, degree of saturation (DOS), and the splitting tensile strength over the first 72 h of hydration are investigated for air, sealed, and wet curing methods at different depths of the sample. The results suggest that the DOS, porosity, and tensile strength of the sample can be correlated to the resistivity from 12h to 72h. A linear relationship between DOS and resistivity was established at different times of hydration and was applied to predict the DOS of the sample from resistivity. This means that resistivity measurements could be used to determine the effectiveness of different curing methods and provide insights into the properties of the sample.

2.2 Experimental Methods

2.2.1 Materials and Mixtures

The mortar mixture in this study was prepared according to ASTM C305 [25] with a w/cm ratio of 0.45. The mixture proportion by volume is shown in Table 2-1. The cement used in this study met the requirements of an ASTM C150 Type I Portland cement. The fine aggregate used for the mortar mixture was locally available natural sand and met the requirements of ASTM C33. The Blaine of the cement is 3560 cm^2/g and the free lime content is 1.4%. The chemical compositions of the cement are shown in Table 2-2.

Table 2-1. Mixture proportion of mortar.

	Cement	Water	Fine Aggregate	Air
Volume (%)	18.5	23.4	56.7	0.4

Table 2-2. Chemical composition of cement.

	SiO_2	Al_2O_3	Fe_2O_3	CaO	MgO	SO_3	Na_2O	K_2O	C_3S	C_2S	C_3A	C_4AF	LOI
Cement (%)	21.1	4.8	3.1	64.5	2.33	3.2	0.17	0.58	50	23	7	9	2.6

2.2.2 Electrical Resistivity Test

The plastic cylinder molds have a diameter of 152.4 mm and were 228.6 mm in height. The cylinders used seven layers of 4-40 threaded stainless steel rods (2.8 mm in diameter, and 40 threads per 25.4 mm). Each layer used two rods with a horizontal spacing of 92.7 mm and a vertical spacing of 12.7 mm. The steel rods were installed through the molds and were stabilized and sealed with glue before the mortar was placed. The configuration of the specimen is shown in Figure 2-1. Mortar was used to fill the mold to 203.2 mm in height. The top 25.4 mm was not filled to allow different curing methods to be applied. The mortar was placed in three layers. For each layer, the sample was consolidated for 10 s with a vibrating table at a frequency of 60 Hz to remove entrapped air and to promote a good bond with the threaded rod.

During hydration, water is consumed and the sample shrinks [26]. This volume change may form a gap between the mold and the edge of the sample. To ensure that the drying is only from the top of the sample and not from the edges, the edge of the fresh mortar was sealed with plastic wrap and covered by mortar. More details can be found in Appendix A.

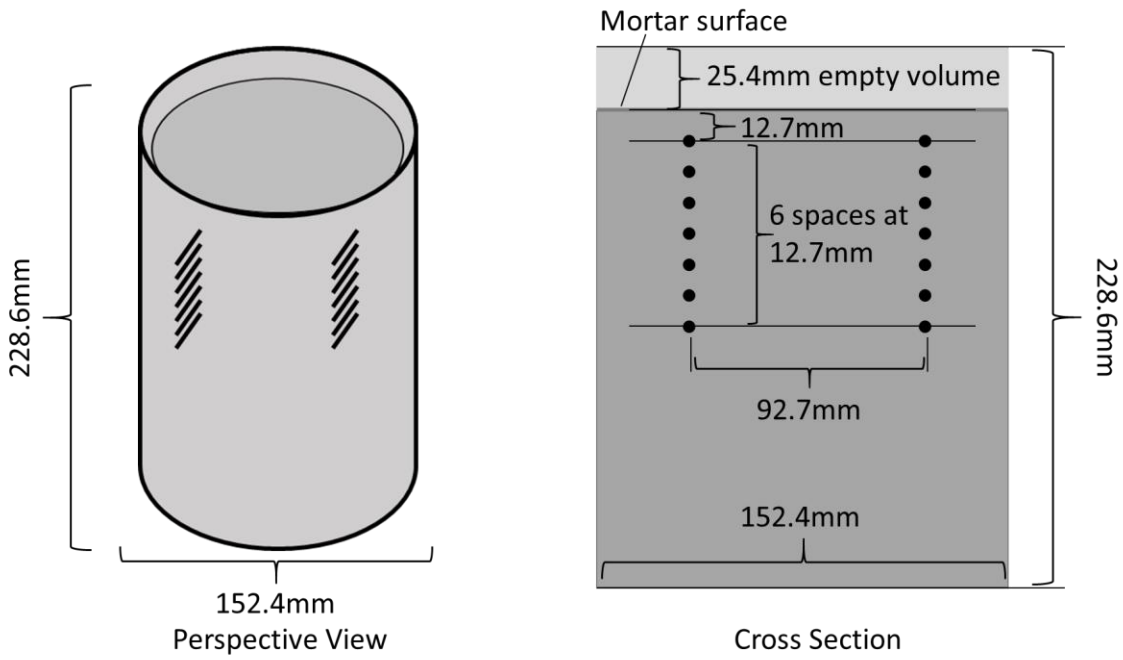

Figure 2-1. Configuration of the mortar sample for resistivity measurement.

This study investigated wet curing, sealed curing, and air curing. All three curing methods were conducted in an environmental chamber with a temperature of 23°C and humidity of 50%.

After the samples were cast into molds, curing methods were applied on the surface of the sample. In the wet curing, three layers of water-soaked burlap were placed on the surface and then the surface of the mold was sealed with aluminum tape. Every day the burlap was removed and soaked with water and replaced on top of the sample. In the sealed curing, the mold was covered with aluminum foil and sealed with aluminum tape to prevent moisture loss. The air curing method leaves the sample open to the 50% RH environment.

The resistivity was measured between the rods every 10 minutes through the hydration process. The circuit for the resistivity measurement was programmed with the Arduino platform. An Arduino Mega 2560 was used as the central processor with a 12-Bit impedance converter AD5933. In this research, a frequency of 30 kHz was used. This was chosen because at this

frequency the imaginary part of the impedance is close to zero. The system was calibrated with a 100-ohm resistor. The calibration process was to calculate the Gain Factor of the system based on a known resistor. The Gain Factor can then be used to calculate the resistivity in future measurements. The detailed calculations for these measurements are included in Appendix B.2. Five multiplexers were used to measure 80 channels simultaneously. The results were recorded on an SD card and retrieved for analysis. More details about the additional hardware and the raw data process of impedance can be found in Appendix B.1.

Since the frequency range selected has forced the imaginary impedance to close to 0, the measured impedance is also called the bulk resistance of the mortar sample. The unit of the measured bulk resistance is the ohm. To get the resistivity of the mortar sample, Equation 2-1 was used.

$$Resistivity\ (K\Omega * cm) = bulk\ resistance\ (\Omega) * A\ (mm2)\ /\ L\ (mm)/10000 \quad \text{Equation 2-1}$$

In Equation 2-1, A is assumed to be the rectangular cross-sectional area of the electrode perpendicular to the signal. The area is taken as 338.8 mm^2, since the electrode is 2.8 mm in diameter and approximately 120.96 mm long. The distance between the electrodes, L, is 92.7 mm.

2.2.3 Mass Change

The mass of the wet, sealed, and air curing samples over the first 72 h of hydration was measured and recorded every hour. The percentage of mass change was then obtained with Equation 2-2.

$$\%Mass\ Change = \frac{M_n - M_i}{M_i} \times 100 \quad \text{Equation 2-2}$$

2.2.4 Porosity and Degree of Saturation (DOS) Test

The porosity and degree of saturation (DOS) [27] are investigated to support the resistivity measurements. The porosity illustrates the microstructure development, and the DOS shows the amount of moisture within the sample. The DOS is a critical factor in promoting early hydration within the sample [28–32]. Other research shows that hydration ceases at a relative humidity of about 80% due to negative capillary pressure that opposes the reaction [33].

The mortar samples for the porosity and DOS measurement were cast into tubes of 25.4 mm in diameter by 114.3 mm tall. Each tube was filled with three layers of mortar. The mortar was from the same mixture as the one for the resistivity measurement. The wet cured DOS samples were stored in a fog room with a constant humidity of 100% and temperature of 23°C with its surface open to the environment. This is because the surface area of the container is too small to apply wet burlap. The sealed curing and air curing were conducted in an environment with 50% humidity and 23°C temperature. In the sealed curing, the sample top was sealed with the lid for the tube.

The porosity and DOS were measured when the samples had hydrated for 12 h, 24 h, 48 h, 72 h, and 96 h. Each curing method used 3 samples for this test. When the sample reached the designated hydration time, it was demolded and cut into 3 segments that were each 38.1 mm tall. This means that the distance to the midpoint of each segment was 19.1 mm, 57.2 mm, and 95.3 mm from the sample surface. This was done so that the porosity and DOS of each segment could be compared to the resistivity measurements at similar depths.

2.2.4.1 Determining the porosity and degree of saturation (DOS)

The porosity and DOS were determined by ASTM C642 with some minor changes where the samples were saturated within a vacuum chamber at a pressure of 37mmHg±5mmHg instead of boiling in water. Equation 2-3 and Equation 2-4 were used to calculate the porosity and degree of

saturation (DOS), where W_i is the initial weight of the sample, W_d is the oven-dried weight at 110 ºC, W_{sa} is the saturated surface dried (SSD) weight, W_{su} is the weight of the sample while the sample is suspended in water, it's equal to the difference between the sample weight and its buoyant force.

$$Porosity = \frac{W_{sa} - W_d}{W_{sa} - W_{su}} \times 100 \quad \text{Equation 2-3}$$

$$DOS = \frac{W_i - W_d}{W_{sa} - W_d} \times 100 \quad \text{Equation 2-4}$$

2.2.5 Splitting Tensile Strength

The splitting tensile strength test is performed according to the previous work by Robertson et al. [34] and Dickey [35]. The detailed calculation of the strength and assumptions can be found in Appendix D. The mortar samples for splitting tensile strength were cast into 152.4 mm in diameter by 76.2 mm tall plastic cylinders. Metal plates were fixed into the mold to form 2 notches with a 30° angle at the sample surface along its length shown in Figure 2-2 (a). The mold was filled in 2 layers and vibrated for 10 s on the vibration table at 60 Hz. The samples were cured the same way as the resistivity samples.

After the mortar sample was hydrated for 72 h, the sample was demolded and split with a hydraulic press as shown in Figure 2-2 (b). The loading platen has the same dimensions as the notches. The splitting test was conducted in this way because the sample failure is caused by the tension forces caused by the loading platen being pushed in compression and pushing on the angled inserts. The platen was loaded at a rate of 2000 N/min. Each curing method used 5 samples for this test. The samples that did not split at the notches were excluded from the strength calculation. Calculation details are included in Appendix D.

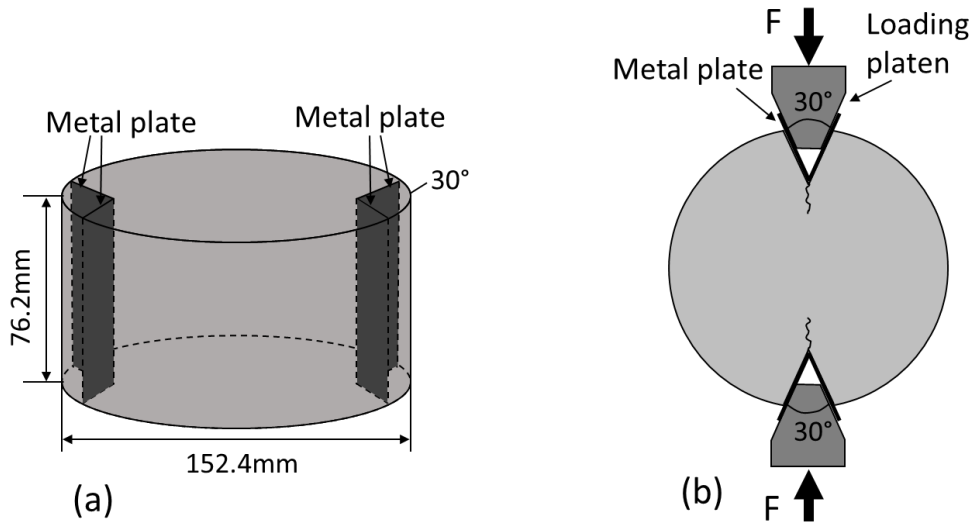

Figure 2-2. Schematic diagrams of (a) mold for splitting tensile strength test and (b) mortar sample under splitting test.

2.3 Results and Discussion

2.3.1 Resistivity Response over Time

The average resistivity along the sample depth of the three curing methods is shown in Figure 2-3. Every curing method shows growth in resistivity over time and the resistivity curve of different curing methods presents a similar shape. The similar shape of resistivity growth is likely caused by hydration reactions and consumption of water over time. This will be discussed more in the document over these mechanisms. As the hydration reaction proceeds, free water is consumed to form hydration products as the mixture changes from a slurry to a solid. As a result, the average resistivity of the mortar specimen increases with hydration. The air curing shows the highest resistivity followed by the sealed sample, and then the wet cured sample has the lowest resistivity. The difference in resistivity could depend on several factors including the amount of moisture in the pores, ion concentration in the pores, and the tortuosity of the pore network. In this work, the moisture amount and the porosity of the samples are examined. This will be discussed further in the paper.

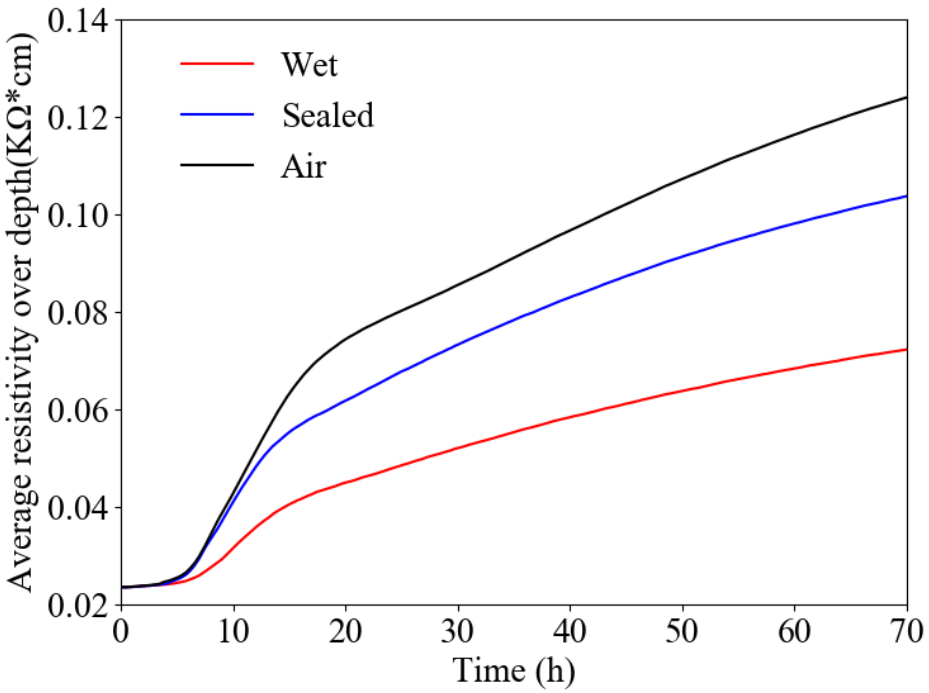

Figure 2-3. Average resistivity curve over the depth of different curing methods.

Figure 2-4 shows the percentage of moisture change for the three curing methods. It shows that the wet curing sample has absorbed moisture within the first 20 h and the air curing sample has the most mass loss in the first 20 h. A slight moisture loss happens to the sealed sample during the first 8 h and then the mass is constant. In all samples, the mass change stopped after roughly 20 h. This is likely caused by the hydration process reducing the porosity and pore connectivity in the mortar. As stated above, the difference in resistivity between curing methods is at least partially caused by moisture differences between the samples. The moisture change curve supports this statement by showing that the air curing sample has the most moisture loss over time and the wet curing sample has moisture absorption over time.

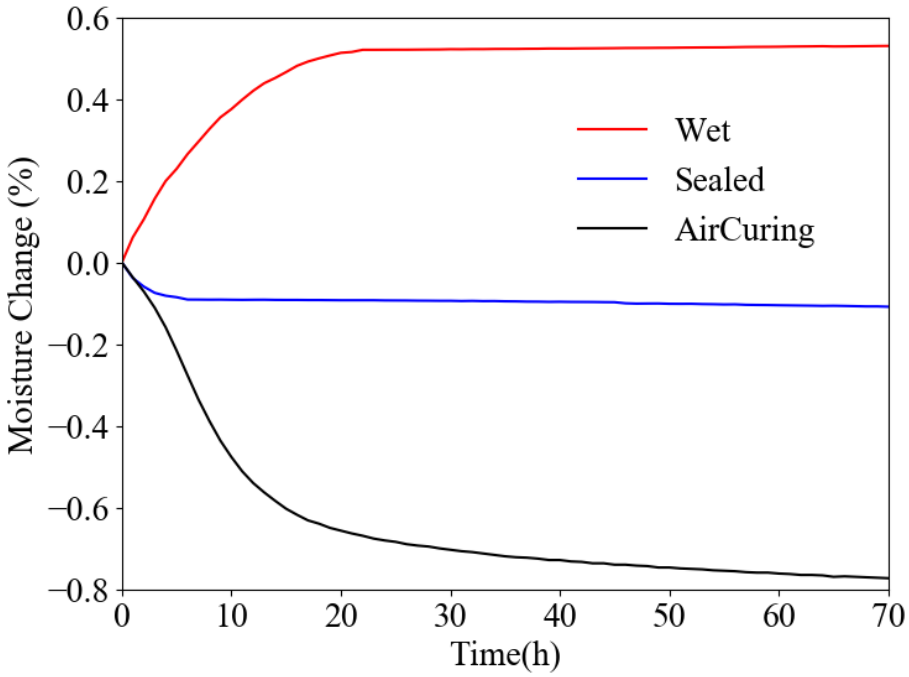

Figure 2-4. Percent moisture change over time.

Figure 2-5 shows the resistivity profile over the sample depth at different times. The wet curing sample had uniform resistivity over the depth. There is a resistivity gradient observed for the air cured and sealed cured samples. This gradient is first observed at about 8 h in the sealed and air cured sample and it continues to magnify over time. These same samples showed measurable moisture loss at 8h in the drying experiments from Figure 2-4. This loss of water likely contributes to the observed changes in resistivity. The higher resistivity at 12.7 mm compared to 76.2 mm is expected if there is more moisture loss at the surface of the sample.

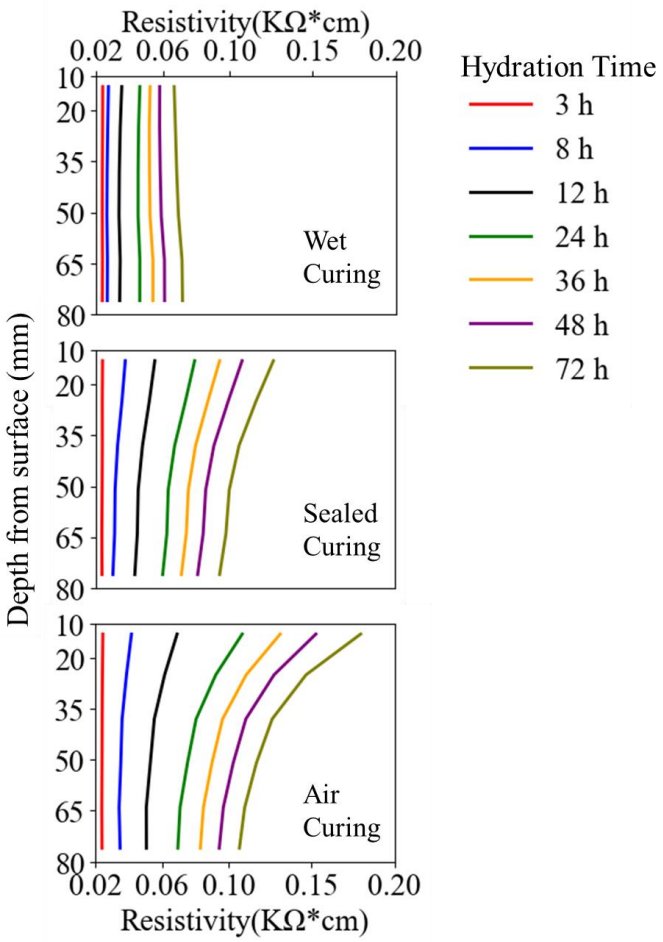

Figure 2-5. Resistivity gradation profile at different time points of wet curing, sealed curing, and air curing.

2.3.2 Porosity and DOS Change

The DOS of the wet curing specimen is expected to be higher than the other curing methods because of the extra moisture provided over time. Also, this extra moisture promotes the hydration reaction and this will reduce the porosity of the wet curing samples compared to the other methods. For the sealed sample, the moisture is consumed during the hydration and there is some evaporation over the first several hours of hydration. In the air curing sample, water is consumed during hydration and also lost to evaporation. Because of the loss of water, the air curing sample is expected to have the highest porosity and lowest DOS.

Figure 2-6 shows how the porosity and DOS change over time. Each line on the figure represents a different curing method. At 12h, the three curing methods have almost the same porosity over the depth, which indicates that the degree of hydration of the three curing methods is similar despite the difference in moisture content. It should be noted that after hydrating for 24h, there is a porosity gradient in every sample with the furthest depth having the lowest porosity and the surface having the highest porosity. This higher porosity at the surface may be caused by differences in bleeding. When comparing the results at each depth, the air cured sample has the highest porosity followed by the sealed cured sample and the wet cured sample has the lowest porosity. This difference in porosity between the curing types is caused by the differences in the amount of moisture available for hydration. It should be noted that the air cured sample stopped showing a porosity change at 19 mm from the surface after 48 h. This is shown by the green line. This might be caused by the humidity not being high enough within the sample to sustain hydration. More insights into this can be found from the DOS measurements.

The right column of Figure 2-6 shows the DOS or the moisture content within the samples. There is a minimal DOS gradient in the wet cured and sealed cured samples. The sealed cured sample has a lower DOS than the wet cured samples. This difference is caused by the continuous amount of moisture provided on the surface of the wet cured sample. It should be noted that the DOS of the wet curing sample is increasing from 12h to 48h. This is likely caused by the water absorbed into the sample during wet curing. This matches the mass increase observed during wet curing shown in Figure 2-4.

The air cured samples in Figure 2-6 show a lower DOS at all depths compared to the wet and sealed cured samples; however, at 19 mm from the surface, the air cured sample shows a much lower DOS than the wet and sealed cured samples. This lower DOS in the air cured samples is caused by the loss of water from the surface. A direct comparison of the moisture change is shown in Figure 2-4. It should be noted that the DOS for the sample at 19 mm depth is below

60% DOS after 48 h for the air cured sample. Based on the previous literature this suggests that hydration should stop when the relative humidity is below 80% [33].

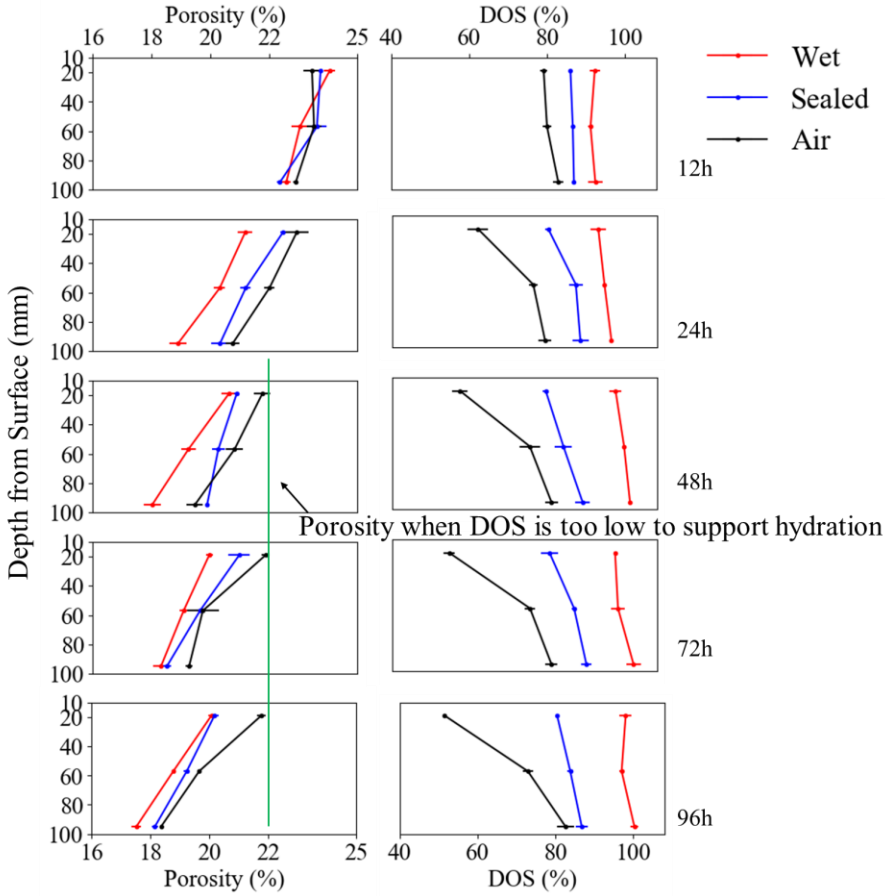

Figure 2-6. Porosity and DOS gradation profile over the sample depth at 12, 24, 48, 72, 96 h of wet, sealed, and air curing.

Figure 2-7 shows the resistivity and DOS at 12, 24, 48, and 72 h of hydration over the sample depth for the three curing methods. The graph shows that the DOS and resistivity curves are correlated. For example, as the DOS begins to decrease, the resistivity increases. This means the resistivity value gives important insights into the moisture content inside the concrete. This also means that a resistivity value taken near the surface and one taken in the depths of the sample could be used as an indicator of the DOS and hence the moisture in the concrete. This could be used as a useful tool to measure the quality of the curing applied to the concrete.

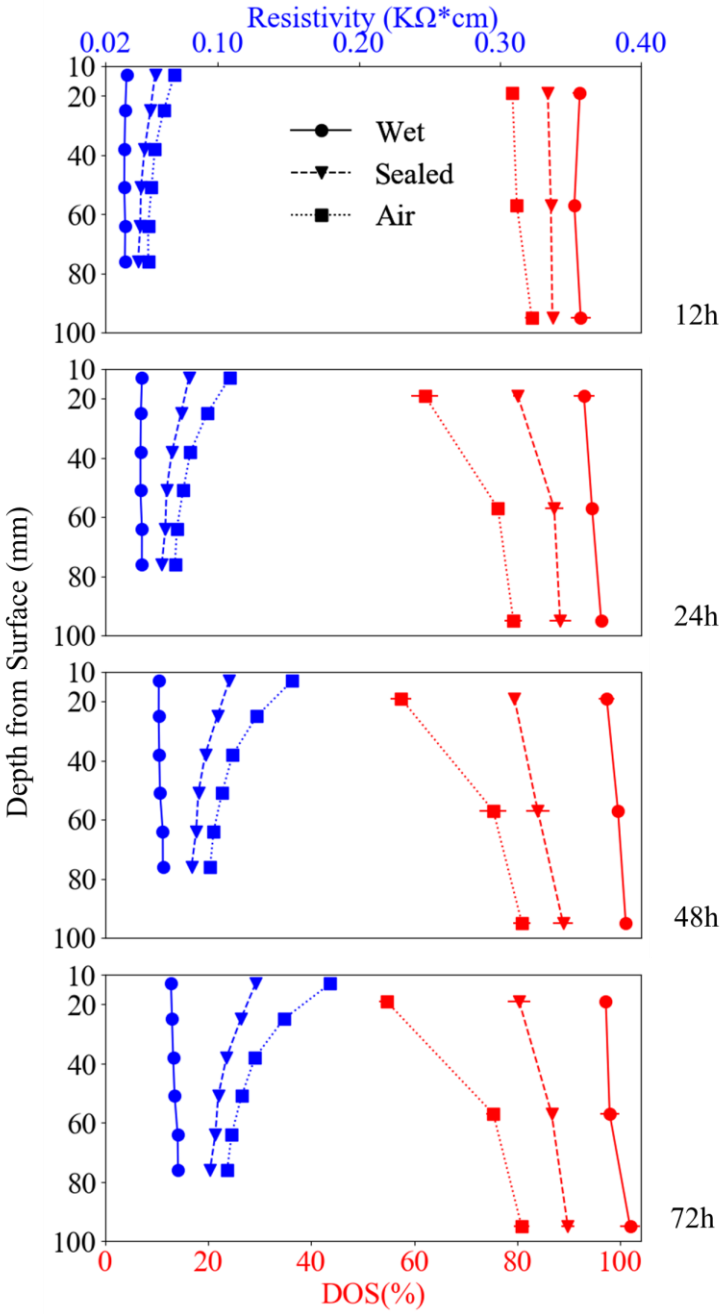

Figure 2-7. Resistivity and DOS at 12, 24, 48, 72 h of hydration of wet curing, sealed curing, and air curing.

Figure 2-8 shows that the resistivity and DOS can be assumed to be linearly related between 12h and 72 h of hydration. The fitted curve between resistivity and DOS through linear regression at

different times is shown in Figure 2-8. The resistivity at each point was determined by linear interpolation of the two adjacent points that vary by +/- 5 mm.

Figure 2-8 shows that the resistivity and DOS are linearly related between 12 h and 72 h of hydration. The fitted curve between resistivity and DOS through linear regression at different times is shown in Figure 2-8 and this linear regression function can be used to predict the DOS value with resistivity measurements. The parameters of each fitted line are shown in Table A. 1 in Appendix C. The R square value is close to 1 for 24h, 48h, and 72h, which illustrates the high accuracy of the linear relationship. These fitted curves can then be used to predict the DOS at any depth within the sample at a given time.

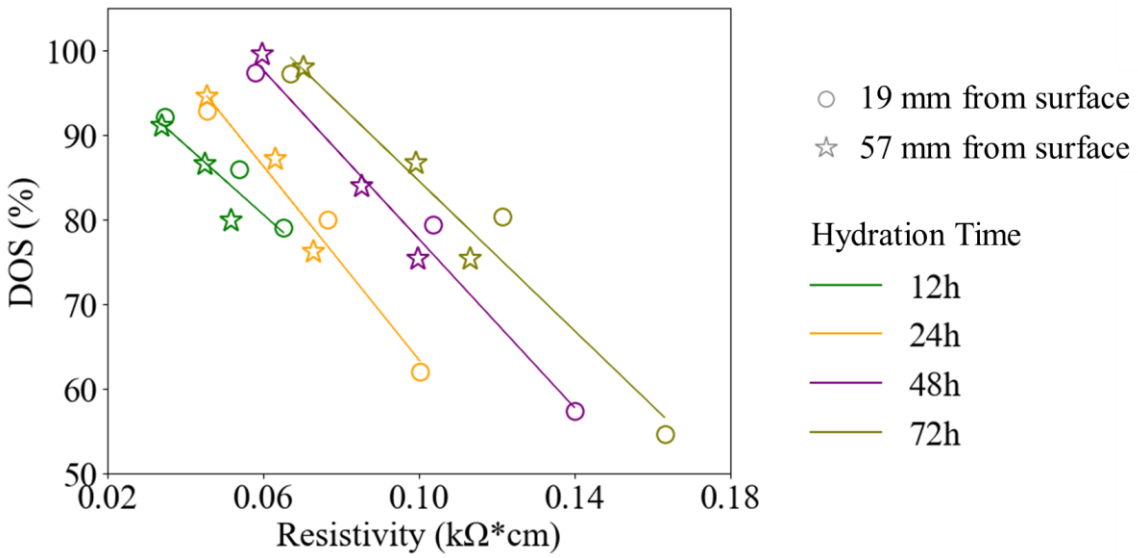

Figure 2-8. DOS is shown as a function of resistivity at 19 mm and 57 mm from the surface after hydrating for 12, 24, 48, and 72h respectively.

Figure 2-9 shows the predicted DOS based on the resistivity measurements. The predicted DOS shows good agreement with the measured DOS value. This means using resistivity measurement can quantitatively compare the DOS created by different curing methods for a given set of

materials. This can be used as a new tool to measure how water loss from hydration or drying correlates to the DOS or water content within a concrete sample. Since this moisture content during hydration is so important to the properties of the concrete, these resistivity measurements can provide important insights into the material properties of the concrete.

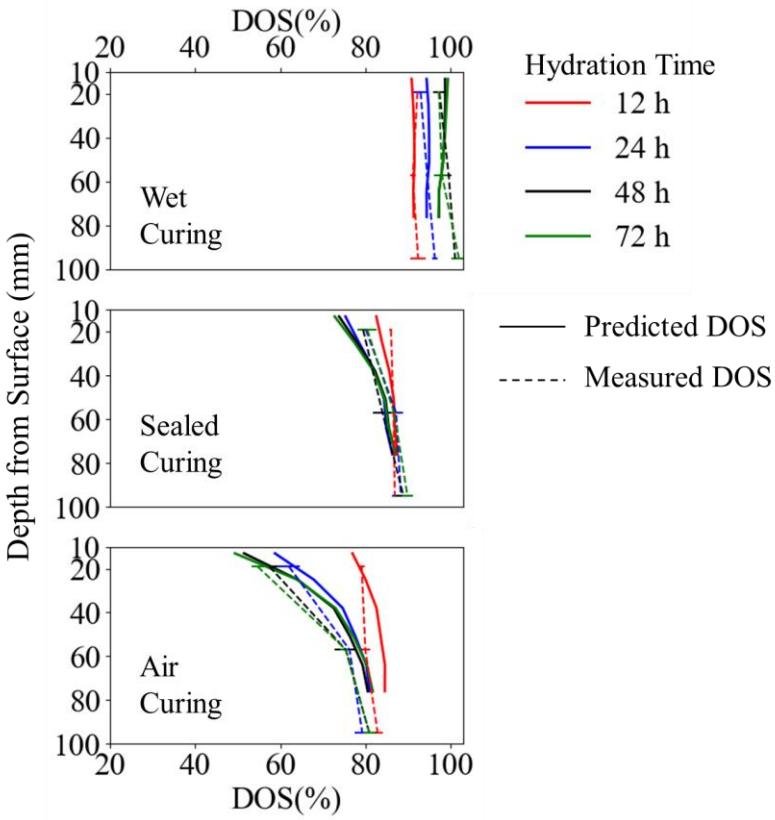

Figure 2-9. Predicted DOS from resistivity at 12, 24, 48, 72 h of hydration compared with the measured DOS.

It can be noted in Figure 2-8 that as the hydration proceeds, the DOS versus the resistivity curve shifts to the right, the slope of the curve decreases, which indicates that resistivity becomes more and more sensitive to DOS change as hydration proceeds. This is likely because the formation of hydration products decreases the porosity and increases the resistance of electron mobility. Figure 2-10 shows the measured porosity versus the resistivity at 86% DOS at different hydration times. This porosity and resistivity were chosen from the sealed curing specimen and a DOS of 86% was

chosen because it would ensure hydration is continuing. Because a constant DOS is used, the plot shows how the porosity would change with resistivity at a fixed DOS. This means that as the hydration reaction proceeds, the porosity decreases, and the resistivity increases. The relationship seems to be bilinear between 12 h and 72 h. This change in the shape of the curve could be caused by differences in pore solution chemistry or the connectivity of the pore structure at different times. These are areas of future research. This is an important finding because it shows the ability of resistivity to give insights into the pore structure properties of mortar as it hydrates.

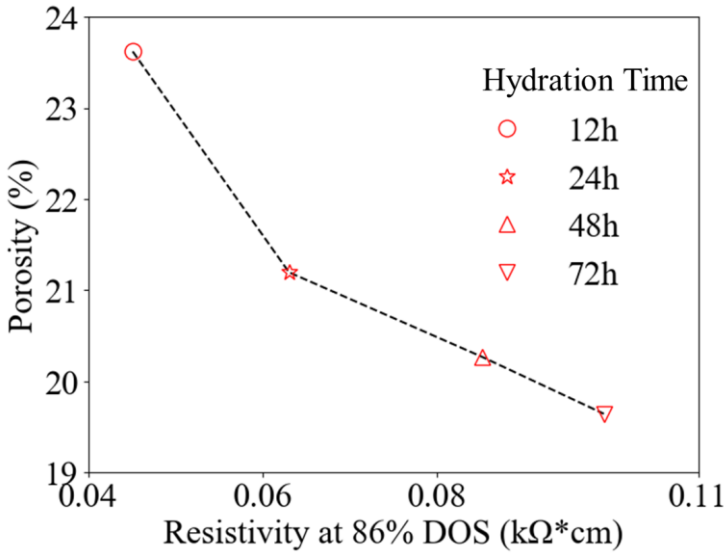

Figure 2-10. The relationship between porosity and resistivity at 86% DOS.

2.3.3 Splitting Tensile Strength

Figure 2-11 shows the splitting tensile strength at 72 h for the three different curing methods in comparison to the average resistivity at the same time and the same depth. The results show that the resistivity is inversely proportional to the splitting tensile strength of the concrete. For example, the wet curing sample exhibited the highest splitting tensile strength and the lowest resistivity and the air cured sample showed the lowest splitting tensile strength and the highest resistivity. These differences in strength and resistivity are likely caused by differences in the DOS during hydration. This means that under certain conditions the resistivity can give insights

into the tensile strength of the concrete. This is not surprising as Figure 2-8 and Figure 2-10 show that the resistivity can be related to both the porosity and DOS during the first 72 h of hydration.

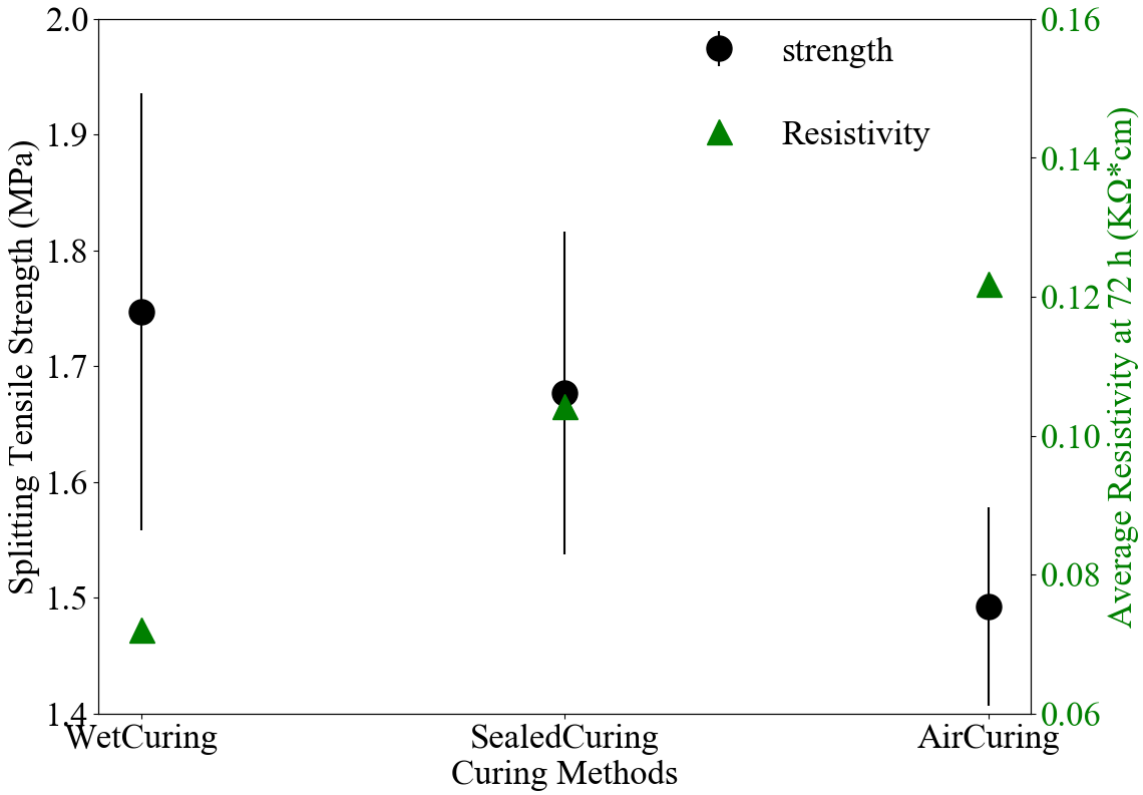

Figure 2-11. Splitting tensile strength at 72 h and average resistivity along depth at 72 h of the three curing methods

2.4 Practical Significance

This work compares the resistivity of air, sealed, and wet curing at different depths in a sample. The results suggest that the resistivity can be correlated to the DOS, porosity, and tensile strength of the sample between 12h and 72h. This means that resistivity measurements during this period could be used to determine the uniformity and effectiveness of different curing methods and provide insights into the uniformity of the hydration over the depth of the sample. This information can provide insights into the porosity and ultimately the strength of the samples at

different depths by making real-time measurements that are minimally intrusive. These measurements could be used in either the field or the lab to inexpensively evaluate concrete quality in almost real-time. For example, this technique could be used to determine how sensitive a concrete mixture is to different curing practices. This technique could also be used in the field to use the resistivity gradient in the concrete to give insights into the quality of the real-time curing and hydration of the concrete. Since the resistivity measurements can be made easily and economically then this makes the measurements very useful.

2.5 Conclusions

A new technique of comparing curing effects using electrical resistivity at different depths was investigated in this study. The electrical resistivity was compared between wet curing, sealed curing, and air curing methods, at different depths within the sample and at different hydration times. These measurements are compared to the porosity, DOS, and tensile strength of the sample, and a linear relationship between resistivity and DOS is created for these materials. The following conclusions can be drawn for mortar between 12h and 72h:

- Resistivity corresponds to the degree of saturation, porosity, and tensile strength of a mortar mixture.
- A linear relationship is developed between resistivity and degree of saturation and this relationship changes as hydration proceeds.
- A bi-linear relationship exists between resistivity and porosity at a fixed DOS that is high enough to promote hydration.
- Wet curing samples showed uniform moisture gradients and had the highest degree of saturation and tensile strength of the samples measured. These samples also showed a 0.5% increase in the mass over the first 20 h of hydration.
- The air cured sample at 23°C and 50% relative humidity environment showed a significant drying gradient over the top 85 mm and the refinement of the pore structure

stopped after 48 h. This sample also showed a 0.78% decrease in the mass over the first 70 h of hydration.

- The sealed sample showed a uniform moisture gradient and had a degree of saturation, porosity, and tensile strength that is between the wet cured and air cured samples. This sample showed only a slight change in mass during hydration which is likely from an imperfect seal.
- A porosity gradient was observed in all the mixtures regardless of the curing method used. This gradient is likely caused by differences in curing and also bleeding.

This work establishes a systematic method to use resistivity to rapidly and economically measure the in situ degree of saturation, porosity, and provide insights into the tensile strength of the concrete. This could provide a useful scientific and practical measurement technique for future work.

CHAPTER III

EARLY AGE HYDRATION INVESTIGATION ON CONCRETE WITH WET CURING APPLIED AT DIFFERENT TIMES

3.1 Introduction

Curing is an important process in producing durable concrete. Wet curing is often used when concrete needs to be the most resistant to deterioration. The purpose of wet curing is to provide continuous moisture to the fresh cement-based system to promote hydration [1, 2]. As a result, wet curing can improve the porosity, permeability, strength, shrinkage, and creep of the resulting concrete [3–10]. While there are many benefits to applying wet curing to concrete, there are also challenges because it is labor-intensive and can therefore it can be challenging to apply the wet curing in a timely manner.

The goal of this work is to investigate the influence of wet curing applied at different times in different evaporative environments to determine the allowable delay in applying the wet curing on the surface before the properties of the concrete are compromised. This work examines the performance in evaporation rates between 0.15 kg/m^2/h and 0.85 kg/m^2/h. These evaporation rates are commonly observed in practice but are not the highest evaporation rates that can be measured. This research purposely focused on lower evaporation rates as they would show the most potential to delay the application of wet curing. A nomograph predicting the evaporation rates

based on different weather conditions is shown in Figure 3-1. The evaporation rates investigated are shown.

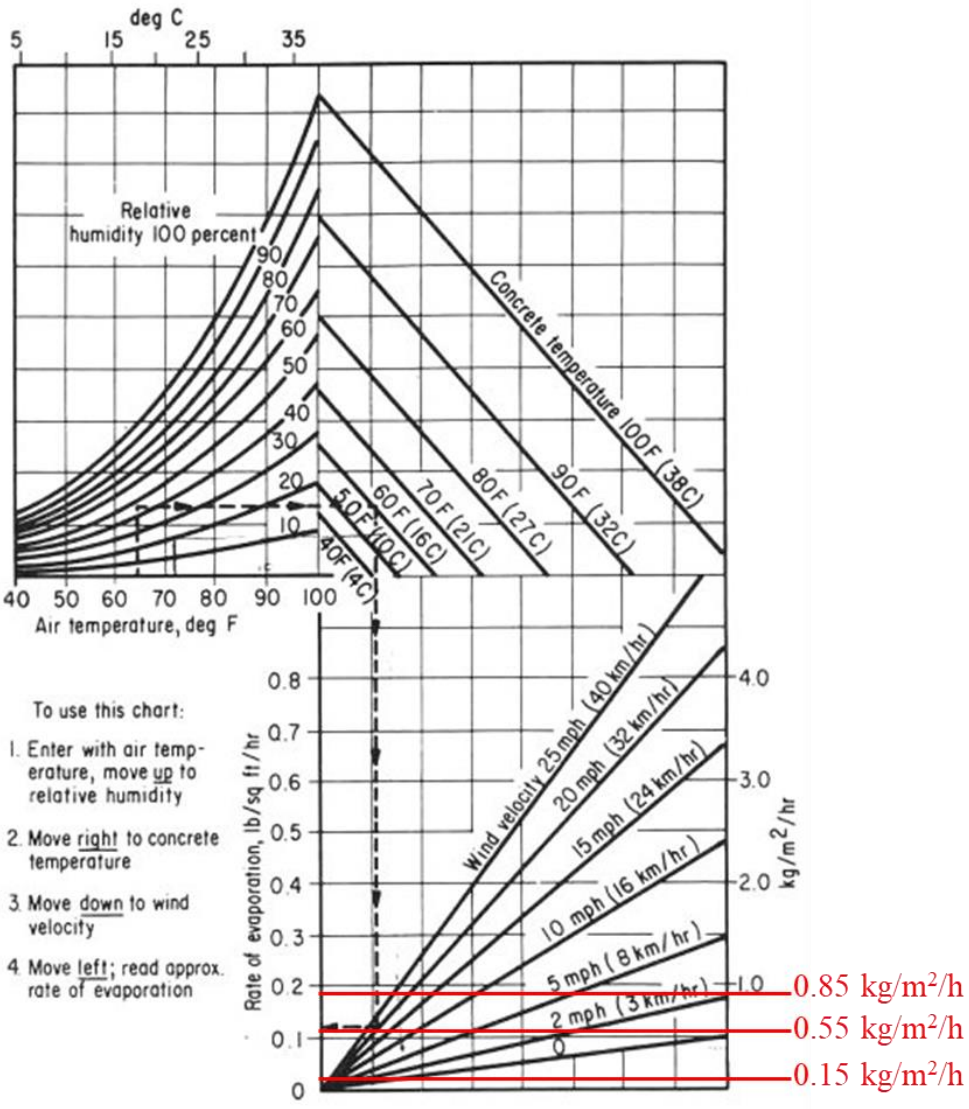

Figure 3-1. ACI nomograph for estimating surface water evaporation rate of concrete: the "ACI Hot Weather Concreting Evaporation Nomograph" [36].

The curing methods evaluated include wet curing applied to the surface with no delay or continuous wet curing, wet curing applied with a delay between 2h and 10h, and samples with no curing applied to the surface or air curing. When wet curing is applied to the surface with no

delay it will be called “continuous wet curing”. The samples that were not cured will be called “air curing”.

The impact of these different curing methods is measured by the diffusion coefficient, porosity, and degree of saturation (DOS) [27] after 72h of hydration. The resistivity along the sample depth was also used to monitor the hydration for the first 72h, as resistivity measurement is sensitive, effective, nondestructive, and it can perform rapid and continuous measurement with low cost [16–21]. In addition, the temperature gradient of the samples with the highest evaporation rate (0.85 $kg/m^2/h$) is also measured.

3.2 Experimental Methods

3.2.1 Materials and Mixtures

The concrete mixture in this study was prepared according to ASTM C305 [25] with a w/cm ratio of 0.45. The mixture proportion by volume is shown in Table 3-1. The cement used in this study met the requirements of an ASTM C150 Type I Portland cement. The fine and coarse aggregates used for the mixture are local aggregates that meet the requirements of ASTM C33. The Blaine of the cement is 3560 cm^2/g and the free lime content is 1.4%. The chemical compositions of the cement are shown in Table 3-2. This mortar mixture is designed to be the mortar portion of the concrete mixture used in the other tests in the paper (See Table 3-3).

Table 3-1. Mixture proportion of concrete.

w/cm	Cement (kg/m^3)	Coarse Aggregate (kg/m^3)	Fine Aggregate (kg/m^3)	Water (kg/m^3)
0.45	366.7	1078.6	747.6	142.6

Table 3-2. Chemical composition of cement.

	SiO_2	Al_2O_3	Fe_2O_3	CaO	MgO	SO_3	Na_2O	K_2O	C_3S	C_2S	C_3A	C_4AF	LOI
Cement (%)	21.1	4.8	3.1	64.5	2.33	3.2	0.17	0.58	50	23	7	9	2.6

Table 3-3. Mixture proportion of mortar.

w/cm	Cement (kg/m^3)	Fine Aggregate (kg/m^3)	Water (kg/m^3)
0.45	598.0	1495.0	266.9

s

3.2.2 Testing Environments

The concrete samples were tested under three different environments as summarized in Table 3-4. The 0.15 and 0.55 $kg/m^2/h$ evaporation rates were obtained by storing the samples at 50% RH and 23°C and 38°C respectively. The highest evaporation rate was obtained by storing the concrete 30.5 cm away from a 250 Watt heating lamp. A hygrochron sensor showed that the air temperature was 43°C with a 12% RH. When wet curing was applied, three layers of water-soaked burlap were placed on the surface and then this was sealed with aluminum tape to prevent evaporation. Every day the burlap was removed and soaked with water and placed on top of the sample. The air curing sample was open to the environment.

Table 3-4. Curing methods applied to the concrete samples in different environments.

Environments	Maximum Evaporation Rate	Temperature & Humidity	Curing methods applied to concrete samples
Low Evaporation	0.15 $kg/m^2/h$	23°C+50% RH	Air curing; Continuous wet curing; Wet curing after being exposed to the environment for 3h, 6h, 9h respectively
Middle Evaporation	0.55 $kg/m^2/h$	38°C+50% RH	Air curing; Continuous wet curing; Wet curing after being exposed to the environment for 3h, 6h, 9h respectively
High Evaporation	0.85 $kg/m^2/h$	43°C+12% RH	Air curing; Continuous wet curing; Wet curing after being exposed to the environment for 2h, 4h, 6h, 8h, 10h respectively

3.2.3 Evaporation Rate

The evaporation rate of the three curing environments was determined by measuring the mass change of the concrete sample over time. The evaporation rate was determined according to Equation 3-1, where r is the evaporation rate, Mi is the initial mass of the sample, Mn is the mass after evaporation, and A is the surface area of the sample, t is the elapsed time. The evaporation was determined by the integration of the evaporation rate over time shown in Equation 3-2.

$$Evaporation\ rate: r = \frac{M_i - M_n}{A * t} \quad \text{Equation 3-1}$$

$$Evaporation = \int r\ dt \quad \text{Equation 3-2}$$

3.2.4 Electrical Resistivity

The molds were 152.4mm in diameter by 228.6mm tall plastic cylinders. The cylinders used seven layers of 4-40 threaded stainless steel rods with a 4.57mm diameter. Each layer used two rods with a horizontal spacing of 92.7mm and a vertical spacing of 12.7mm. The steel rods were installed through the molds and were stabilized and sealed with glue before the concrete was placed. The configuration of the specimen is shown in Figure 3-2. Concrete was used to fill the mold to 203.2mm in height. The top 25.4mm was not filled to allow curing methods to be applied. The concrete was placed in three layers. For each layer, the sample was consolidated for 10 s with a vibrating table at a frequency of 60 Hz to remove entrapped air and to promote a good bond with the threaded rod.

During hydration, water is consumed and the sample shrinks [26]. This change in volume may form a gap between the mold and the edge of the sample. To ensure that the drying is only from the top of the sample and not from the edges, the edge of the fresh mortar was sealed and covered by mortar. More details can be found in Appendix A.

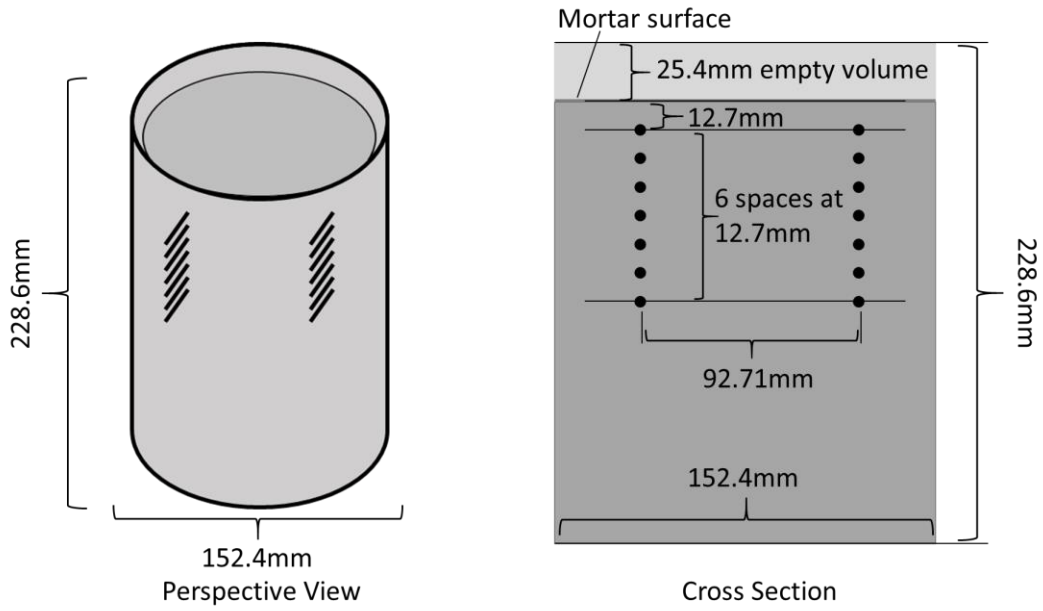

Figure 3-2. Configuration of the mortar sample for resistivity measurement.

After the samples were cast into molds, the resistivity was measured between the rods every 10 minutes through the hydration process. The circuit for the resistivity measurement was programmed with the Arduino platform. An Arduino Mega 2560 was used as the central processor with a 12-Bit impedance converter AD5933. In this research, a frequency of 30 kHz was used. The system was calibrated with a 100-ohm resistor. The calibration process was to calculate the Gain Factor of the system based on a known resistor. The Gain Factor can then be used to calculate the resistivity of future measurements. The detailed calculations are in Appendix B.2. Five multiplexers are used to measure 80 channels simultaneously. The results are recorded on an SD card and retrieved for analysis. More details about the additional hardware and the raw data process of resistivity can be found in Appendix B.1.

3.2.4.1 Resistivity gradient

The resistivity gradient is calculated along with the sample depth from 13 mm to 89 mm from the sample surface. Equation 3-3 was used to calculate the resistivity gradient, where R13mm and R89mm are the resistivities at the depth of 13 mm and 89 mm from the surface measured at the

same time of hydration. The gradient is a helpful measurement to compare the resistivity between curing methods because before the application of wet curing, the bottom of the sample at 89 mm is moist and the sample at the surface could be different. Using the resistivity at 89 mm this normalizes the measurement between mixtures.

$$Resistivity\ gradient\ (K\Omega * cm\ /\ mm) = (R_{13mm} - R_{89mm})\ /\ (89 - 13) \qquad \text{Equation 3-3}$$

3.2.5 Temperature

The temperature at different depths was measured on concrete samples in the highest evaporation environment during air curing, continuous wet curing, and wet curing after drying for 6h. The concrete samples for temperature measurement were cast into the same molds as those for the resistivity test. Four type T thermocouples were used along with the depth as shown in Figure 3-3 before the concrete was filled. The thermocouples were stabilized and sealed by glue. The molds were filled in the same way as that of the resistivity test. The temperature was measured with a time interval of 10 minutes.

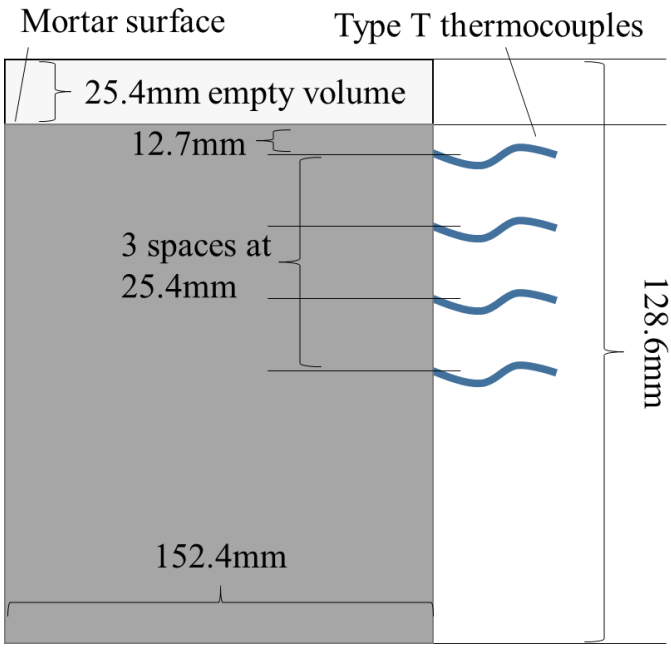

Figure 3-3. Configuration of the thermocouples of the mortar sample.

3.2.6 Porosity and Degree of Saturation (DOS)

The porosity and degree of saturation (DOS) [36] are investigated to examine the curing influence in the three environments by using mortar samples. Mortar samples are used because coarse aggregates can significantly impact the measurements of these tests. The mixture design of mortar samples is shown in Table 3-3. The mortar samples were cast into tubes of 25.4 mm in diameter by 114.3 mm tall. Each tube was filled with three layers of mortar.

The porosity measurement allows the total pores to be compared between mixtures. As the hydration continues then it is expected that the porosity would decrease. This means that a sample with a higher porosity will have a lower amount of hydration and lower strength and possibly higher diffusion coefficient.

The DOS shows the amount of moisture within the sample. This allows the relative moisture content of the different samples to be compared when the samples are 72h old. This is useful because the moisture content of the sample is important to understand the diffusion results. Also, the air-dried samples provide insight into the amount of drying in the sample and how that impacts hydration. Other research shows that hydration ceases at a relative humidity of about 80% due to negative capillary pressure that opposes the reaction [33], and this is close to a DOS of 65% [37].

The porosity and DOS were measured when the samples were 72h old. For each curing method, three samples were measured. At 72h the sample was demolded and cut into 3 segments that are each 38.1 mm tall. This means that the distance to the midpoint of each segment is 19.1 mm, 57.2 mm, and 95.3 mm from the sample surface. This is helpful to determine the porosity and DOS at different depths.

The porosity and DOS were determined by ASTM C642 with some minor changes where the samples were saturated within a vacuum chamber instead of boiling in water. Equation 3-4 and

Equation 3-5 were used to calculate the porosity and DOS, where W_i is the initial weight of the sample, W_d is the oven-dried weight at 110 ºC, W_{sa} is the saturated surface dried (SSD) weight, W_{su} is the suspended apparent mass of the saturated samples.

$$Porosity = \frac{W_{sa} - W_d}{W_{sa} - W_{su}} \times 100 \quad \text{Equation 3-4}$$

$$DOS = \frac{W_i - W_d}{W_{sa} - W_d} \times 100 \quad \text{Equation 3-5}$$

3.2.7 Diffusion Coefficient

The mortar mixture used for diffusion testing is the same as the porosity and DOS and is shown in

Table 3-3. The containers for the mortar sample were 15.44 mm in diameter by 113.54mm long cylinders. The mortar samples were cured in the same way as the concrete samples. When it was time to wet cure the samples, water was placed on the top. The air cured sample never received water. For each curing method, four samples were measured.

The configuration of the diffusion test is shown in Figure 3-4. In this test, the diffusion coefficient of the mortar was obtained by placing KI solution on the sample and monitoring the ion penetration depth over time. This method has been described in previous publications [38–41]. The higher the diffusion coefficient, the easier for the sample to be penetrated by outside chemicals, this makes the concrete more susceptible to damage caused by chlorides or other chemicals.

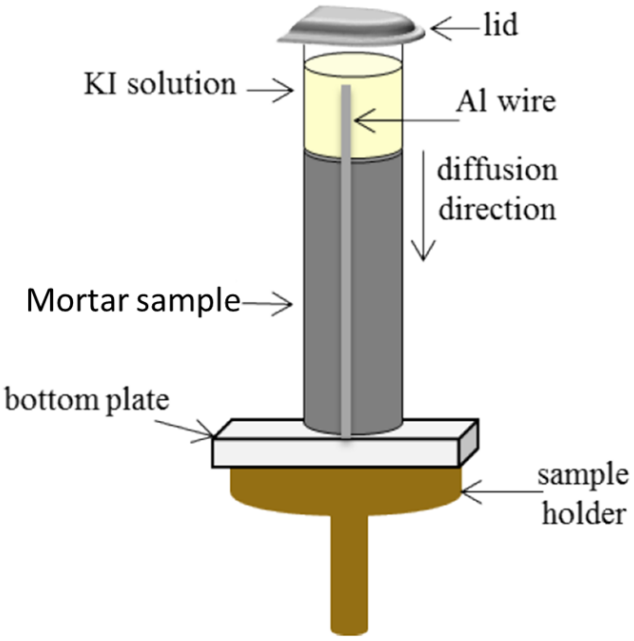

Figure 3-4. Configuration of Diffusion Testing.

3.3 Results and Discussion

3.3.1 Evaporation

The total amount of evaporation and the rate of evaporation is shown in Figure 3-5. The maximum evaporation rate will be used for discussion in this paper because a widely available tool exists in Figure 3-1 to calculate this value. Within the first hour of measurement, the maximum evaporation rate was measured for each sample. The lowest evaporation rate of 0.15 kg/m^2/h is for a sample that was stored at 23°C and 50%RH. This sample had an almost constant evaporation rate. The sample stored at 38°C and 50%RH had the next highest evaporation rate at 0.55 kg/m^2/h. The evaporation rate was constant from the first measurement until 4h later. The highest evaporation rate is 0.85 kg/m^2/h. This sample was stored 304.8 mm away from a 250 Watt heating lamp. This maximum evaporation rate was only held for about 2h and then decreased. Interestingly, the evaporation rate for the 0.55 and 0.85 kg/m^2/h samples followed a very similar trend between 5h and 12h. This could be because both surfaces are predominately

solid and so they have similar resistance to evaporation. More work is needed to better understand this.

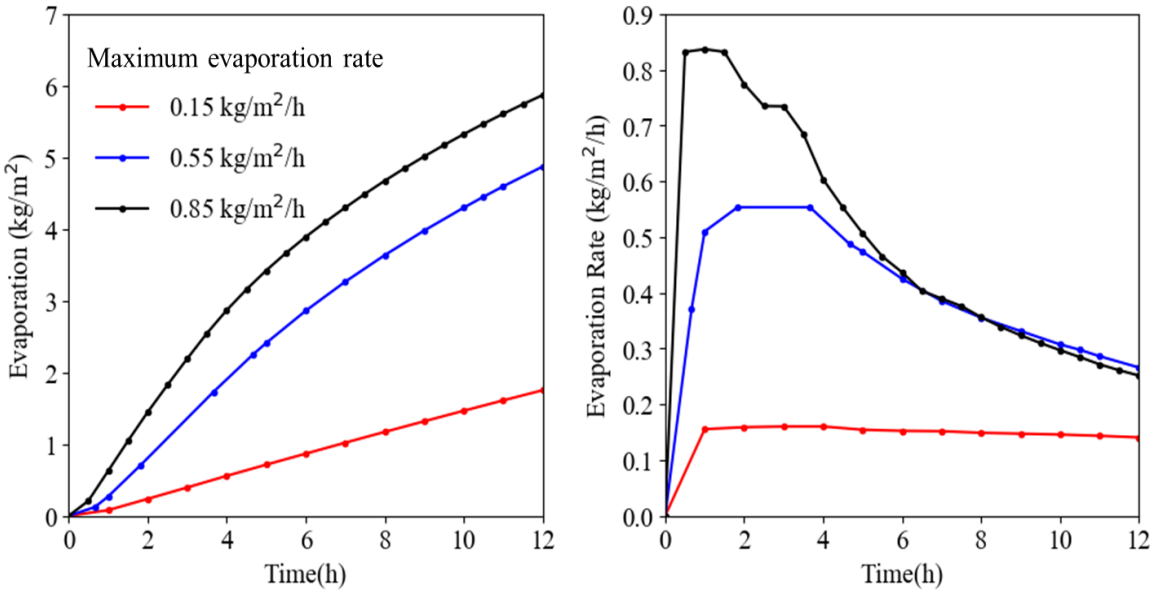

(a) (b)

Figure 3-5. (a) Evaporation over time of the three curing environments, (b) Evaporation rate over time of the three curing environments.

3.3.2 Temperature

The temperature at different depths within the concrete in the highest drying environment is shown in Figure 3-6. The results are shown for air curing, continuous wet curing, and wet curing after drying for 6h. Each curve shows the heat from the exothermic reaction of hydration that occurs at roughly 9h. The results show that the temperatures within the concrete are greatly impacted by how the samples are cured. The air curing sample had the highest temperature at 13mm from the surface of about 43°C and the other depths were about 40°C after 10h of hydration. The continuous wet curing had a uniform temperature that was about 15°C less than the air curing sample. The sample initially open to the environment for the first 6h had a similar temperate as the air curing sample over the first 6h; however, after the wet burlap was placed on

the concrete the temperature dropped to be similar to the sample with continuous wet curing. This shows that even after 6h of drying, the wet curing can reduce the internal temperature of the concrete to levels that are similar if it was continually wet cured even in hot and dry environments. This is useful to understand the internal temperature gradient within the concrete.

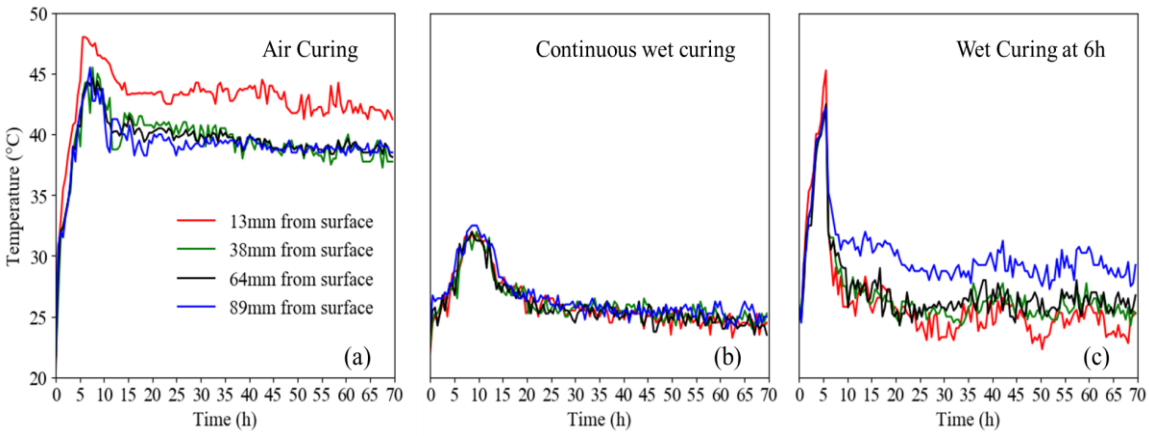

Figure 3-6. Temperature over time inside the concrete samples under the heat lamp of (a) air curing, (b) continuous wet curing, (c) wet curing after drying for 6h.

3.3.3 Electrical Resistivity

The average electrical resistivity over the depth of the concrete samples for the three different drying environments is shown in Figure 3-7. An overview graph is shown as well as a zoomed graph that provides more details. Note that the reduction in resistivity corresponds with the time when the wet curing was placed on the sample. There is no correction for differences in temperature in this data as the impact of temperature is shown to be insignificant because the resistivity is controlled by the DOS of the sample during this period [37].

In each environment, before the wet curing is applied, the resistivity curve follows the air curing sample. One important observation is that once the wet curing is placed on the samples with the 0.15 and 0.55 kg/m^2/h evaporation rates, the resistivity matches the concrete that received continuous wet curing. This seems to suggest that even though the samples have been drying in

these environments, once the water is placed on the surface the electrical resistivity returns to the same values as if it was continuously wet cured. This seems to indicate that a drying period of 9h in 0.15 and 0.55 kg/m^2/h evaporation rate did not keep water from penetrating the concrete; however, this is not the case in the 0.85 kg/m^2/h evaporation rate environment. In this environment, the sample that was drying for 2h returned to the same electrical resistivity level as the sample that had been under continuous wet curing but the sample that was cured for 4h did not. This higher resistivity level after placing the wet curing suggests that the material has been altered by the drying. This suggests that the material has been microcracked or the structure has been altered in a way that the drying has created a permanent change in the material.

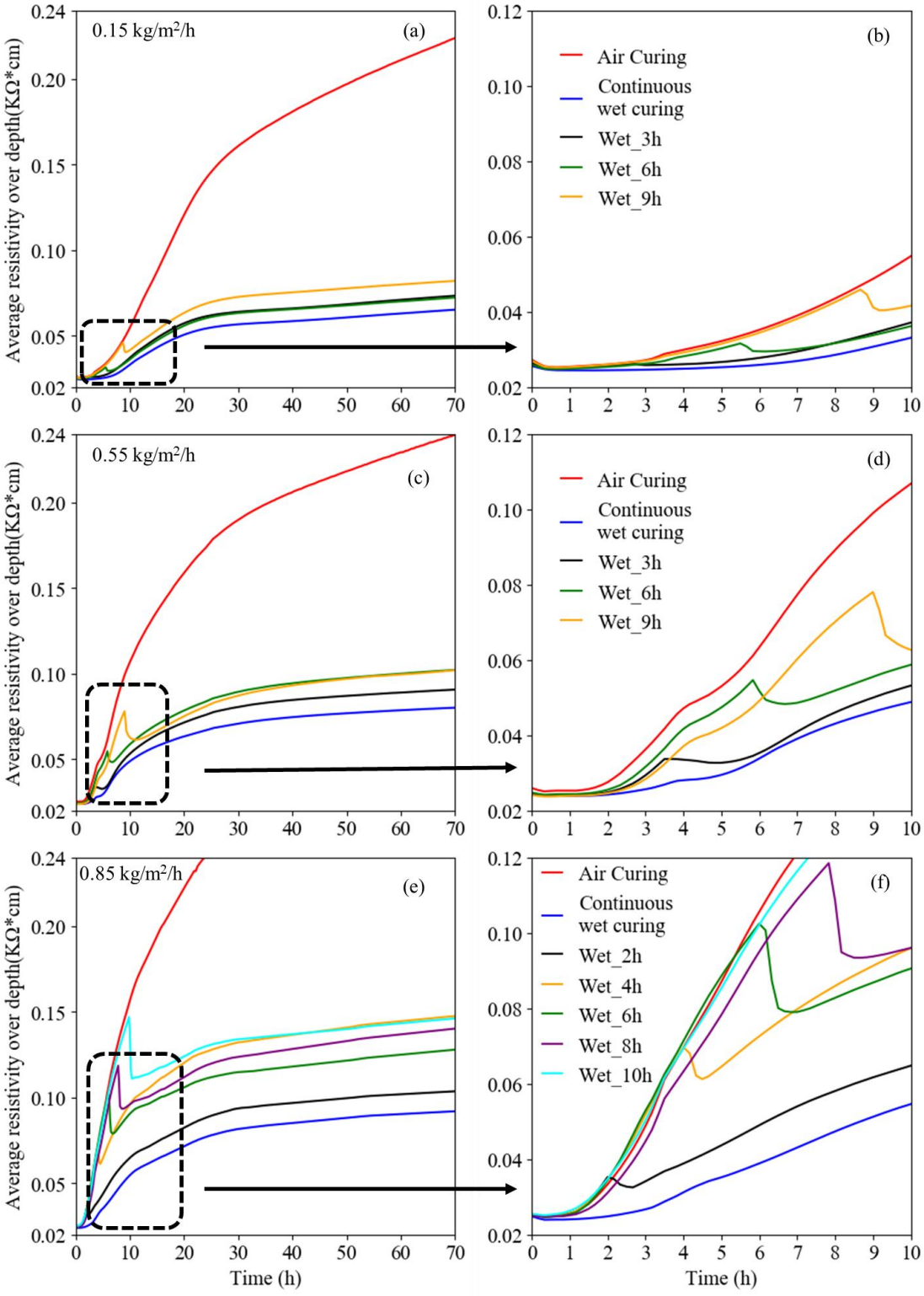

Figure 3-7. Electrical resistivity of the concrete in different drying environments for wet curing placed at different times on the surface.

3.3.4 Porosity and DOS Test

The porosity and DOS change for samples with different periods of wet curing are shown in Figure 3-8. For the air curing sample, water is consumed during hydration and is also lost to evaporation. Because of the loss of water, the air curing sample is expected to have the highest porosity and lowest DOS compared to the other samples with wet curing. The DOS of the specimen with wet curing applied is expected to be higher than the air curing sample because of the extra moisture provided over time.

The DOS of the air cured samples is helpful to understand the severity of the drying that occurs at different depths of the sample. As expected, the relative ranking of the DOS at the surface matches the relative ranking of the maximum evaporation rate. It is interesting to note that all three drying environments showed very similar DOS at 60 mm and 100 mm from the surface. This shows that differences in surface drying primarily impact the top 100 mm of the sample. For all of the evaporation rates, the DOS of the wet cured samples at any time period are very similar. Since the DOS measures the amount of water in the pores, this shows that the wet curing filled the available pores.

The porosity measures the total volume of pores in the sample. A student t-test between continuous wet curing and the other curing methods of the porosity at 20mm depth from the surface is shown in Table 3-5. In the t-test results, if the calculated t value is greater than the theoretical t value (2.776 for a 95% confidence interval), the groups are categorized as not similar, if the calculated t value is less than the theoretical t value then the groups are categorized as similar.

Differences in the porosity between the samples shows that the drying caused a change in the amount of hydration and this, in turn, created more pores in the concrete. These additional pores could result in a reduction in strength at the surface. This can cause increased cracking and

reduced abrasion resistance. The increase in the diffusion coefficient depends on how interconnected the pores are. This will be investigated in a future section.

For the 0.15 kg/m^2/h evaporation rate, the t-test shows there is no significant difference in the porosity for the continuously wet cured samples and the samples with a delay in wet curing up until 6h. The sample with a delay in wet curing of 9h did show an increase in porosity at 20 mm and 60 mm from the surface but no difference at 100 mm from the surface. This means that for the evaporation rate of 0.15 kg/m^2/h that wet curing could be delayed up until 6h and there is no significant impact on the porosity but there is an impact after 9h of drying.

For the 0.55 kg/m^2/h evaporation rate, there is no difference for the sample where the wet curing was delayed 3h but there is a measurable difference for the sample where the wet curing was delayed 6h. The sample where the wet curing was delayed 9h showed even higher porosity at the surface. The t-test also shows the same result at the surface. This means that for this environment the wet curing could be delayed 3h at the surface without impacting the porosity of the sample.

For the highest evaporation rate of 0.85 kg/m^2/h, the porosity measurements show that the longer the sample is exposed to the environment, the higher the porosity of the sample at the surface. The student t-test also shows there is a statistical difference between the continuous wet curing and the other curing methods at the surface porosity. These measurements show that the surface porosity is significantly modified even after 2h of drying. This means that wet curing would need to be applied earlier than 2h in this drying environment to not impact the porosity of the sample.

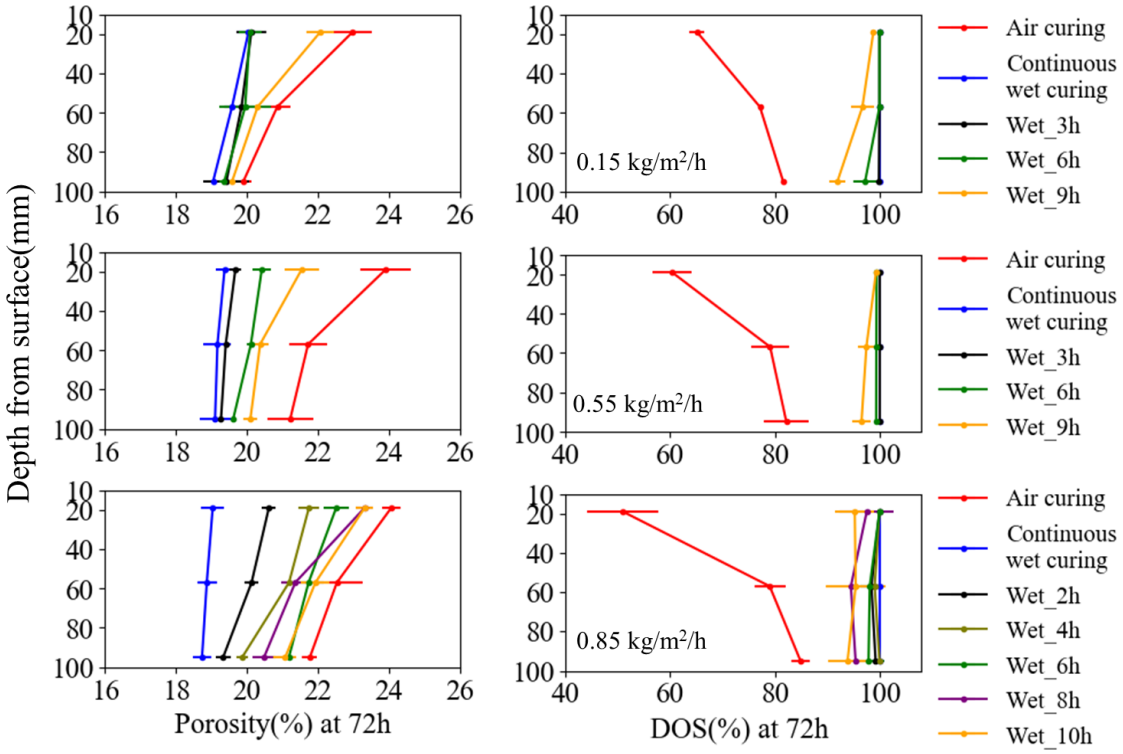

Figure 3-8. Porosity and DOS gradation profile along with the sample depth at 72h hydration at different environments.

Table 3-5. Student t-test result between continuous wet curing and the other curing methods in different environments on the porosity values at 20mm from the surface.

0.15 kg/m^2/h						
	Wet_3h		Wet_6h	Wet_9h		Air Curing
Continuous Wet	2.51		2.65	12.04		14.93
	similar		similar	Not similar		Not similar
0.55 kg/m^2/h						
	Wet_3h		Wet_6h	Wet_9h		Air Curing
Continuous Wet	2.14		6.28	17.94		32.25
	similar		Not similar	Not similar		Not similar
0.85 kg/m^2/h						
	Wet_2h	Wet_4h	Wet_6h	Wet_8h	Wet_10h	Air Curing
Continuous Wet	6.37	13	12.38	18.95	19.46	22.42
	Not similar	Not similar	Not similar	Not similar	Not similar	Not similar
1. The t-test hypothesis is that: the two group means are the same. 2. Parameters for the t-test: significance value $\alpha = 0.05$; degree of freedom = 4; theoretical t value = 2.776. All of these measurements are comparing the results at 20 mm from the surface.						

Because the electrical resistivity measurements are made continuously, they can be compared to the porosity. Further analysis shows that the slope or the gradient of the electrical resistivity measurement correlates to the porosity at 20 mm from the surface. These results are shown in Figure 3-9.

For the 0.55 kg/m^2/h and 0.85 kg/m^2/h evaporation rates, the porosity at 20 mm increased with an increase in the resistivity gradient. This increase in gradient means that more water has been lost to the sample. This means the concrete has had less water available for hydration and so this has impacted the porosity. For the 0.15 kg/m^2/h evaporation rate, there is little difference between the evaporation rate and the porosity for the sample at 3h and 6h.

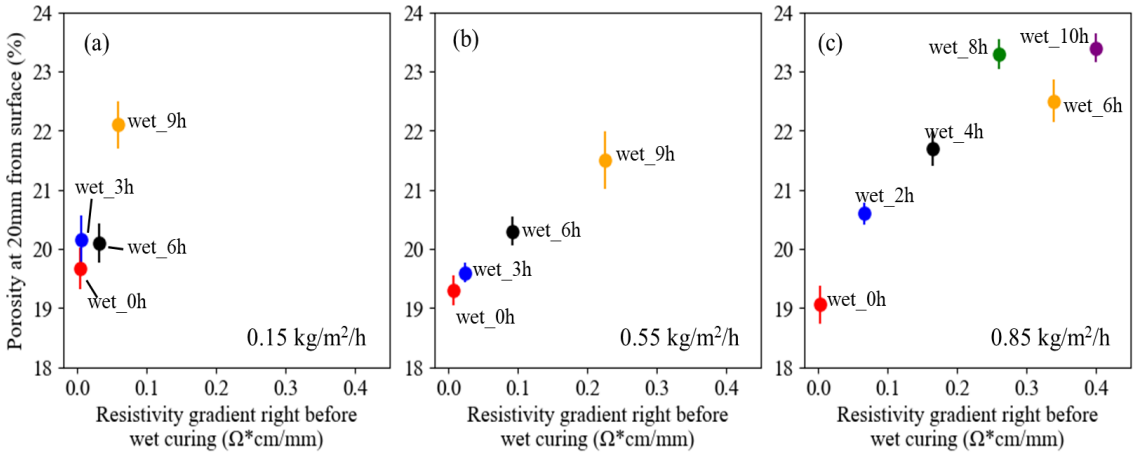

Figure 3-9. Porosity at 20 mm from the surface versus the resistivity gradient right before wet curing is applied for different drying environments.

3.3.5 Diffusion Coefficient

The diffusion coefficient for different evaporation rates and curing times is shown in Figure 3-10, and a t-test between continuous wet curing and the other curing methods is shown in Table 3-6. In the t-test results, if the calculated t value is greater than the theatrical t value (2.447 in this case for a 95% confidence interval), the groups are categorized as not similar, otherwise, the groups are categorized as similar.

In all cases, the continuously wet cured sample performed the best and the air cured sample performed the worst. Also, as the evaporation rate became more severe, the diffusion coefficient increased. As the diffusion coefficient increases, this means the resistance to outside chemical penetration also decreases and this decreases the durability of the concrete.

All the samples in the 0.15 kg/m^2/h evaporation rate seem to have a similar diffusion coefficient. A t-test was used to show that there is no statistical difference in these measurements. The results are shown in Table 3-6. This means that the drying did not impact the measured diffusion coefficient. In the 0.55 kg/m^2/h evaporation rate, all the curing periods have a similar diffusion coefficient except for the air cured sample. It does not appear that the diffusion coefficient detects

a difference in delaying the curing to be placed on the concrete until at least a 9h delay, and this shows agreement with the t-test results. The diffusion coefficient does not seem to be as sensitive to the delay in curing as does the porosity measured in the previous section.

At the 0.85 kg/m^2/h evaporation rate, the continuously wet cured sample has a higher diffusion coefficient than the other drying environments. This could be caused by the higher temperature impacts on the uniformity and quality of the hydration products. Also, when the wet curing is delayed this causes the diffusion coefficient to increase almost linearly with time until 8h. The results also show that even delaying the application of the wet curing by 2h will cause an increase in the diffusion coefficient. The t-test results also show that all the delayed wet curing has a statically different mean from that of the continuously wet cured sample. This shows the importance of placing wet curing on the surface quickly in a high drying environment as a 2h delay will impact the diffusion coefficient.

Care should be taken in evaluating the diffusion coefficient of the air cured samples to the other evaporation rates. The air cured samples will have a lower amount of water in their pores from drying that was never replenished with applied water. When the tracer solution is added to measure the diffusion coefficient then these samples it will be drawn in by a combination of diffusion and absorption. This will make the measured diffusion coefficient appear to be larger. This doesn't occur in the wet cured samples because the water added to the surface increases the DOS and so the movement of the outside fluid into the concrete would only be caused by diffusion. This diffusion coefficient is a good indication of how the concrete will perform after a severe drying period.

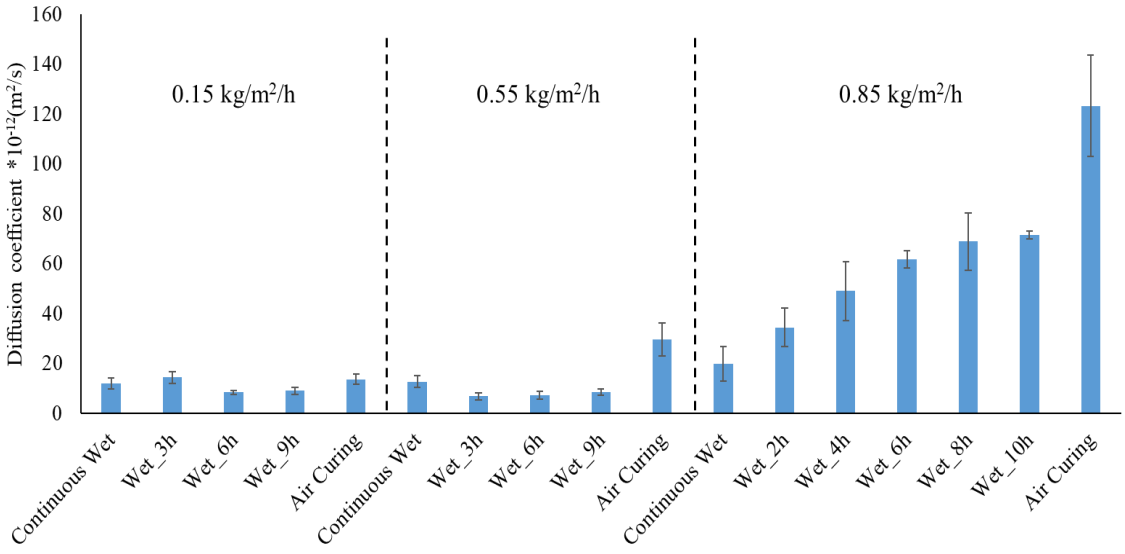

Figure 3-10. Diffusion coefficient of the mortar samples under different curing methods.

Table 3-6. Student t-test results between continuous wet curing and the other curing methods in different environments on the diffusion coefficient.

0.15 kg/m^2/h				
	Wet_3h	Wet_6h	Wet_9h	Air Curing
Continuous Wet	1.46	1.03	0.75	1.06
	similar	similar	similar	similar
0.55 kg/m^2/h				
	Wet_3h	Wet_6h	Wet_9h	Air Curing
Continuous Wet	2.35	2.4	1.66	4.87
	similar	similar	similar	Not similar

0.85 kg/m^2/h						
	Wet_2h	Wet_4h	Wet_6h	Wet_8h	Wet_10h	Air Curing
Continuous Wet	2.87	4.27	10.93	7.34	14.55	9.63
	Not similar	Not similar	Not similar	Not similar	Not similar	Not similar

1. The t-test hypothesis is that: the two group means are the same.
2. Parameters for the t-test:
significance value $\alpha = 0.05$; degree of freedom = 6; theoretical t value = 2.447.

Since the diffusion coefficients of different wet curing methods in the 0.85 kg/m^2/h evaporation rate environment are statistically different, the relationship between diffusion coefficient and resistivity gradient immediately before application of the wet curing is shown in Figure 3-11. It shows a linear relationship between resistivity gradient and diffusion coefficient at the highest evaporation rates. Other relationships are not shown because the evaporation rate was not high enough to make a statistically measurable impact on the diffusion coefficient.

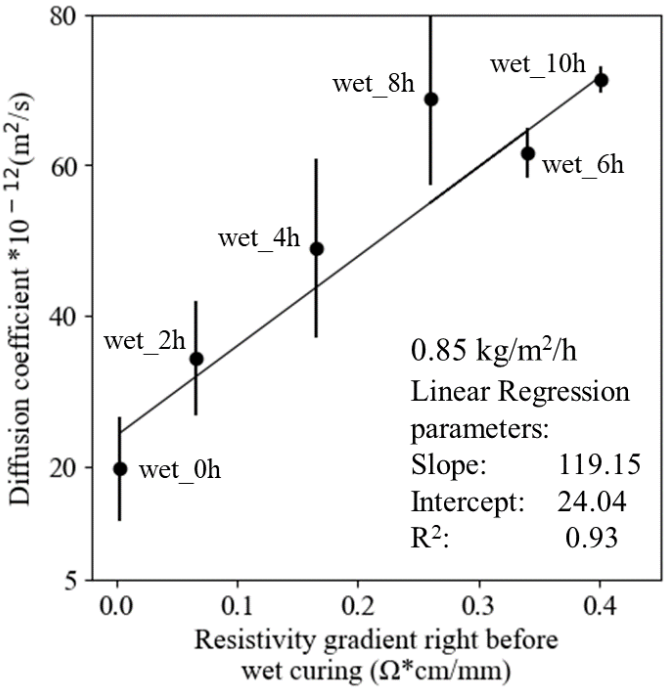

Figure 3-11. Diffusion coefficient shown as a function of resistivity gradient along with sample height right before the application of wet curing at the evaporation rate of 0.85 kg/m^2/h.

3.4 Practical Significance

This work compares the resistivity, diffusion coefficient, porosity, and DOS of wet curing at different times and air curing on concrete and mortar samples. The results show that the critical timing for applying wet curing is based on the evaporation rate of the concrete.

The work also shows that the porosity measurements in this work are more sensitive to changes in early age drying than the diffusion coefficient. Table 3-7 shows the critical time for applying the wet curing to the surface for porosity and diffusion coefficient for the three different drying environments investigated.

Table 3-7. Allowable delay in wet curing before performance is compromised.

Maximum Evaporation Rate	Allowable delay in wet curing before performance is compromised based on the statistical significance of porosity or diffusion coefficient at 20 mm from the surface.	
	Porosity	Diffusion Coefficient
0.15 kg/m^2/h	6h	>9h
0.55 kg/m^2/h	3h	9h
0.85 kg/m^2/h	<2h	<2h

This shows that in the least severe drying environment of 0.15 kg/m^2/h evaporation rate, the wet curing can be delayed for 6h and there will be no statistically significant change in the porosity or diffusion coefficient at 20 mm from the surface. When the drying rate is increased to 0.55 kg/m^2/h, wet curing can be delayed for 3h before there is a statistically significant change in the porosity or diffusion coefficient. For the highest rate of evaporation of 0.85 kg/m^2/h evaporation rate, the delay must be less than 2h. It should be noted that Table 3-7 shows the exact time when performance is found to be compromised and that it is typical to use a safety factor for specification requirements. Also, this work only used a single concrete mixture and the testing only examined three different drying environments. However, with more measurements and a wider range of materials and drying environments then a recommendation could be made on safe delays in applying wet curing.

There are two possible ways to future implementation of these findings. First, a specification could be used where the evaporation rate in the environment is measured, and based on the maximum evaporation rate a certain delay is allowed in applying the curing to the concrete. Handheld weather stations already exist that could do this by measuring all of the variables and

the nomograph from Figure 3-1. However, there has been some question about the validity of the nomograph and also criticism that the recommendations of the nomograph do not depend on the type or quality of the concrete or the solar radiation [42].

Another option would be to measure the resistivity gradient in the field of the fresh concrete. This measurement would capture the difference in moisture loss between the top and bottom of the sample. This would allow you to measure the impact of the environment on the concrete while taking into account the bleeding rate of the concrete. For this to be a practical approach, work needs to be done to understand what resistivity gradient is allowable before the properties of the material are compromised.

It is also important to note that this work suggested the allowable limits based on the changes in the porosity. It is not clear how these changes would relate to a loss in other physical properties like abrasion resistance or cracking resistance. These measurements of the direct properties would be more useful to determine the impact of the curing on the concrete. More measurements would provide greater insights into when a critical property is impacted by the delay in the wet curing.

3.5 Conclusions

The influence of wet curing at different times was investigated in this study. The experiments were conducted under three different evaporation conditions for the first 72h of hydration. The diffusion coefficient, porosity, DOS, and resistivity of the sample were measured and compared between curing methods. The following conclusions can be drawn:

- The electrical resistivity measurements are able to show the loss in moisture over time in all three drying environments. When wet curing was applied to the surface after 9h of drying for the samples in the 0.15 $kg/m^2/h$ and 0.55 $kg/m^2/h$ evaporation rate, the resistivity decreased to values similar to the sample was never allowed to dry. However,

in the 0.85 kg/m^2/h evaporation rate for at least 2h, the resistivity did not decrease to the same level as the sample continuously wet cured.

- At the 0.15 kg/m^2/h evaporation rate environment, delaying the wet curing for 6h did not impact the porosity of the sample. The diffusion coefficient was not impacted when the wet curing was delayed for 9h.
- At the 0.55 kg/m^2/h evaporation rate environment, delaying the wet curing for 3h did not impact the porosity of the sample. The diffusion coefficient was not impacted until the wet curing was delayed for 9h.
- The average porosity at 20 mm in depth is related to the resistivity gradient right before the application of curing in the 0.85 kg/m^2/h evaporation rate. The resistivity gradient was also useful in predicting the change in the diffusion coefficient in the 0.85 kg/m^2/h evaporation rate. This shows that the resistivity gradient in the sample during curing could be used to track changes in the surface porosity and the diffusion coefficient from drying.

This work would benefit from additional testing done in the field to verify the measurements and also to compare the predicted performance with a wider range of materials; however, the results show promise for establishing a method to measure the impacts of delaying wet curing in different environments on the porosity and diffusion coefficient of concrete.

CHAPTER IV

MEASURING EFFECTIVE FREEZE-THAW CYCLES IN THE FIELD

4.1 Introduction

The durability and service life of cementitious material is impacted greatly by the surrounding environments. Field structures are continuously interacting with the environments and this interaction can cause durability issues. An important durability issue is freeze-thaw damage [43, 44]. The temperature and degree of saturation (DOS) of a cementitious material play a critical role in the freeze-thaw durability of cementitious materials [45–49]. The degree of saturation is defined as the percentage of voids that are filled by water in a porous system, and it's determined by ASTM C642 with some minor changes where the samples were saturated within a vacuum chamber instead of boiling in water.

Previous freeze-thaw studies have shown that once a critical DOS is reached, this is typically between 78% and 91%, freeze-thaw damage will begin to initiate in the past [12, 13]. This means that concrete that is continually exposed to moisture raises the probability of freeze-thaw damage. In this work, an average DOS of 85% is chosen as the critical DOS for analysis. Besides the level of freeze-thaw damage, the DOS is also important in the temperature that a cementitious material freezes [50, 51]. Studies have shown that as the DOS increases then the temperature at freezing will approach 0 ^{o}C [51]. Also, the amount of ice that forms will increase with a higher DOS [50].

As a result, understanding the DOS in field concretes exposed to water, such as an area with poor drainage, can give great insight into how to design concrete to resist freeze-thaw damage. Unfortunately, lab experiments such as ASTM C666 [14] are typically conservative but they do not accurately represent the DOS and freezing rate of structures in the field. For example, the ASTM C 666 samples are constantly surrounded by moisture and the freezing rates are around 4 to 9 times faster than what is experienced in the field [52–55].

Making field measurements of DOS and ice formation is not trivial. Methods are needed that are reliable and economical. Measuring the resistivity of cementitious materials has been used since 1928 [56]. This measurement technique has been used to measure hydration [18, 57], chloride transport [58, 59], corrosion [60], cracking [61, 62], as well as measuring DOS of cementitious materials. Electrical resistivity is also a useful tool to study freezing concrete [63–66]. A previous study used electrical resistivity to assess the freezing process of concrete [65]. The study of freeze-thaw performance would benefit from investigating concrete performance in complicated wetting, drying, and freezing environments in the field. Also, it would benefit from simultaneously measuring the DOS and the freezing response of the concrete. This paper aims to fill some of these gaps and make important observations that can be extended to additional sites in the future.

Resistivity is widely used to measure concrete because of its convenience, efficiency, useful measurements, and ease of operation. The influence of specimen geometry, temperature, DOS, and pore solution chemistry must be considered when interpreting the results of electrical measurements. A previous publication tracked water penetration by using electrical measurements and taking into account the electrode position and sample geometry and making corrections for sample geometry by using finite element models [67]. This work does not make these same corrections but instead carefully controls variables and uses calibration samples [68–71]. In this work, the field samples and calibration samples have the same configuration and are

from the same mixture design, the resistivity relationships established for the calibration samples are then applied to the field samples.

This work reduces the number of variables by using a single mortar mixture that is more than 60 d old in all of the experiments. Calibration samples are used in the lab to better understand the relationship between temperature, DOS, and ice formation. The calibration data is then used in the field to compare the weather at two locations and how it impacts the temperature, DOS, and ice formation at different depths within the specimen. This provides a systematic way to compare the impact of the weather in these two locations.

These measurements can provide critical data and new observations to quantify the impact of the environment on the freeze-thaw durability of cement-based materials. This fills a needed gap in the knowledge of how weather impacts the durability of concrete structures. This approach is used at two different sites in this paper but is being extended to close to 40 others. This work establishes the measurement methods and provides important insights. This new information can lead to improved concrete designs that are better tailored for their environment. This will reduce the cost and improve the sustainability and constructability of concrete structures.

4.2 Experimental Methods

4.2.1 Field Sample Preparation

The field samples were made from a mortar mixture and cast into 152.4 mm in diameter by 228.6 mm tall plastic cylinders. The mixture proportion by volume is shown in Table 4-1. The water-to-cement ratio (w/c) was 0.45. The cement used for the mortar mixture met the requirements of an ASTM C150 Type I Portland cement. The chemical compositions of the cement are shown in Table 4-2. The fine aggregate used was local natural sand and met the requirements of ASTM C33. No supplementary cementing materials (SCM) were used in the samples to minimize the change in resistivity over time [72].

Table 4-1. Mixture proportion of mortar

	Cement	Water	Fine Aggregate	Air
Volume (%)	18.5	23.4	52.7	4.4

Table 4-2. Chemical composition of cement

	SiO_2	Al_2O_3	Fe_2O_3	CaO	MgO	SO_3	Na_2O	K_2O	C_3S	C_2S	C_3A	C_4AF	LOI
Cement (%)	21.1	4.8	3.1	64.5	2.33	3.2	0.17	0.58	50	23	7	9	2.6

The configuration of the mortar samples is shown in Figure 4-1. Four type T thermocouples and eight pairs of 4-40 threaded stainless steel rods (2.8 mm in diameter, and 40 threads per 25.4 mm) were held in place by drilling holes in the empty mold along with the depth at known locations. Some glue was used at each drilled hole to hold the thermocouples and rods in place. The steel rods had a center-to-center distance of 92.7 mm at each depth. The top steel rods and thermocouples were installed above the mortar surface and exposed to the air to detect water accumulation and air temperature respectively. The surface of the mortar samples was 25.4 mm lower than the mold top to promote water accumulation. This space forces any rainwater to be retained and evaporate naturally. This is done to mimic concrete with poor drainage.

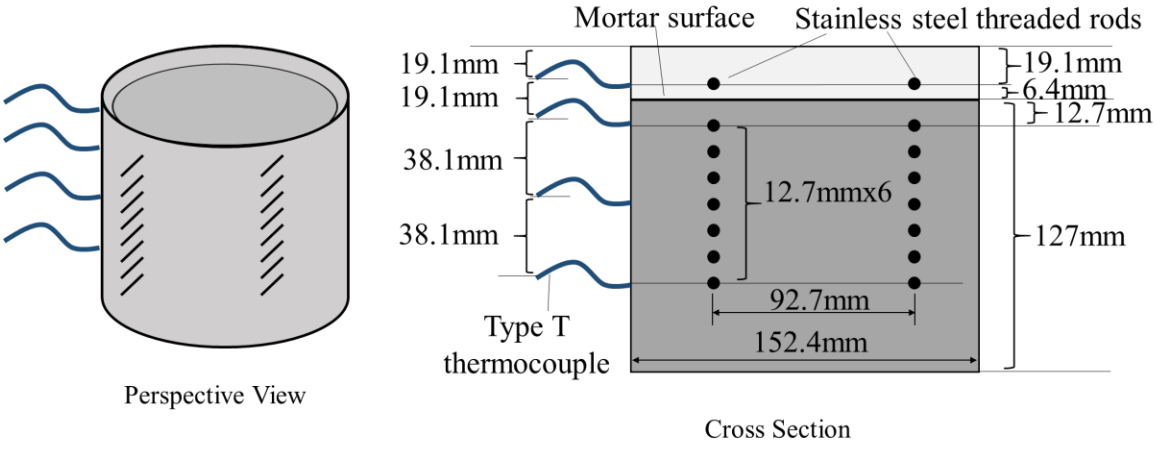

Figure 4-1. Configuration of the thermocouples and steel rods of the mortar sample.

The mortar samples were wet cured for 60 d by adding water on their top and covering the top with a plastic tarp. This was done to keep the samples at a high DOS before they were sent out to the field. After the samples were over 28 days old, copper wires of 16 AWG were soldered on each steel rod. The copper wires extended the distance between the mortar sample and the data logger. Electrical tape was used to cover the copper wires after they were soldered on the steel rods to isolate the circuit from the outside concrete cover.

As the mortar sample dries then it will shrink [73]. To avoid a gap created by shrinkage between the sample and the plastic mold, a low shrinkage mortar is used to seal the edge of the sample along with the plastic mold. The low shrinkage mortar was the same mixture from Table 4-1 but it used a 9% replacement of the water with a shrinkage reducing admixture. Each block contained two mortar samples so that redundant measurements can be made. The fiber-reinforced concrete cover protected the wiring and samples, it also ensured the samples stayed upright and it insulated the samples to simulate a sample within a concrete pavement. The surrounding concrete used 0.45 w/cm concrete mixtures with macro synthetic fibers at 2% by volume of the mixture. The size of the final concrete block is 457 mm x 305 mm x 178 mm.

The equipment used to monitor the performance of the mortar samples is shown in Figure 4-2. The mortar specimens were connected into the instrument box through thermocouples and extended copper wires for temperature and resistivity measurements respectively. A data logger was installed inside the instrument box and powered by a 12 voltage battery charged through the solar panel. The instrument box was fixed 0.9 m above the ground.

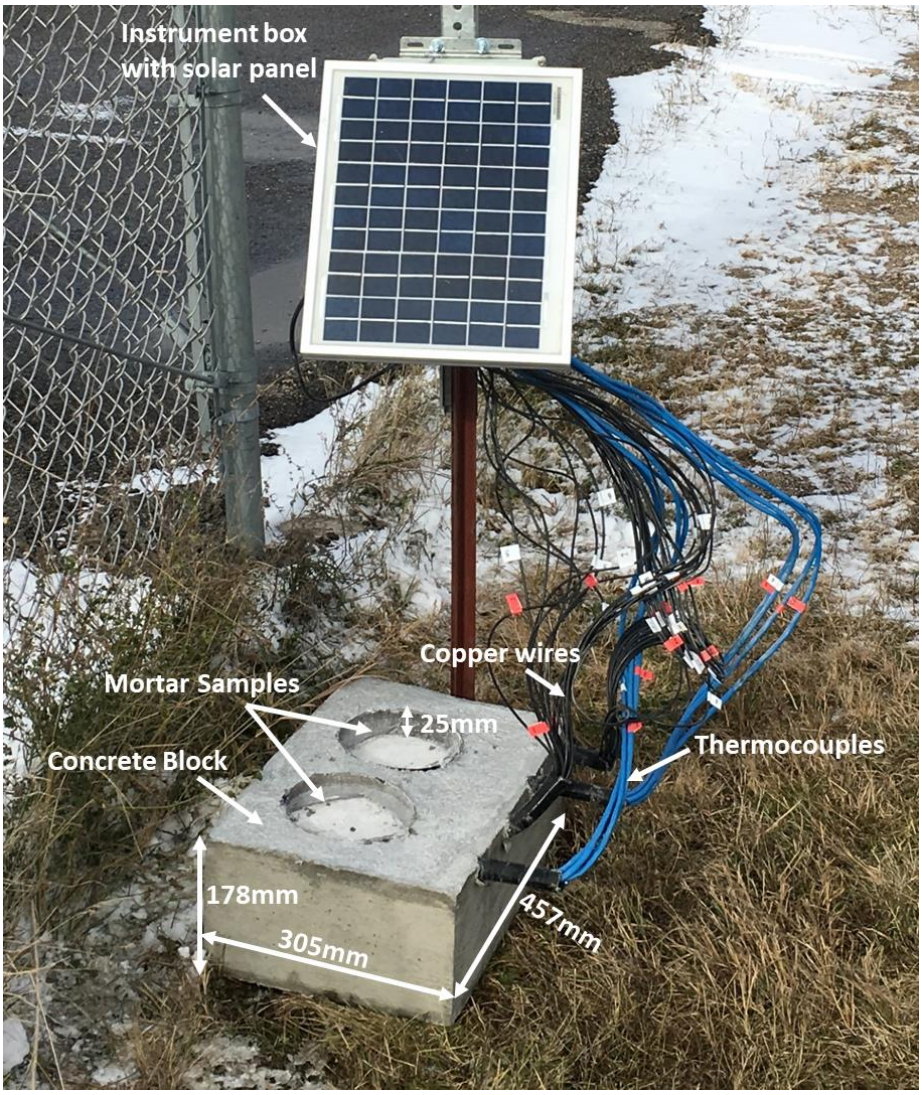

Figure 4-2. Configuration of the instrumentation box.

The data logger is a printed circuit board (PCB) developed for resistivity and temperature monitoring. The PCB was designed with KiCAD and programmed with the Arduino platform. An ATmega 2560 was used as the central processing unit. The circuit used a clock to record the time of each measurement. The resistivity and temperature are measured every 30 minutes and the data is recorded on an SD card. The data was then retrieved into a USB drive for later analysis. Several multiplexers were embedded into the PCB to expand the measurement ability to 16 channels.

A 12-Bit impedance converter AD5933 was the sensor used to measure resistivity. The frequency generator of the AD5933 allows the mortar specimen to be excited at a frequency of 4KHz, at which the imaginary impedance is close to 0, which means the concrete acts as a pure resistor, and the real impedance is used as the bulk resistance of the mortar specimen in ohms [16]. This simplifies the interpretation of the impedance response of the concrete sample. To get the resistivity of the mortar sample, Equation 4-1 was used.

$$Resistivity\ (K\Omega * cm) = bulk\ resistance\ (\Omega) * A\ (mm2)\ /\ L\ (mm)/10000 \quad \text{Equation 4-1}$$

In Equation 4-1, A is assumed to be the rectangular cross-sectional area of the electrode perpendicular to the signal. Since the electrode is 2.8 mm in diameter and approximately 121 mm long, the area is taken as 338.8 mm^2. The distance between the electrodes, L, is 92.7 mm. More details on how the impedance and temperature sensors work in the data logger could be found in Appendix F.

4.2.2 Calibration Sample Conditioning

The calibration samples were made with the same mortar mixture as the field samples and cured in the same way but did not contain thermocouples. These samples were first conditioned at a fixed relative humidity and stored in an environmental chamber according to ASTM E-04 [74]. After the samples reached a constant mass, a 40g sample was removed and tested for DOS according to ASTM C642. To get a wider array of DOS, some samples were vacuum saturated and then dried to meet a target DOS. This was done to avoid drying samples in an oven that may cause microcracking. This process was completed to obtain a DOS of 36.2%, 45.6%, 65%, 75%, 86.8%, 90%, 95%, and 100%. A summary of the different humidity and DOS are shown in Table 4-3.

Table 4-3. DOS of the calibration samples.

Humidity (%)	DOS (%)	The standard deviation of DOS (%)	Freezing temperature (°C)	Thawing temperature(°C)
59	36.2	0.21	-4.8	0.0
75	45.6	0.10	-4.9	0.0
85	65.0	0.16	-4.2	0.0
-	75.0	0.07	-4.6	0.0
100	86.8	0.11	-2.8	0.0
-	90.0	0.03	-2.6	0.0
-	95.0	0.11	-2.5	0.0
-	100.0	-	0.0	0.0

The temperature of the sealed calibration samples was changed from 49°C to -18°C at an interval of 2°C. Each temperature was maintained for 6 hours to minimize any temperature gradients. After reaching a uniform temperature, the resistivity of each sample was measured. The freezing and thawing temperature is reported for each DOS. More details are provided later in the document about these measurements. The measured freezing temperature is about 3°C higher than other publications [51]. This might be because the samples used in this study are $1.28x10^8$ times larger in volume than the previous work (25.4mm×25.4mm×300mm in the previous work). Larger samples have a higher probability for ice nucleation and so the ice is observed at a higher temperature.

4.2.3 Determining the Number of Effective Freeze Thaw Cycles

In this work, an effective freezing event is expected to occur if the DOS is above 85% and if ice forms in the sample. This work will first find the relationship between temperature, DOS, and ice formation. Then it will verify the formation of the ice in the field with the electrical resistivity measurements. Ultimately, the number of effective freeze-thaw cycles at the two locations will be a function of the predicted ice formation, measured DOS before the ice forms, and then this will be validated by directly observing the ice formation in the samples.

4.3 Results and Discussion

4.3.1 Relationship between Resistivity, Temperature, and DOS for the Mortar Samples

Figure 4-3 shows the resistivity of the samples with different DOS as a function of temperature. The measured value of the calibration samples is also compared with the theoretical model between resistivity and temperature of concrete [75]. The model is described in the following Equation 4-2.

$$Z_{ref} = Z \times exp[(-Ea)/R \times (1/(T + 273) - 1/(T_{ref} + 273))] \quad \text{Equation 4-2}$$

Where:

Z and Z_{ref} = resistivity of concrete, KΩ*cm,

T and T_{ref} (typically 23°C) = temperatures of the concretes, °C,

Ea = activation energy of conduction, kJ/mol, and

R = universal gas constant, 0.008314 J/(mol K).

The calculated activation energy of each DOS is shown in Table 4-4. The resistivity measurements match the model when the temperature is greater than 0°C. When the temperature is below 0°C, the measured resistivity can be much higher than the theoretical value. This is because of the phase of water and higher activation energy (Ea) is expected to use.

Table 4-4. The activation energy of different DOS of the concrete sample.

DOS (%)	36.2	45.6	65	75	86.8	90.0	95.0	100.0
Activation energy (kJ/mol)	33	30.1	27	25	23	23	23	23

For all the samples, the resistivity decreases as the temperature increases. The increase in temperature also increases ion mobility. This higher ion mobility causes the resistance to decrease [70, 76–78]. It is also noticed that a sample with a higher DOS gives a lower resistivity

for a given temperature. In the higher DOS sample, the additional free water allows more ion movement, and this causes a lower resistivity.

There is a non-linear relationship between resistivity and temperature as shown in Figure 4-3. The non-linearity is more obvious when the temperature is below the freezing point of water. Since ice has a higher resistivity than liquid water, this will cause an increase in resistivity [64, 79]. To learn more, the rate of the change of the resistivity versus temperature (dR/dT) is plotted in Figure 4-4. From Figure 4-4, the freezing temperature can be estimated by finding the point where the slope changes. The freezing point of different DOS values is summarized in Table 4-3. The freezing temperatures show that samples with a DOS higher than 85% would freeze at a higher temperature than those with a lower DOS. This is consistent with the previous literature [51]. The thawing temperatures were obtained in the same way and the results are shown in Figure 4-5. The thawing point was taken as the point where the water was completely melted. The temperature was increased from -16°C to 15°C, and the change in slope near 0°C was selected as the thawing temperature. The thawing temperatures of the samples with different DOS gave a consistent value of 0°C. This was consistent with the findings in previous research [50].

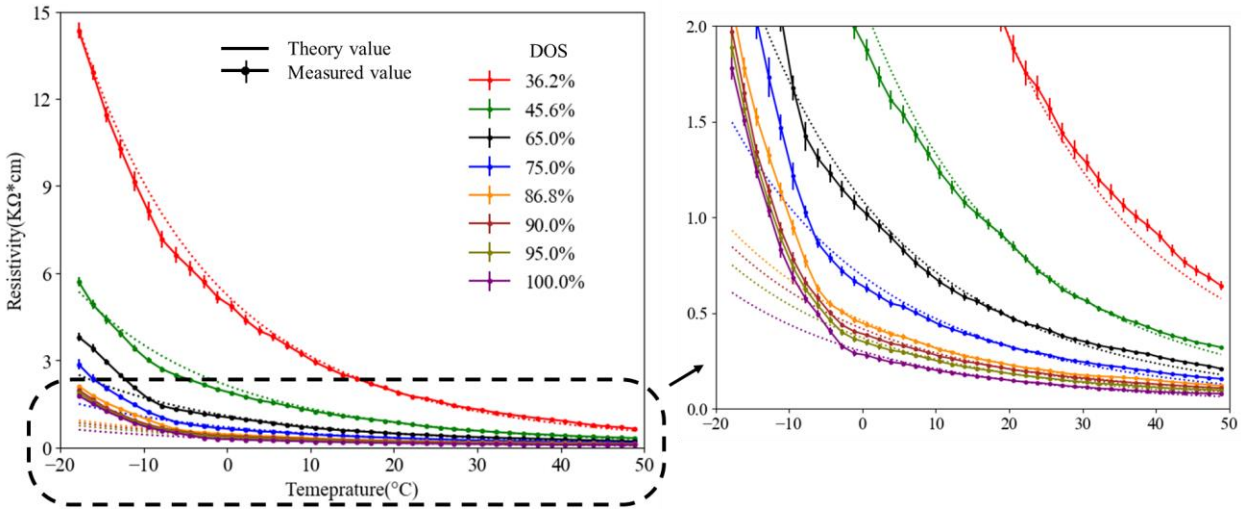

Figure 4-3. Resistivity as a function of temperature for samples with different DOS.

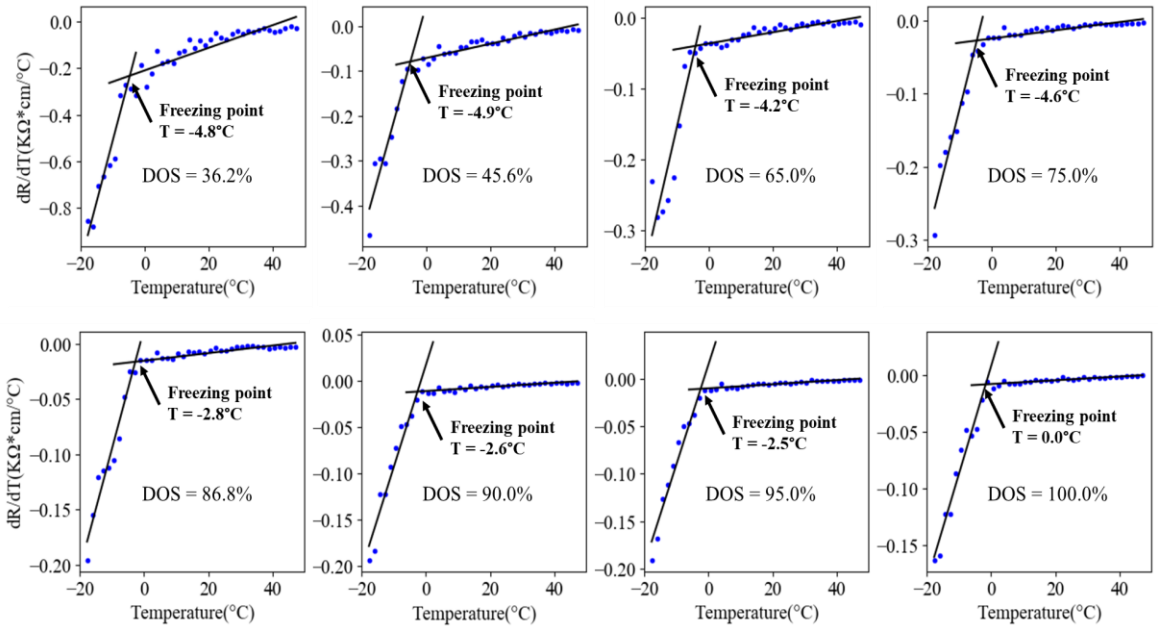

Figure 4-4. Resistivity changing rate over temperature (dR/dT) during freezing.

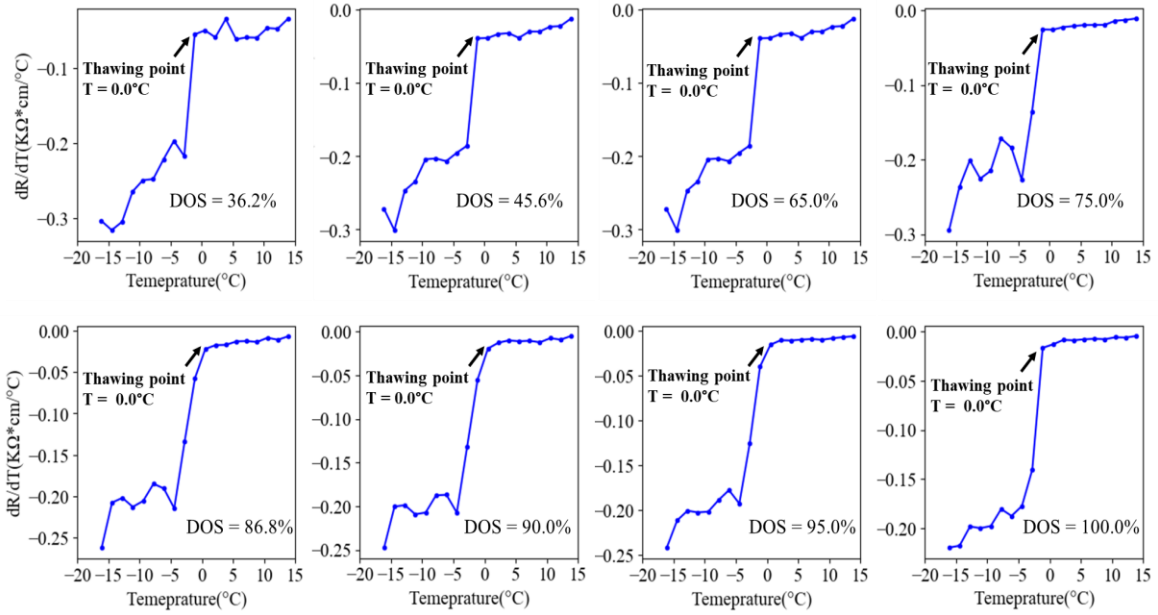

Figure 4-5. Resistivity changing rate over temperature (dR/dT) when thawing.

The freezing temperature versus DOS is shown in Figure 4-6. A 5-degree polynomial function is used to fit the data. The equation used is shown in Equation 4-3. The fitted parameters are given

in Table 4-5. The r2 value of the fit is 0.944, which is higher than a fourth or sixth-degree polynomial fit.

$$Freezing\ Temperature = a_0+a_1*DOS+a_2*DOS^2+a_3*DOS^3+a_4*DOS^4+a_5*DOS*^5 \quad \text{Equation 4-3}$$

Table 4-5. Parameters value in Equation 4-3.

Parameters	a_0	a_1	a_2	a_3	a_4	a_5
value	3.81e-08	1.2e-05	1.4e-03	-8.1e-02	2.3e+00	-2.9e+01

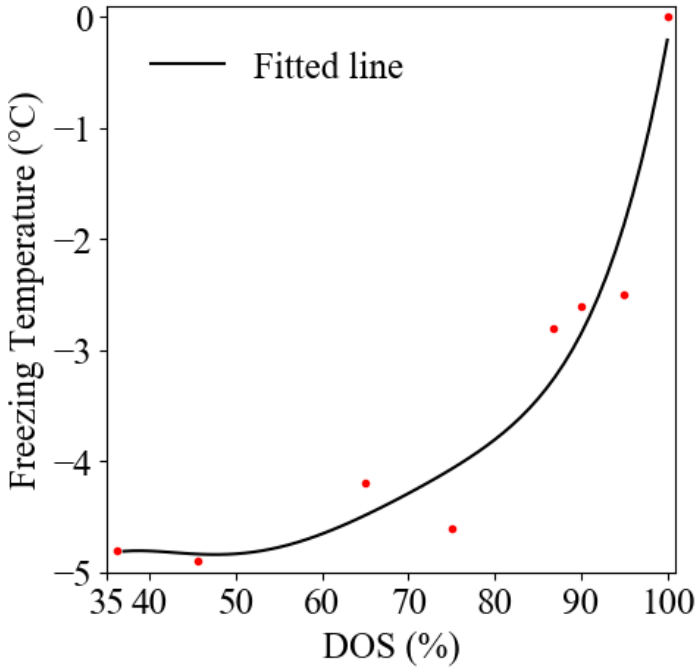

Figure 4-6. Freezing Temperature is shown as a function of DOS.

Figure 4-7 shows the DOS as a function of resistivity at different temperatures. For easy observation, only the data from 47 to 11°C is shown. The whole range of temperature change from 49°C to -18°C is shown in Appendix G. The results show that for a given DOS that the resistivity is higher as the temperature decreases. The data is plotted in this way to show how the

resistivity and temperature measured in the field can be used to find the DOS. An example of this is shown in Appendix G.

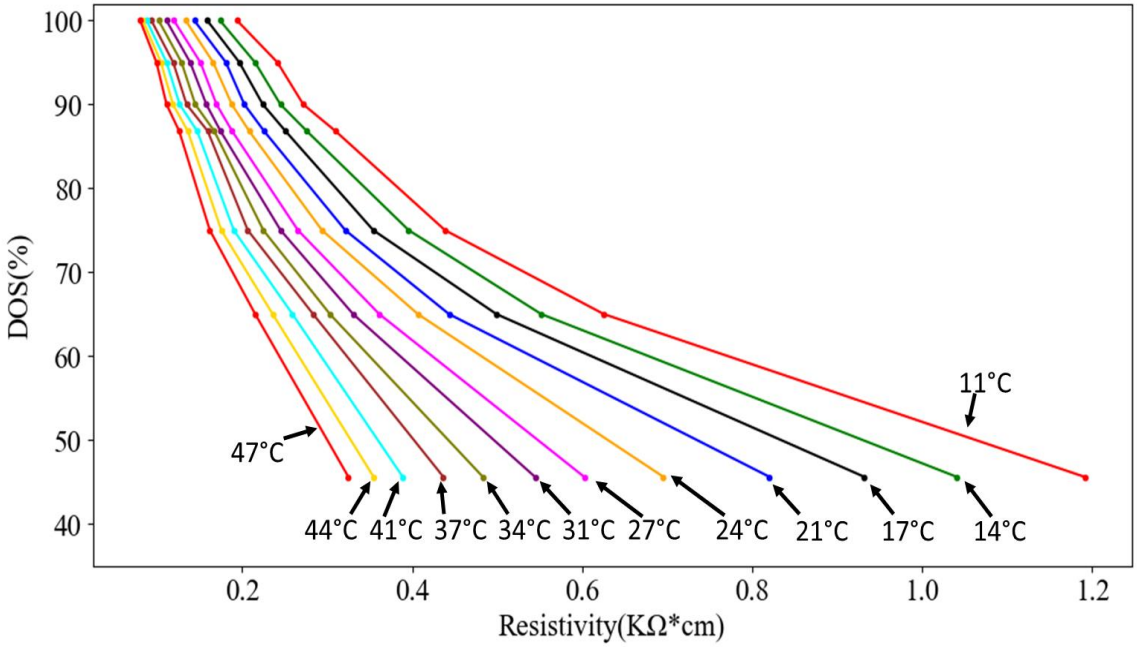

Figure 4-7. DOS represented as a function of resistivity at temperatures from 47°C to 11°FC.

4.3.2 Measurement of the Temperature, Resistivity, and DOS of Field Samples

Figure 4-8 shows the temperature and resistivity response of the field samples installed in Stillwater, Oklahoma USA in September 2019. For easy observation, only 3 depths are shown. The curve of other depths shows a similar response. The temperature of the weather station data in Figure 4-8(a) is obtained from the Local Climatological Data (LCD) of the National Centers for Environmental Information [80]. The weather station is installed in the Stillwater regional airport, which is about 2 miles away from the field sample.

Figure 4-8(a) shows that the mortar sample has a uniform temperature along with its depth and the temperature of the mortar samples shows a good agreement with the local weather station but with higher daily peaks. The average difference is within 1.7°C between the weather station and

the field samples. This temperature difference is likely from differences in the specific heat capacity of the mortar compared to the air and the impact of radiant heat [81, 82]. The diurnal amplitude of the temperature is about 33°C. Figure 4-8(b) shows the resistivity response of the field sample along with its depth. The resistivity is also fluctuating and appears to be inverse to the temperature changes. The resistivity is not uniform along with the sample depth. The top depth generally gave a higher resistivity value than the lower depths. This is likely caused by a lower saturation level or a lower DOS near the top of the sample. This indicates that a DOS gradient formed along with the sample depth.

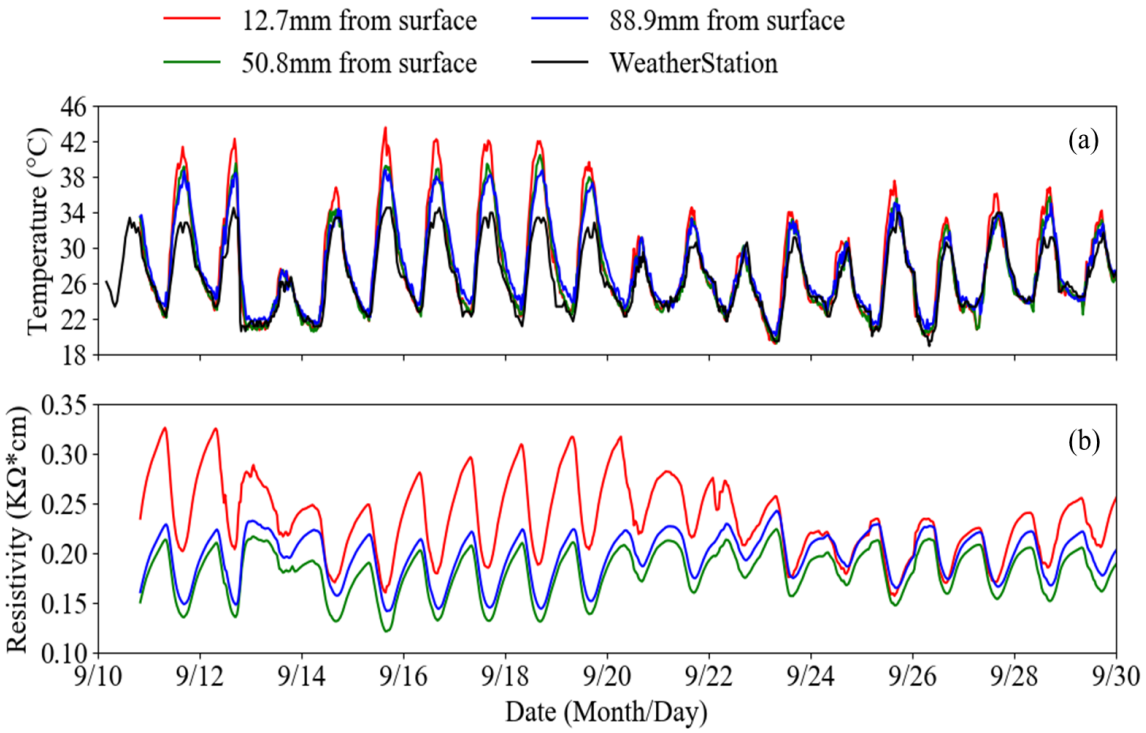

Figure 4-8. Field sample response in September 2019 in Stillwater, OK: (a) temperature response, (b) resistivity response.

By using the laboratory calibration samples, the resistivity and temperature measurements can be used to determine the DOS at different depths. These results are shown in Figure 4-9(a). Figure 4-9(b) shows the precipitation from the weather station.

Figure 4-9(a) indicates that the measurement at 12.7 mm from the surface was the most sensitive because it was the closest to the surface. For example, on 9/12, There was a rain event and the DOS at 12.7 mm from the surface increased rapidly from 73% to 80%. The DOS continued to increase over the next 24 h to about 85% DOS and then it started to decrease. On 9/22, a rain event increased the DOS from 75% to 82%. In the latter days, several small amounts of precipitation occurred and the DOS at 12.7 mm depth continued increasing to 87%.

It is interesting that at the 50.8 mm and 88.9 mm depths the DOS do not immediately change after a rain event and they do not seem to be immediately impacted by the subsequent drying. However, when moisture was present on the surface for extended times, as occurred on 9/14, it can be observed that the DOS at 50.8 mm depth does increase. This shows that the DOS increases around 20 h after the rainfall. This is shown with a rectangular box and note. This seems to indicate that the water from the rainfall has penetrated to 50.8 mm and increased the moisture level.

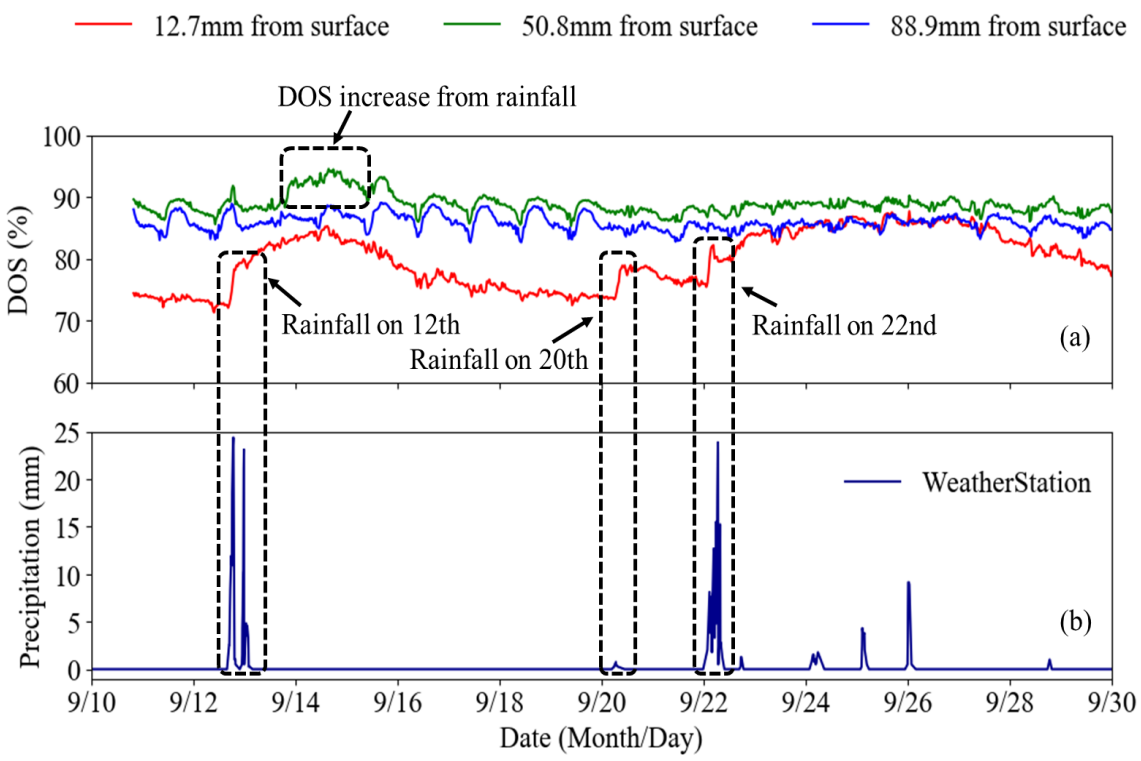

Figure 4-9. (a) DOS of field sample in September 2019, Stillwater, OK, (b) precipitation from the weather station.

Figure 4-10 shows the DOS gradient along with the sample depth on 9/11, 9/14, and 9/18 along with a horizontal line showing the assumed critical degree of saturation of 85%. This is an average degree of saturation and would be conservative for most concrete mixtures.

These dates are chosen as they are before and after a rain event. From the 11th to the 14th, the overall DOS within the sample increased by at least 8% at 40 mm and higher. At 12.7 mm from the surface, the DOS increased by more than 10%. After four days of drying the DOS was almost the same as it was before drying. These results show how precipitation events can locally raise the moisture level of mature concrete to 50.8 mm into the depth and this increase in moisture can lower over time.

This work also shows that a freezing event that occurred on 9/11 would only be expected to damage between 40 mm and 80 mm in the sample. However, after the rain event, the entire sample would be expected to be damaged. This emphasizes how important it is to understand both the moisture content in the concrete as well as the temperature. It also shows how complicated the moisture profile can be and how it is impacted by precipitation events.

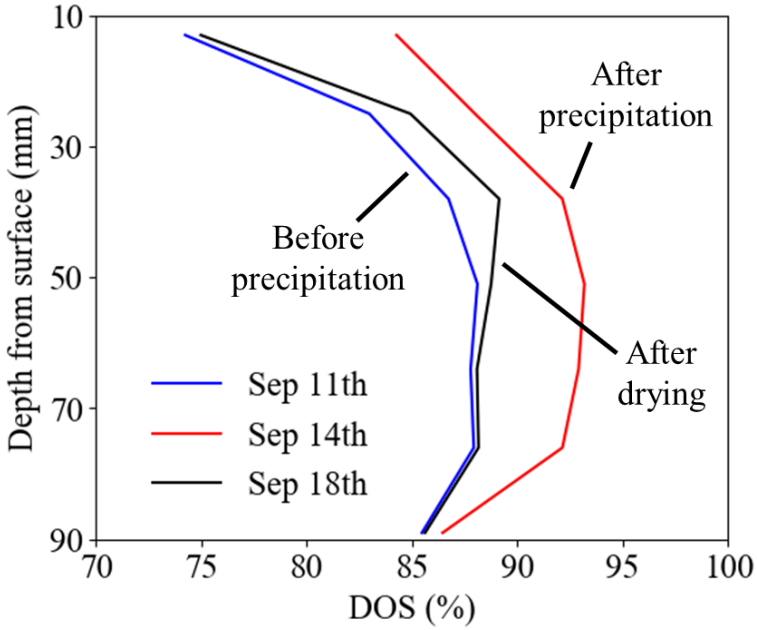

Figure 4-10. DOS gradation on September 11th and 14th, 2019, Stillwater, OK.

4.3.3 Comparing the DOS between Field Samples Installed at Different Locations

In this section, the field samples installed at two different locations are compared. These locations are approximately 350 mi apart and have similar latitudes. Both locations are in the same state but have different average relative humidity and average precipitation. More details about the two locations are shown in Table 4-6.

Table 4-6. Information of the two locations in Oklahoma State for 2019.

Location	latitude	longitude	Average temperature(°C)	Average RH (%)	Average precipitation (mm)	Number of times air temperature below 0°C
A	36.8° N	101.4° W	12.8	60	0.004	120
B	36.1° N	97.1° W	15.3	69	0.017	67

A subset of the temperature and DOS from 9/11 to 9/19 is shown in Figure 4-11 for the two locations. By comparing the temperature graphs, location B has a higher average temperature. This is consistent with the ranking of the average annual temperatures shown in Table 4-6.

In Figure 4-11, the dashed line in the DOS plots are times when ice formation occurs. This will be discussed in the next section. The DOS of the 12.7 mm depth was always lower than the 50.8 mm and 88.9 mm depths. This means the surface is less saturated than deeper into the concrete. Further, location A had the lowest DOS, followed by location B. The DOS observation is consistent with the average RH of the three locations. The RH and precipitations of the two locations from weather stations within the same time range are shown in Appendix H.

While the relative ranking of the moisture content and temperature at different depths is useful, it does not provide insights into the ice formation, or the amount of damage expected from the ice formation. This will be investigated next.

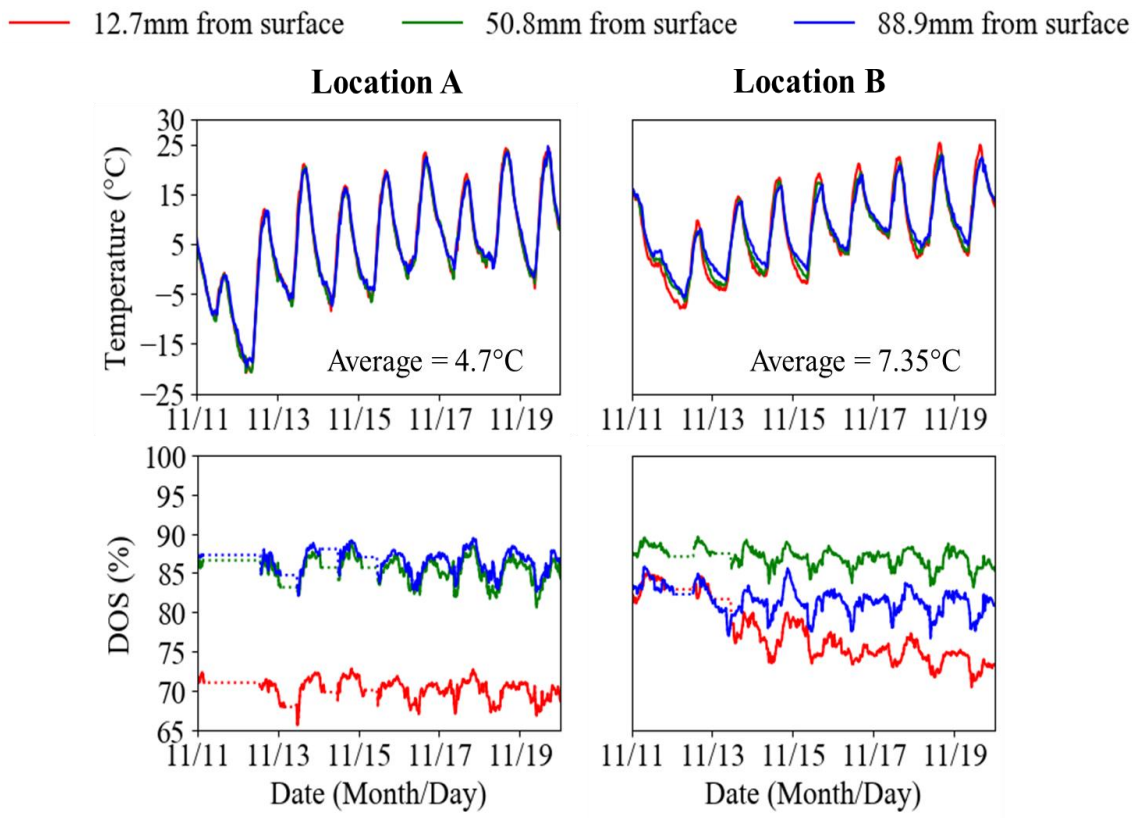

Figure 4-11. Temperature and DOS of the field samples from November 11th to 19th, 2019.

4.3.4 Detection of Freezing Events

Based on the calibration samples, a freezing event is predicted to occur as shown in Equation 4-3 or Figure 4-6 at different combinations of DOS and temperature. To examine how accurate this is, the combination of the temperature and resistivity is used in Equation 4-3 to predict a freezing event and then compared to the measurements made on the field blocks.

Figure 4-12 shows freezing events at 12.7mm depth at location A from November 11th to 19th, 2019. A horizontal line is shown in Figure 4-12(a) at 0°C to highlight the freezing point of water. It should be noted that this is the highest temperature when freezing may occur but it will depend on the DOS of the sample as shown in Equation 4-3. The blue dashed vertical lines show where the ice should start forming based on Equation 4-3 and the green dashed vertical line shows

where the ice should be melted. There are several locations where the temperature of the concrete decreased below 0°C but ice is not expected to form. The reason ice does not form is that at the DOS of the sample the temperature needs to be lower than 0°C for the ice to form. This again shows the complexity of predicting ice formation without simultaneous information about the DOS and the temperature of the samples.

Figure 4-12(b) shows the predicted DOS over time based on the resistivity measurements. It can be noted that sudden changes in the predicted DOS appear during the predicted freezing event. This DOS is not accurate. It is instead a reflection of the change in resistivity caused by the ice formation in the sample. Because of this, the measured DOS during a freezing event is shown as a dashed horizontal line. This can be seen in Figure 4-12(c). This resistivity change of freezing typically causes a sudden 8% or higher resistivity change.

This shows that the predicted freezing from Equation 4-3 closely matches the detected ice formation in the field. This validates the use of calibration samples to predict field performance and it also shows that Equation 4-3 can be used on the data to predict the number of freezing events. This creates a useful approach to determine the number of freezing events at different depths and times for the two locations. This work defines an effective freeze-thaw cycle if the temperature and DOS met the requirements for Equation 4-3 and if there is an 8% or higher change in the resistivity value from ice formation.

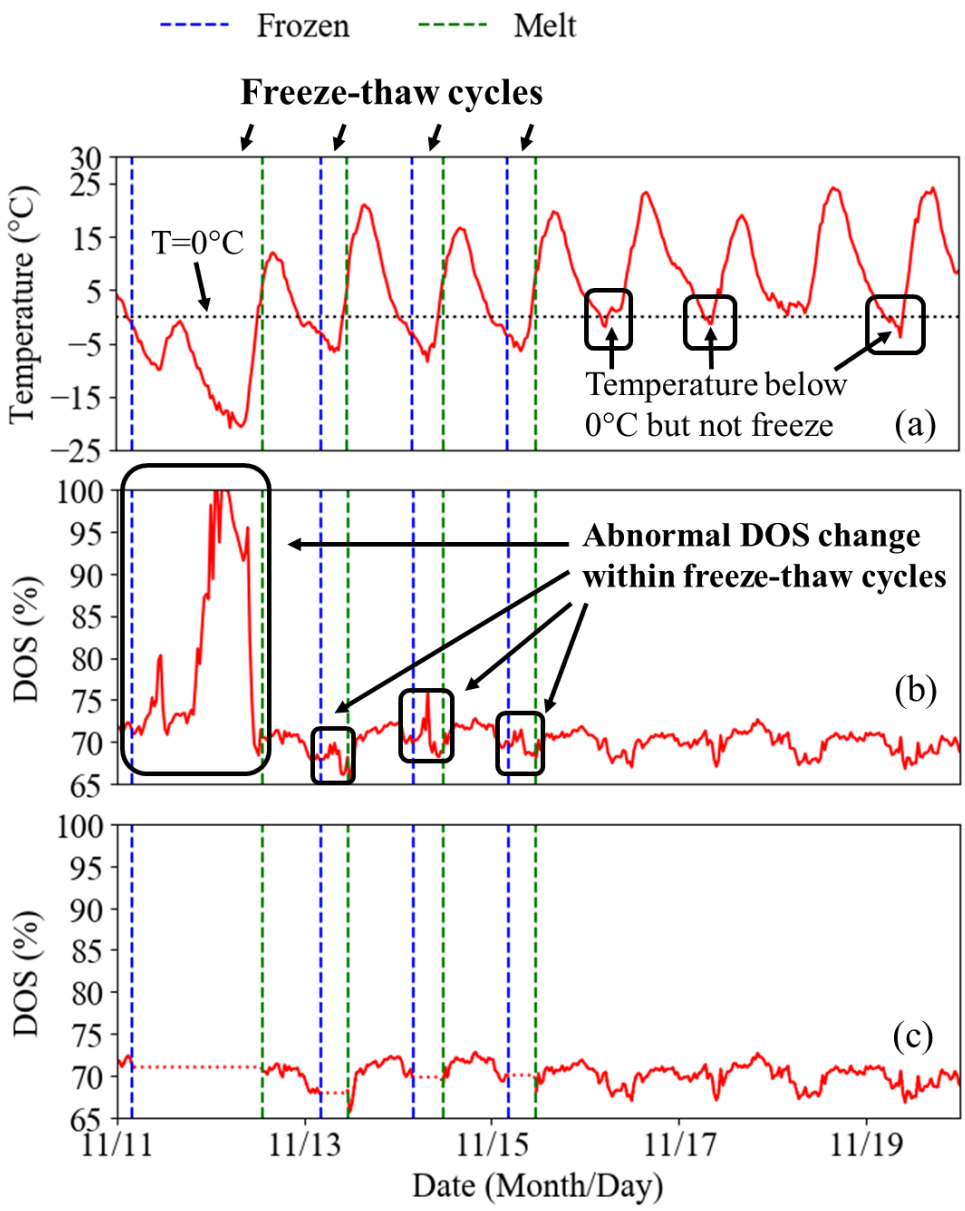

Figure 4-12. Freeze-thaw cycles detection at 12.7mm depth of the field samples in the location from November 11th to 19th, 2019, Oklahoma: (a) temperature curve, (b) DOS curve included the DOS values within freeze-thaw cycles, (c) DOS curve excluded the DOS values within freeze-thaw cycles.

4.3.5 Determining Effective Freezing Events

As stated previously, a freezing event is only expected to be damaging if the moisture level is above the critical DOS. For this work, this is assumed to be 85% or higher. Because the temperature, DOS, and presence of ice are known then all of this can be used to determine if the observed freezing event occurred when the DOS is 85% or higher. This means that the number of effective freezing events can be determined.

For example, Figure 4-13 shows the DOS and determined freezing events for the two locations. This figure shows the freezing events as dashed lines where ice was detected to form. A horizontal line is shown with a DOS of 85%. Any freezing event above this DOS is expected to be an effective freezing event that causes damage and a freezing event below this DOS is not expected to cause damage.

The data shows that the sample in location B has a higher DOS than that in location A. This is also consistent with Table 4-6, as location B has a wetter environment than A. This means that location B tends to be more susceptible to freeze-thaw damage when freezing occurs. It also shows that, in both locations, the DOS is not consistent over the depth of the sample. The middle of the sample tends to have a higher DOS than the surface and so they will lead to more effective freezing events. For example, in location A, the freeze-thaw events below 51mm depth are susceptible to damage as the DOS is higher than 85%; however, the freeze-thaw events at higher depths are not. In both locations, the DOS at 51mm and lower is higher than 85%, which means a freezing event will always cause ice that can cause damage.

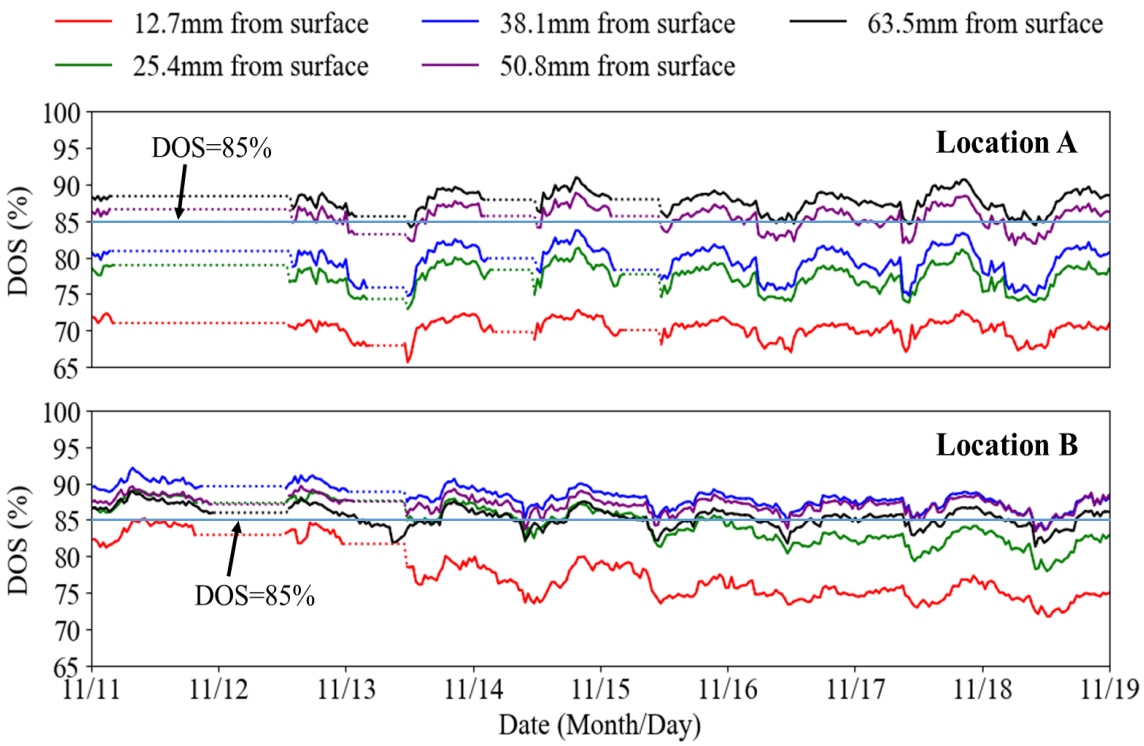

Figure 4-13. Freeze-thaw cycles detection at different depths of the 2 locations from November 11th to 19th, 2019.

3.6 Differences in Performance in the Field

To compare the two locations, a summary of the freeze-thaw cycles and environmental conditions of both locations from 11/2019 to 4/2020 is shown in Table 4-7 and the freeze-thaw cycles that occurred are shown in Figure 4-14. These days are analyzed because this is the time when the temperature is below 0°C.

The freezing events in Table 4-7 are the times when ice was observed to form. The effective freezing events are when ice is formed and the DOS is greater than 85%. Entries are also added for the average air temperature, relative humidity, precipitation, and the number of times the air temperature was below 0°C. This information is included to compare the two sites.

Several useful observations can be made. First, the number of freezing events experienced by the concrete is approximately the same at each depth within the sample. This means that the insulation provided by the overlaying concrete or ground did not reduce the number of observed freeze-thaw cycles for this test setup. This means that if ice formation was observed in one depth then it was observed in all depths at both locations.

Also, there are more effective freezing events below 51mm than near the surface of the samples. In fact, for both samples, there were almost no effective freezing events observed at less than 25 mm from the surface. This occurs because the DOS near the surface was consistently less than 85% when a freezing event occurred and at 51 mm from the surface the DOS seems to be close to 85% at these two locations. More details are shown in Figure 4-14. Figure 4-14 shows a dot for each freezing event and the DOS that was measured when it occurred. Location A had more freezing events and many of them occurred when the depths had a DOS greater than 85%. Location B has fewer freezing events and effective freezing events were consistently observed at 38 mm and 51 mm from the surface. This was consistent for both samples at location B throughout the 6 months observed. These differences likely happen because of differences in wetting and drying between locations A and B. This is an area of future study.

Since certain locations within each sample have a DOS at 85% or above and the freezing events will happen at all depths of the sample, this means that any freezing event has the potential to cause damage at some location within the sample. This can simplify the prediction of the number of effective freezing events. More work will be needed to better understand the DOS profile within the concrete and how it changes over time at different depths.

Another important observation is that the number of times the air temperature goes below 0^{o}C only roughly correlates with the number of freeze-thaw cycles observed. For example, location A has roughly 67% more times the air temperature went below 0^{o}C, but location A experienced

433% more freezing events than location B. This shows that it is important to understand the combination of DOS and temperature when determining the number of freezing events.

Table 4-7. Summary of freeze-thaw cycles (FT) in the two locations from 11/2019 to 4/2020.

Depth from the surface (mm)	Location A				Location B			
	Avg. air T(°C)	Avg. air RH(%)	Avg. precipitation (mm)	Air T<0°C	Avg. air T(°C)	Avg. air RH(%)	Avg. precipitation (mm)	Air T<0°C
	5.9	59.6	0.05	171	8.9	68.0	0.18	102
	Freezing events		Effective freezing events		Freezing events		Effective freezing events	
13	71		0		13		0	
25	77		3		13		3	
38	80		11		15		14	
51	89		75		14		14	
64	84		84		9		2	
76	80		79		8		4	
89	77		74		3		0	

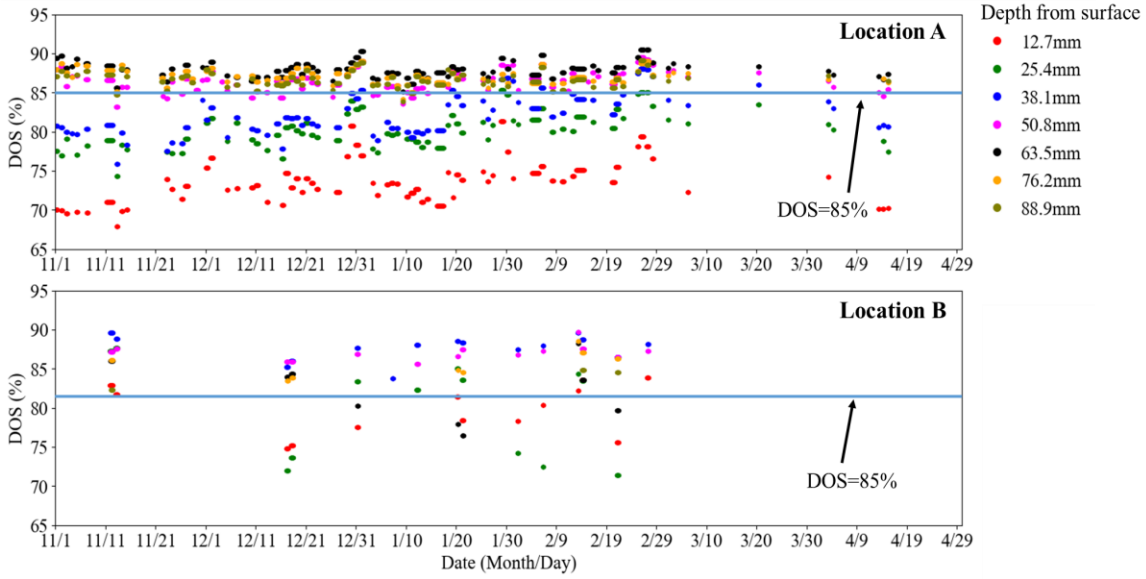

Figure 4-14. Freeze-thaw cycles detection at different depths from 11/2019 to 4/2020.

4.4 Practical Significance

This work provides specific insight into the DOS, temperature, and presence of ice at two locations. This is a starting place to understand how effective freeze-thaw cycles vary in different

geographic conditions. While this work only looked at two locations this same approach is being extended to more than 40 locations throughout the United States with different weather patterns. While the wider number of observations is future work, this work establishes the validity of the method and makes several important findings.

These findings are the first step in developing a measurement-based map or system that can quantify the amount of effective freeze-thaw cycles. Further, this work can establish a procedure to allow local weather conditions to predict the number of effective freeze-thaw cycles in the field through machine learning or some other data-based model.

Care needs to be taken in interpreting this work as the relationship between resistivity, DOS, and ice formation may only apply to these samples and conditions. This also means that the number of effective freeze-thaw cycles determined by this method can be influenced by the mixture, local weather conditions, and specific drainage conditions. Despite these limitations, these results are useful as they use the same material in each location. This means that these measurements are an indicator of the impact of the weather on horizontal concrete surfaces with poor drainage. Since these samples are directly stored on the soil they are most applicable to a pavement, sidewalk, runway, or a slab on grade; however, these findings can likely be extended to bridge decks since the freezing events shown in Table 4-7 are similar at each depth. More observations are needed to validate these findings. This work likely does not apply to vertical concrete except in areas where there is poor drainage.

4.5 Conclusions

In this study, a method has been established to determine the temperature and DOS in mortar samples at varying depths that are surrounded by concrete and placed on soil. This process was calibrated with laboratory studies on a single mixture to establish ice formation and this was validated in the field. These processes can then be used to evaluate the DOS of the mortar when

ice formation occurs. This information can be used to determine the number of damaging or effective freeze-thaw cycles by assuming the critical DOS based on previous studies. The following observations can be drawn from this work:

- The measured temperatures in the mortar samples show a good agreement with local air temperature measurements with the average difference being 1.7° C.
- The DOS at 12.7 mm from the surface was impacted by the wetting and drying of a rain event. The DOS at 25 mm lagged did not change until 20 h after the event and sometimes the DOS at 25 mm did not change after a rain event.
- By using the resistivity and temperature, the ice formation and the melting temperature has been established for a large mortar sample with different DOS with a polynomial regression equation. for the mixture and sample size in this work. These results show that mortars with DOS closer to 100% or greater than 90% will freeze closer to 0^{o} C and that mortars with DOS lower than 75% freeze at -5^{o} C. These laboratory results match field measurements of ice formation made with resistivity and temperature measurements.
- The number of times the air temperature around a sample went below 0^{o}C only roughly correlates with the number of freeze-thaw cycles observed. This highlights the importance of understanding the combination of DOS and temperature when determining the number of freezing events.
- The number of freezing events measured is approximately the same at each depth for two different field locations. This means that the insulation provided by the ground or the depth of the mortar didn't reduce the number of freezing events in the 178 mm thick samples.
- Because the DOS is typically lower at the surface, there were practically zero effective freezing events for the two locations between the surface and 25 mm in depth. For these

two locations, the DOS at 51 mm is always greater than 85% and so each freezing event created an effective freeze-thaw cycle. The moisture gradients are important to understand the number of effective freeze-thaw cycles at different depths.

The work presented in this paper is an early step to establish a procedure to determine the relative number of effective freeze-thaw cycles based on local weather conditions. This method is being extended to a larger number of locations and seasons to bring more insights into effective freezing events in the field.

CHAPTER V

A NOVEL METHOD OF EFFECTIVE FREEZE-THAW CYCLE MONITORING IN THE FIELD

5.1 Introduction

The freeze-thaw durability of concrete is greatly impacted by its surrounding environments [43, 44]. The environmental influence on temperature and degree of saturation (DOS) (the percentage of water that occupies the pore space present in the sample) plays a critical role in this process [45–51]. Previous freeze-thaw studies have shown that the level of damage from freeze-thaw cycles depends on the DOS during freezing and a critical DOS range of 78% to 95% is suggested to be harmful when concrete is freezing [12, 13].

As a result, understanding the DOS change of concrete under freeze-thaw cycles is critical for the design of freeze-thaw durability. However, the lab experiments such as ASTM C666 [14] cannot provide representative situations to the field environments [52–55]. In the previous chapter, a field instrument has been proven to help gather DOS and freeze-thaw cycles in two locations in Oklahoma and the freeze-thaw details in these two locations have been analyzed.

The objective of this work is to gather field data on the DOS and subsequent freeze-thaw cycles inside an insulated mortar specimen. The field measurements use thermocouples to measure temperature and electrical resistivity to measure the moisture and ice formation. These

measurements will be taken at different depths and this can be used to determine the number of freezing events and quantify the ice formation of the samples in the field. The purpose of this chapter is to prove that the same method of determining DOS and freeze-thaw cycles are also applicable for other locations where the instrument is installed and the details of the freeze-thaw cycle were analyzed and summarized. A method of using weather station temperature is proposed to predict the concrete freeze-thaw cycles and the result is compared with the field measurements.

5.2 Experimental Methods

5.2.1 Field Sample Preparation

The field samples were made from a mortar mixture and cast into 152.4 mm in diameter by 228.6 mm tall plastic cylinders. The mixture proportion by volume is shown in Table 5-1. The water-to-cement ratio (w/c) was 0.45. The cement used for the mortar mixture met the requirements of an ASTM C150 Type I Portland cement. The chemical compositions of the cement are shown in Table 5-2. The fine aggregate used was local natural sand and met the requirements of ASTM C33. No supplementary cementing materials (SCM) were used in the samples to minimize the change in resistivity over time [72].

Table 5-1. Mixture proportion of mortar.

	Cement	Water	Fine Aggregate	Air
Volume (%)	18.5	23.4	52.7	4.4

Table 5-2. Chemical composition of cement.

	SiO_2	Al_2O_3	Fe_2O_3	CaO	MgO	SO_3	Na_2O	K_2O	C_3S	C_2S	C_3A	C_4AF	LOI
Cement (%)	21.1	4.8	3.1	64.5	2.33	3.2	0.17	0.58	50	23	7	9	2.6

The configuration of the mortar samples is shown in Figure 5-1. Four type T thermocouples and eight pairs of 4-40 threaded stainless steel rods (2.8 mm in diameter, and 40 threads per 25.4 mm) were held in place by drilling holes in the empty mold along with the depth and holding the thermocouples and rods in place with glue. The steel rods had a diameter of 4.6 mm and a center-

to-center distance of 92.7 mm at each depth. The top steel rods and thermocouples were installed above the mortar surface and exposed to the air to detect water accumulation and air temperature respectively. The surface of the mortar samples was 25.4 mm lower than the mold top to promote water accumulation. This space forces any water that falls to be retained and evaporate naturally to mimic a structure with poor drainage.

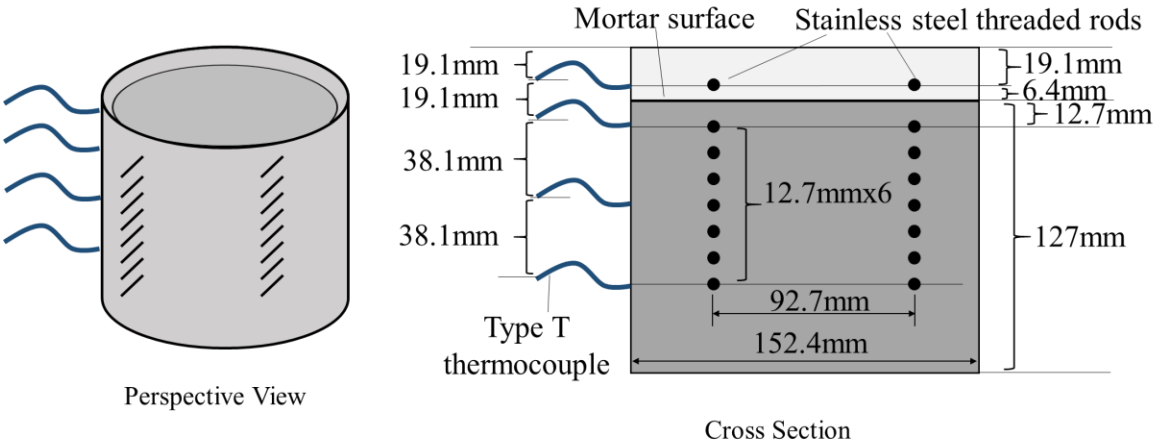

Figure 5-1. Configuration of the thermocouples and steel rods of the mortar sample.

The mortar samples were wet cured for 2 months by adding water to their top and covering the top with a plastic tarp. This was done to keep the samples at a high DOS before they are sent out to the field. After the samples were over 28 days old, copper wires of 16 AWG were soldered on each steel rod. The copper wires extended the distance between the mortar sample and the data logger. Electrical tape was used to cover the copper wires after they were soldered on the steel rods to isolate the circuit from the outside concrete cover.

As the mortar sample dries then it will shrink [73]. To avoid a gap created by shrinkage between the sample and the plastic mold, a low shrinkage mortar is used to seal the edge of the sample along with the plastic mold. The low shrinkage mortar was the same mixture from Table 5-1 but it used a 9% replacement of the water with a shrinkage reducing admixture.

The equipment used to monitor the performance of the mortar samples is shown in Figure 5-2. The mortar specimens were connected to the instrument box through thermocouples and extended copper wires for temperature and resistivity measurements respectively. A data logger was installed inside the instrument box and powered by a 12 voltage battery charged through the solar panel. The instrument box was fixed 0.9 m above the ground.

Each block contained two mortar samples so that redundant measurements can be made. The fiber-reinforced concrete cover protected the wiring and samples, it also ensured the samples stayed upright and it insulated the samples to simulate a sample within a concrete pavement. The surrounding concrete used 0.45 w/cm concrete mixtures with macro synthetic fibers at 2% by volume of the mixture. The size of the final concrete block is 457 mm × 305 mm × 178 mm.

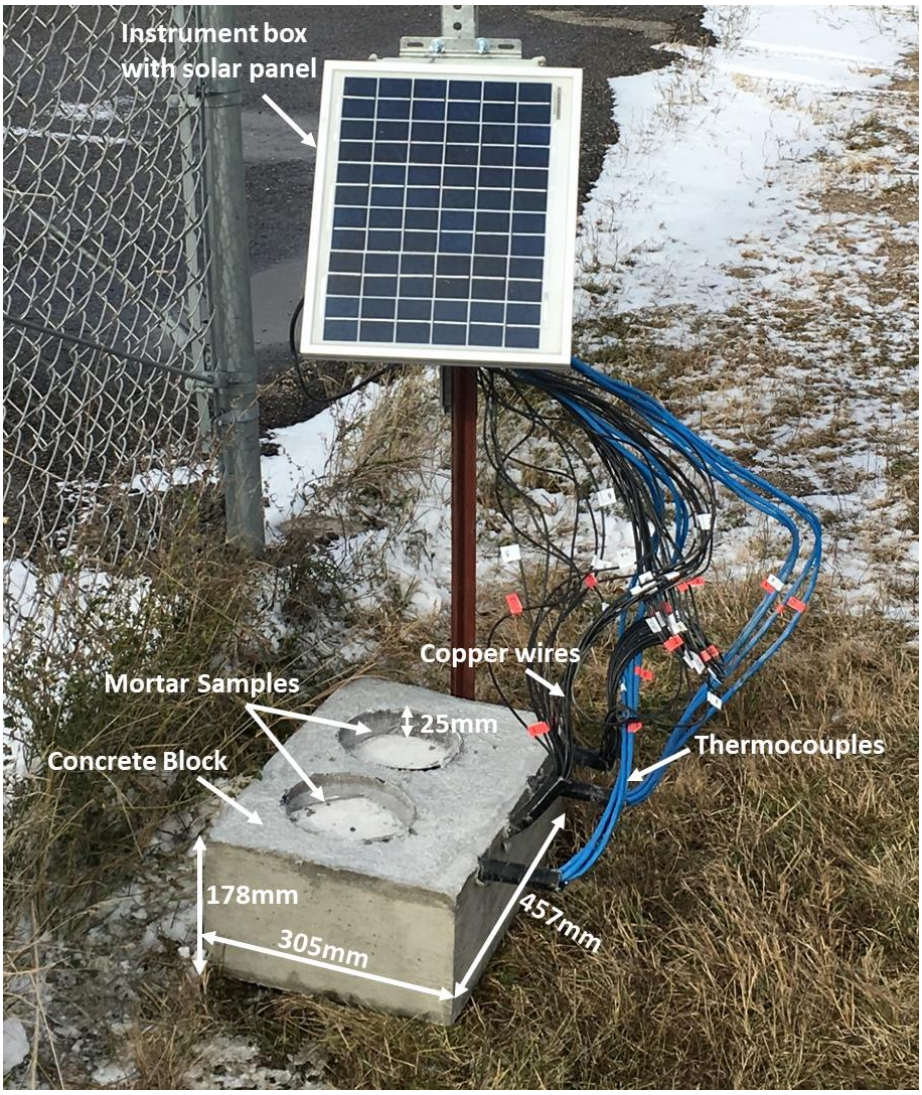

Figure 5-2. Configuration of the instrumentation box.

The data logger is a printed circuit board (PCB) developed for resistivity and temperature monitoring. The PCB was designed with KiCAD and programmed with the Arduino platform. An ATmega 2560 was used as the central processing unit. The circuit used a clock to record the time of each measurement. The resistivity and temperature are measured every 30 minutes and the data is recorded on an SD card. The data was then retrieved into a USB drive for later analysis. Several multiplexers were embedded into the PCB to expand the measurement ability to 16 channels.

A 12-Bit impedance converter AD5933 was the sensor used to measure resistivity. The frequency generator of the AD5933 allows the mortar specimen to be excited at a frequency of 4KHz, at which the imaginary impedance is close to 0, and the real impedance is used as the bulk resistance of the mortar specimen in ohms. To get the resistivity of the mortar sample, Equation 5-1 was used.

$$Resistivity\ (K\Omega * cm) = bulk\ resistance\ (\Omega) * A\ (mm2)\ /\ L\ (mm)/10000 \quad \text{Equation 5-1}$$

In Equation 5-1, A is assumed to be the rectangular cross-sectional area of the electrode perpendicular to the signal. Since the electrode is 2.8 mm in diameter and approximately 121 mm long, the area is taken as 338.8 mm^2. The distance between the electrodes, L, is 92.7 mm. More details on how the impedance and temperature sensors work in the data logger could be found in Appendix F.

5.2.2 Calibration Sample Conditioning

The calibration samples were made with the same mortar mixture as the field samples and cured in the same way but did not contain thermocouples. These samples were first conditioned at a fixed relative humidity and stored in an environmental chamber according to ASTM E-104 [74]. After the samples reached a constant mass, a 40g sample was removed and tested for DOS according to ASTM C642. To get a wider array of DOS, some samples were vacuum saturated and then dried to meet a target DOS. This was done to avoid drying samples in an oven that may cause microcracking. This process was completed to obtain a DOS of 36.2%, 45.6%, 65%, 75%, 86.8%, 90%, 95%, and 100%. A summary of the different humidity and DOS are shown in Table 5-3.

Table 5-3. DOS of the calibration samples.

Humidity (%)	DOS (%)	The standard deviation of DOS (%)	Freezing temperature (°C)	Thawing temperature(°C)
59	36.2	0.21	-4.8	0.0
75	45.6	0.10	-4.9	0.0
85	65.0	0.16	-4.2	0.0
-	75.0	0.07	-4.6	0.0
100	86.8	0.11	-2.8	0.0
-	90.0	0.03	-2.6	0.0
-	95.0	0.11	-2.5	0.0
-	100.0	-	0.0	0.0

The temperature of the sealed calibration samples was changed from 49°C to -18°C at an interval of 2°C. Each temperature was maintained for 6 hours to ensure the samples reach a uniform temperature. After reaching a uniform temperature, the resistivity of each sample was measured. The relationship between resistivity, temperature, and DOS is in Appendix G.

5.2.3 Field Samples Installation

The field samples were installed at 42 locations in 14 different states across the US to understand the field freeze-thaw response in the field. In this work, the freeze-thaw cycles of 6 locations are studied from November 2020 to April 2021. The details about the 6 field locations are listed in Table 5-4 and their geological position is shown in Figure 5-3. These 6 locations are studied because they have full measurements through the winter from 11/2020 to 4/2021, which allows the details of freeze-thaw cycles to be examined for a common time frame. The temperature, relative humidity, and precipitation of the locations are the average for the year 2020 and are obtained from the Local Climatological Data (LCD) of the National Centers for Environmental Information [80].

Table 5-4. Information on the field locations.

State	Location	Latitude (°N)	Longitude (°W)	Distance from the closest weather station (km)	Annual Avg. temperature (°C)	Annual Avg. RH (%)	Annual Avg. precipitation (mm/month)	Annual Avg. Wind Speed (m/s)
OK	1	36.7	-101.5	21.0	13.5	59.7	76.7	5.2
NY	2	41.0	-72.3	20.0	11.5	76.4	150.7	3.1
NE	3	40.8	-96.8	11.2	10.9	68.5	118.5	4.5
NE	4	42.0	-100.6	3.7	10.4	65.6	44.6	4.2
KS	5	38.9	-101.0	35.0	12.1	59.1	145.2	3.5
KS	6	38.9	-95.7	20	12.9	73.8	210.8	4.0

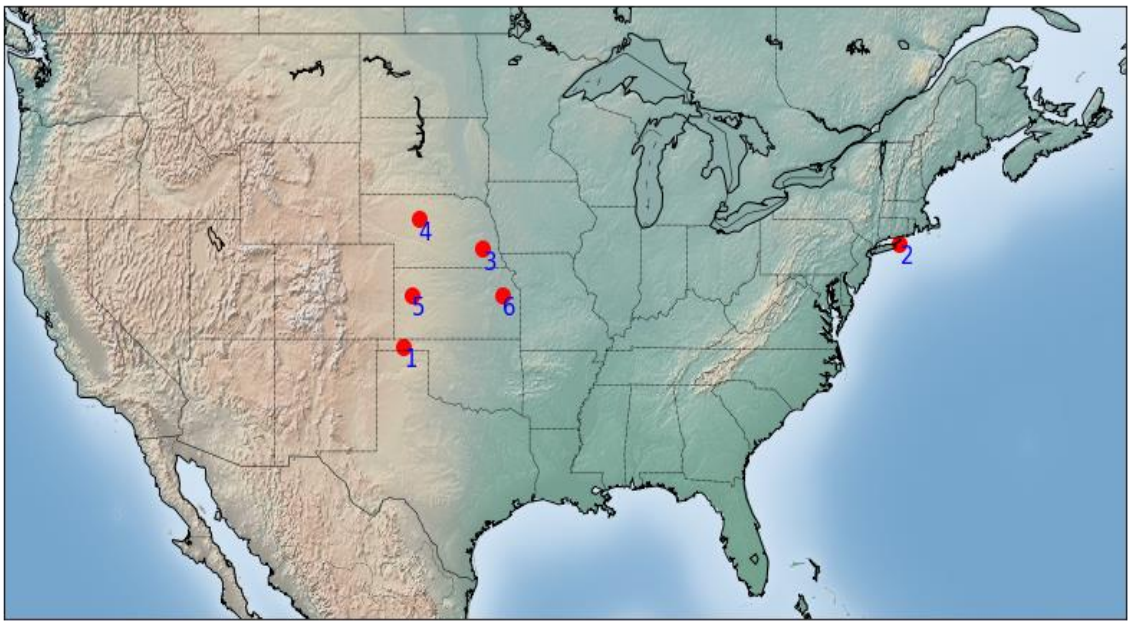

Figure 5-3. Geological positions of different field locations.

5.2.4 Determine Freezing Events using DOS

In the previous chapter, the freeze-thaw cycles in the field are determined by using the DOS to calculate the freezing temperature based on Equation 5-2, as well as a simultaneous 8% or higher resistivity change. The parameter of Equation 5-2is shown in Table 5-5. This method has been proven to be useful when examining the field data in Oklahoma. In this section, the field data

from other locations in different states are examined and the usability of the method from the previous chapter is examined as well.

$$Freezing\ Temperature = a_0+a_1*DOS+a_2*DOS^2+a_3*DOS^3+a_4*DOS^4+a_5*DOS*^5 \quad \text{Equation 5-2}$$

Table 5-5. Parameters value in Equation 5-2.

Parameters	a_0	a_1	a_2	a_3	a_4	a_5
value	3.81e-08	1.2e-05	1.4e-03	-8.1e-02	2.3e+00	-2.9e+01

5.3 Results And Discussion

5.3.1 Wetting and Drying of the Field Samples

Using the laboratory calibration samples, the resistivity and temperature measurements can be used to determine the DOS of the field samples. This method has been applied to the field data from Oklahoma in the previous chapter. In this section, the same method is utilized on the field data from the six locations in Table 5-4. The DOS within the sample can indicate the interaction between field samples and the precipitation in the local weather.

Figure 5-4 shows the DOS change from May 2020 to October 2020 in the six locations in Table 5-4. Depths 13mm and 51mm from the surface were shown for each location, and an example of DOS increase from precipitation is highlighted with arrows. The 13mm depth is the closest to the surface in the concrete sample, this means that this sensor is expected to be the first to show any influence from the weather. The 51mm depth is at the center of the concrete sample, and it is the depth that based on the previous chapter has the most effective freeze-thaw cycles because the DOS content is typically the highest.

In all the locations, the DOS at 13mm from the surface was the most sensitive to precipitation because it is the closest to the surface. This is consistent with the observations in the previous

chapter. For example, in location 1 in Oklahoma, the DOS at 13mm depth increased from 65% to 80% after the rain on May 25th and slowly decreased with time as it dried. Similarly, in location 4 in Nebraska, after the rain on September 10th, the DOS at 13mm depth increased from 83% to 90% and slowly decreased as it dried. In location 2 in New York, the DOS decreased with time but stayed constant with precipitation. For example, the rainfall on October 15th caused the DOS to jump and increased the DOS at the 13mm and 51mm depth, and then the DOS decreased over the next 15 days.

In all the locations the DOS at 51 mm in depth did not change as much as the 13mm depth. However, some precipitation events can still cause an increase in the DOS at 51mm depth. For example, in location 6 in Kansa on May 31st, after precipitation, the DOS at 13mm increased from 80% to 95%. Since moisture was present on the surface and will penetrate the concrete, it can be observed that the DOS at 51mm increased from 95% to 98%.

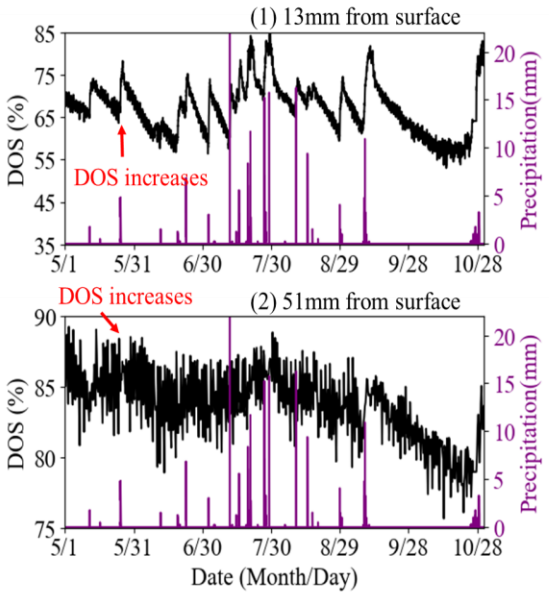

(a) #1 in Oklahoma

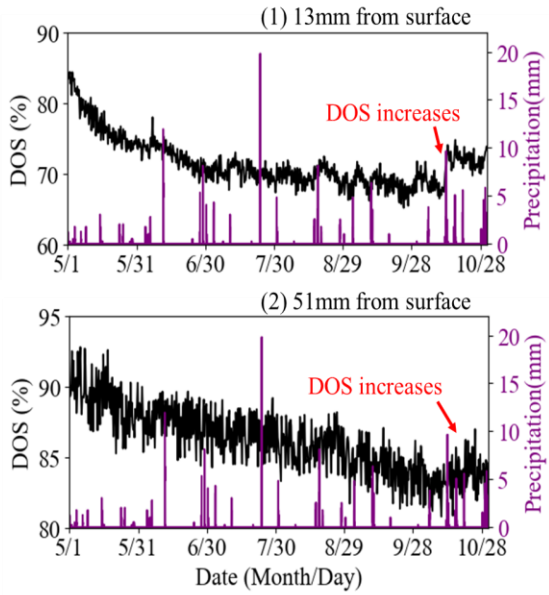

(b) #2 in New York

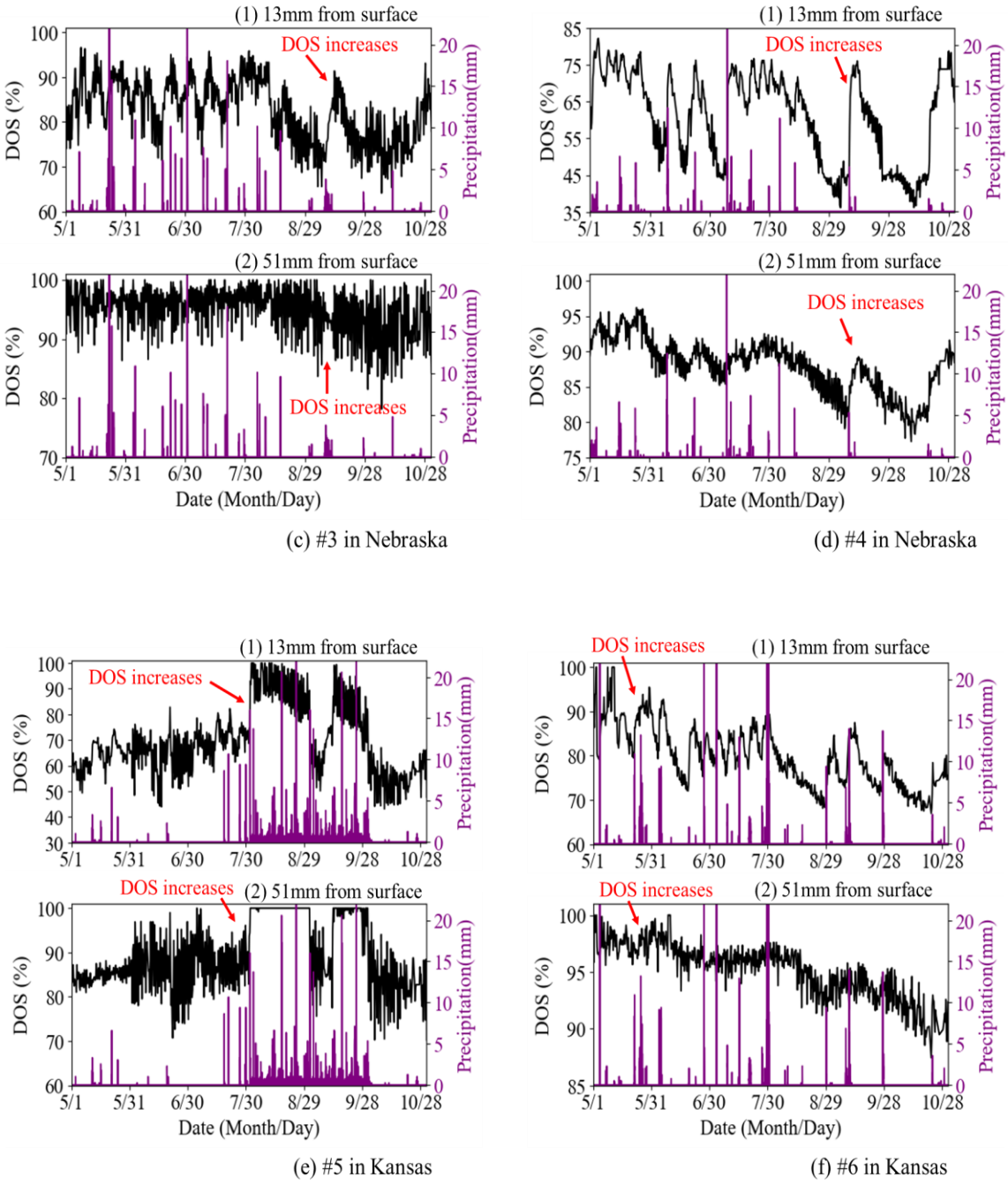

Figure 5-4. Wetting and drying at 13mm and 51mm depth from sample surface in the locations from May 2020 to August 2020: (a) #1 in Oklahoma, (b) #2 in New York, (c) #3 in Nebraska, (d) #4 in Nebraska, (e) #5 in Kansas, (f) #6 in Kansas.

5.3.2 Determining Freezing Events in Different Field Locations

The field temperature, DOS, and, resistivity at 13mm depth from the sample surface when freeze-thaw happened in locations 1 and 2 are shown in Figure 5-5. The data from January 2021 to February 2021 is used because freezing occurred at all six locations. A horizontal line is shown at 0°C in the temperature graph to specify the freezing point of water. This is the highest temperature when freezing may occur but it will depend on the DOS of the concrete as outlined in Equation 5-2 and Table 5-5. The blue dashed vertical lines show where the ice should start forming and the green dashed vertical line shows where the ice should be fully melted. The same graphs for locations 3, 4, 5, and 6 are added in Appendix I.

In all the six locations, there are times when the concrete temperature decreased below 0°C but ice is not expected to form because the DOS is too low. This is also observed in the locations in Oklahoma in the last chapter. This also emphasizes that DOS is important when determining freeze-thaw cycles of concrete.

The DOS curve in Figure 5-5 is obtained based on the resistivity measurements. It can be noted that sudden changes in the predicted DOS appear within the freeze-thaw cycles in all the six locations. This observation is consistent with the field sample in Oklahoma in the previous chapter. This DOS is not accurate. It is instead a reflection of the change in resistivity caused by the ice formation in the sample. This can be observed from the resistivity curve in the figures. Each freeze-thaw cycle generates a resistivity jump at the same time when freezing is predicted to happen. Since the calculated DOS in the freeze-thaw cycle is not real, the DOS in freeze-thaw cycles is assumed to be the same as the DOS right before freezing happens.

This shows that the predicted freezing from Equation 5-2 closely matches the detected ice formation not only in Oklahoma but also in the fields with different geological conditions. This validates the use of calibration samples to predict field performance and it also shows that

Equation 5-2 can be used on the data to predict the number of freezing events for all the locations where the field instruments are measuring.

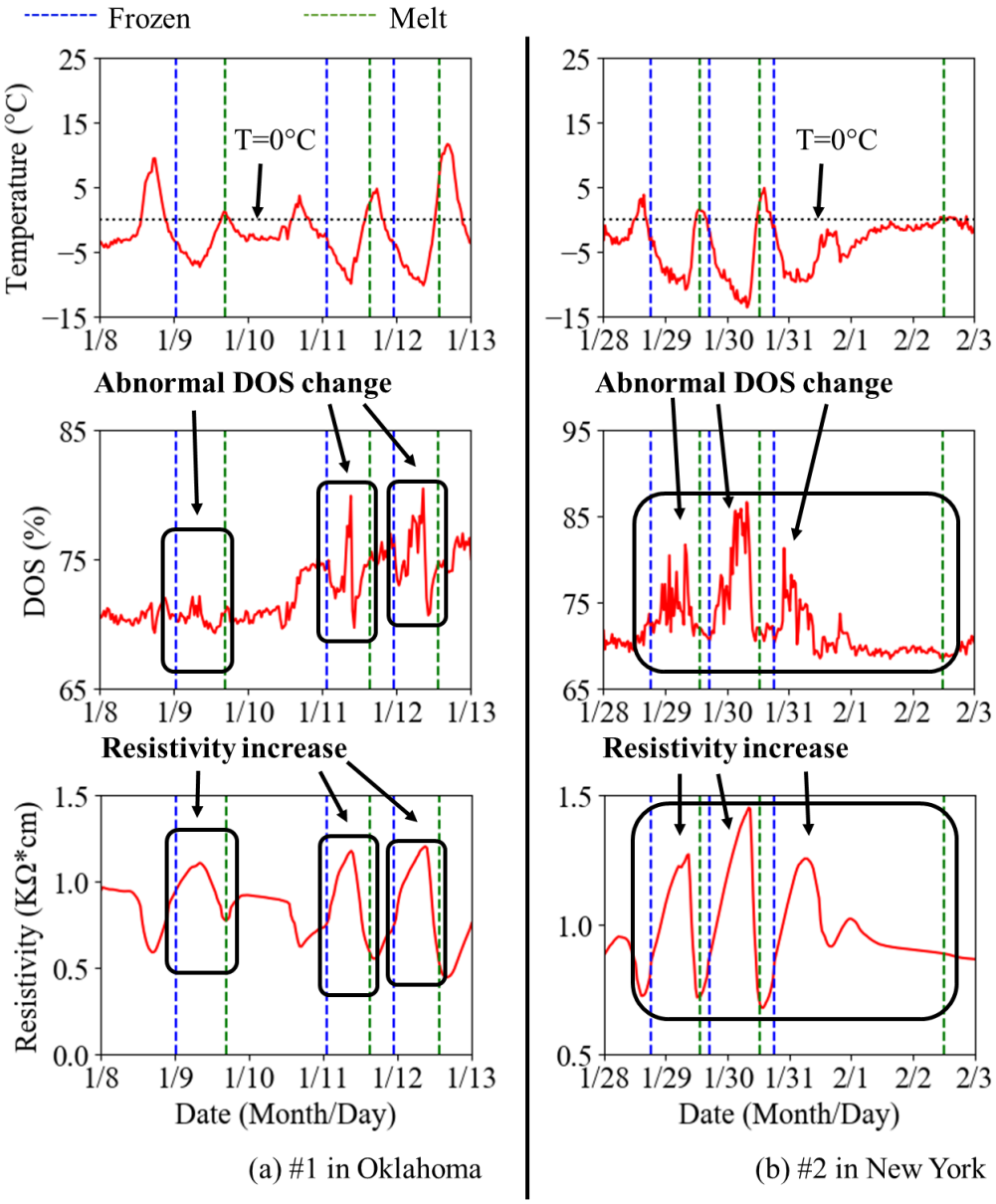

Figure 5-5. Temperature, DOS, and resistivity curve within the freeze-thaw cycles detection at 13mm depth of the field samples in locations #1 and #2 in Table 5-4.

5.3.3 Freeze-thaw Cycles in the Field

To compare the field locations, a summary of the freeze-thaw cycles and environmental conditions from 11/2020 to 4/2021 is shown in Table 5-6 to Table 5-11 for each location and the freeze-thaw cycles that occurred are shown in figures from Figure 5-6 to Figure 5-11 for each location as well. The precipitation during the same time is also shown in Figure 5-6 to Figure 5-11 for each location. These days are analyzed because this is the time when the temperature is below 0°C. The freezing events in Table 5-6 to Table 5-11 are the times when ice was observed to form from the increase in resistivity. The effective freezing events are calculated for three different critical DOS of 80%, 85%, and 90%. These different DOS represent concrete with different quality air void systems. Entries are also added to Table 5-11 for the average air temperature, average air relative humidity, and precipitation from the Local Climatological Data (LCD) for the period from 11/2020 to 4/2021 [80], and the number of times the air temperature was below 0°C. All of these metrics can be used to compare the different locations.

Table 5-6. Freezing summary of #1 in Oklahoma from 11/2020 to 4/2021.

Depth from the surface (mm)	Avg. air T(°C)	Avg. air RH(%)	Total Precip. (mm)	Avg. Wind Speed (m/s)	Air T < 0°C
	4.7	60.9	276.9	5.3	148
	Freezing events	Freezing events with DOS > 80%	Freezing events with DOS > 85%	Freezing events with DOS > 90%	
13	50	2	0	0	
25	41	2	0	0	
38	45	5	0	0	
51	50	50	2	0	
64	50	50	26	0	
76	42	42	4	0	
89	42	42	2	0	

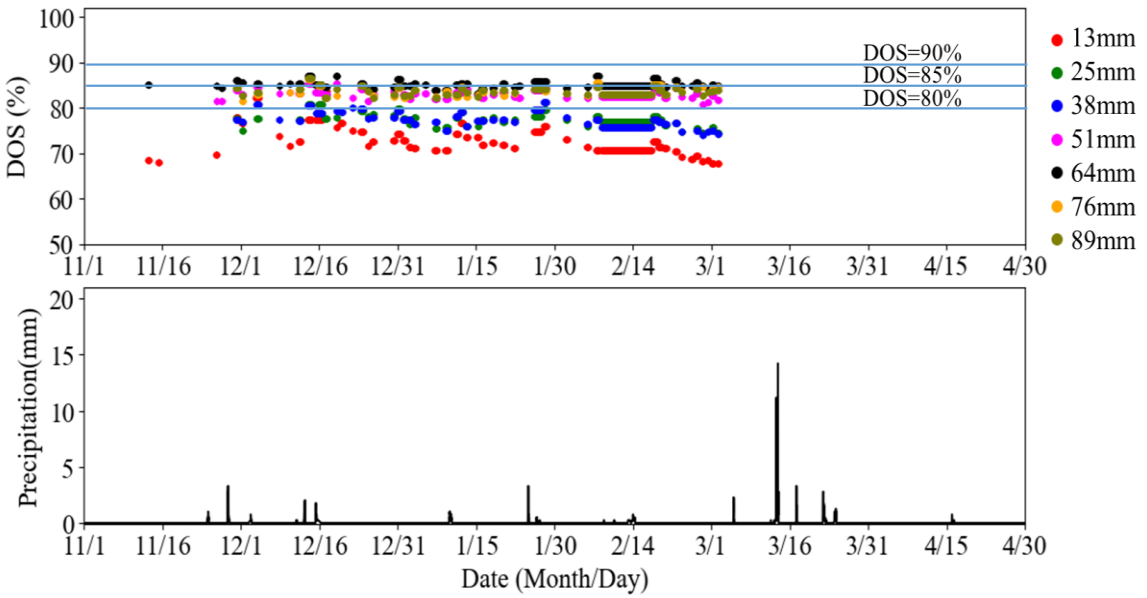

Figure 5-6. Freeze-thaw cycles detection of #1 in Oklahoma at different depths from 11/2020 to 4/2021.

Table 5-7. Freezing summary of #2 in New York from 11/2020 to 4/2021.

Depth from the surface (mm)	Avg. air T(°C)	Avg. air RH(%)	Total Precip. (mm)	Avg. Wind Speed (m/s)	Air T < 0°C
	4.2	71.7	1001.5	3.4	166
	Freezing events	Freezing events with DOS > 80%	Freezing events with DOS > 85%	Freezing events with DOS > 90%	
13	47	0	0	0	
25	49	6	0	0	
38	56	54	0	0	
51	69	69	11	0	
64	55	55	10	0	
76	55	55	6	0	
89	54	54	0	0	

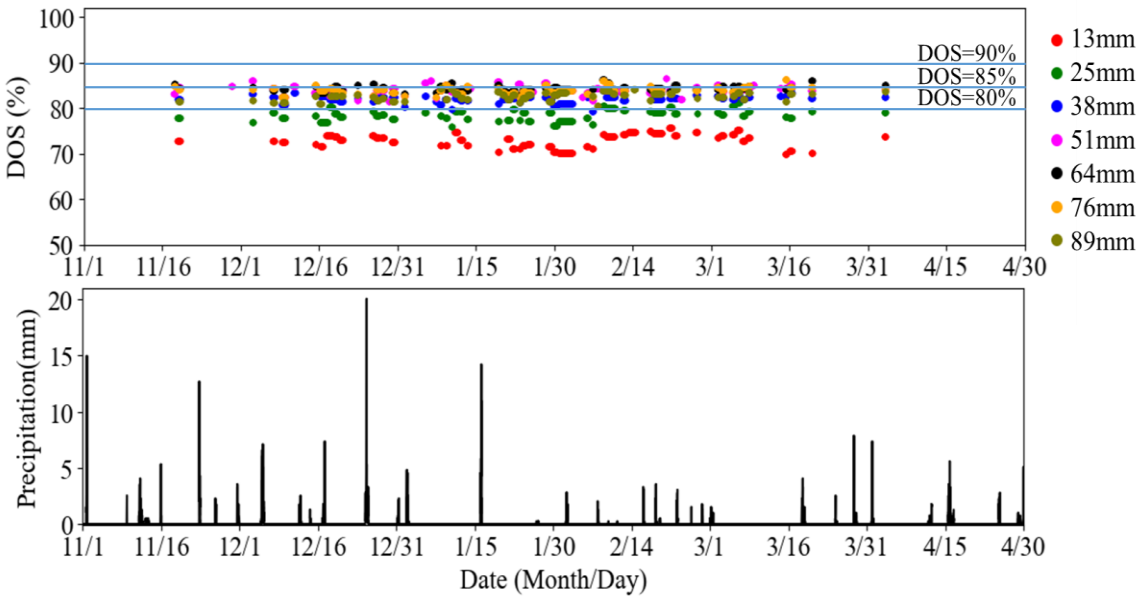

Figure 5-7. Freeze-thaw cycles detection of #2 in New York at different depths from 11/2020 to 4/2021

Table 5-8. Freezing summary of #3 in Nebraska from 11/2020 to 4/2021.

Depth from the surface (mm)	Avg. air T(°C)	Avg. air RH(%)	Total Precip. (mm)	Avg. Wind Speed (m/s)	Air T < 0°C
	1.8	68.8	550.9	4.4	227
	Freezing events	Freezing events with DOS > 80%	Freezing events with DOS > 85%	Freezing events with DOS > 90%	
13	80	69	46	13	
25	72	70	68	41	
38	79	79	79	55	
51	108	108	108	103	
64	95	95	95	86	
76	64	59	58	36	
89	63	62	51	19	

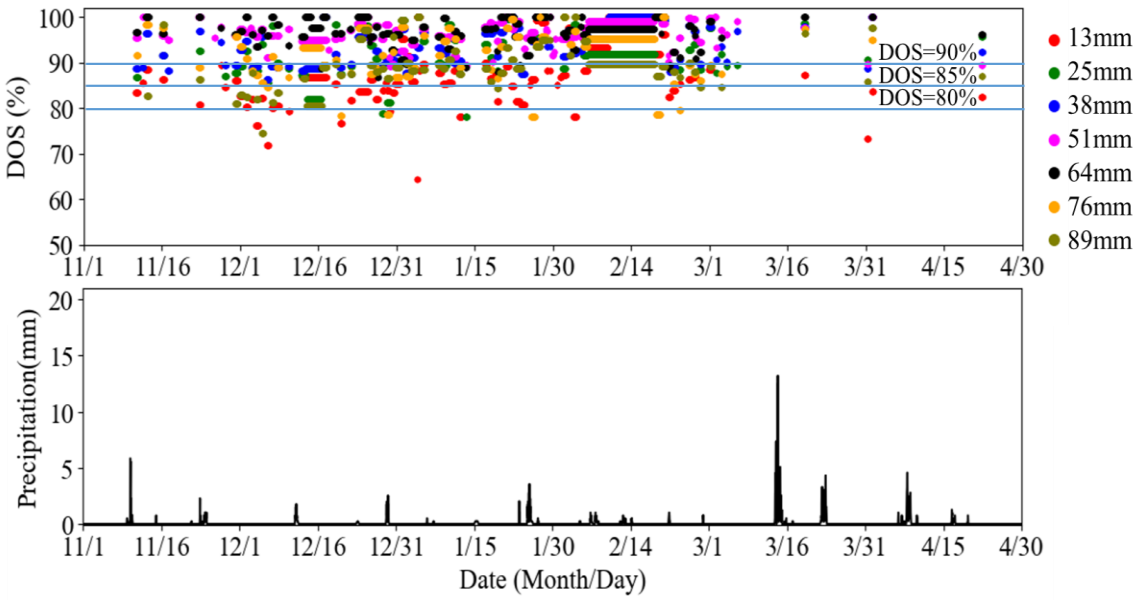

Figure 5-8. Freeze-thaw cycles detection of #3 in Nebraska at different depths from 11/2020 to 4/2021.

Table 5-9. Freezing summary of #4 in Nebraska from 11/2020 to 4/2021.

Depth from the surface (mm)	Avg. air T(°C)	Avg. air RH(%)	Total Precip. (mm)	Avg. Wind Speed (m/s)	Air T < 0°C
	2.0	65.6	104.4	4.0	152
	Freezing events	Freezing events with DOS > 80%	Freezing events with DOS > 85%	Freezing events with DOS > 90%	
13	46	0	0	0	
25	57	57	25	0	
38	49	49	37	1	
51	58	58	57	2	
64	47	47	47	9	
76	40	40	38	0	
89	26	1	1	0	

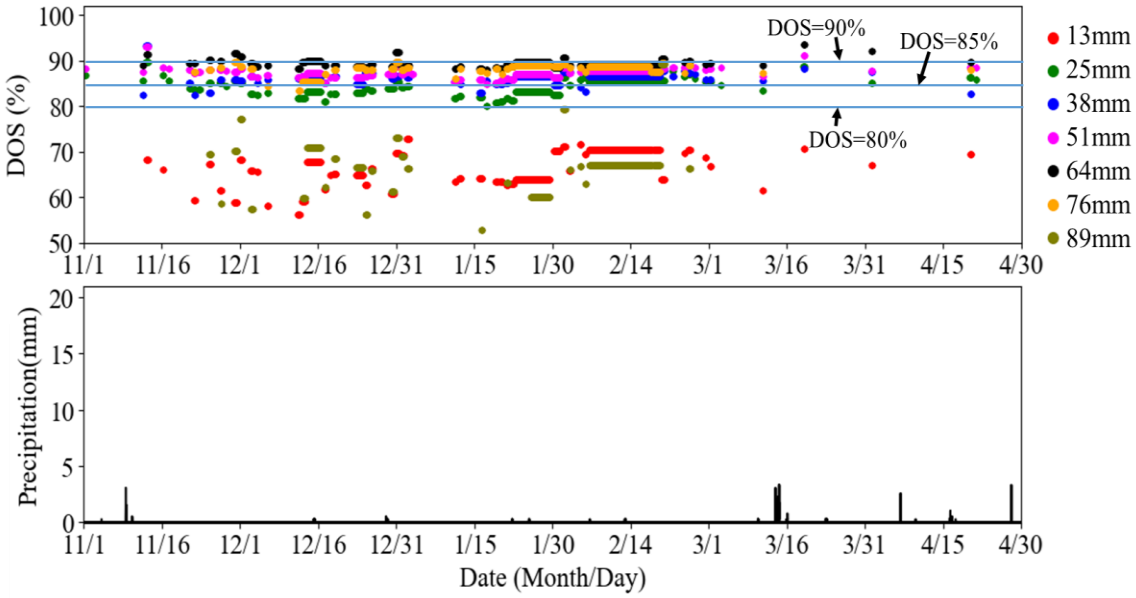

Figure 5-9. Freeze-thaw cycles detection of #4 in Nebraska at different depths from 11/2020 to 4/2021.

Table 5-10. Freezing summary of #5 in Kansas from 11/2020 to 4/2021.

Depth from the surface (mm)	Avg. air T(°C)	Avg. air RH(%)	Total Precip. (mm)	Avg. Wind Speed (m/s)	Air T < 0°C
	3.1	58.1	121.7	3.6	131
	Freezing events	Freezing events with DOS > 80%	Freezing events with DOS > 85%	Freezing events with DOS > 90%	
13	31	3	1	1	
25	30	14	10	1	
38	35	31	21	9	
51	40	39	30	15	
64	36	35	30	16	
76	33	33	29	17	
89	21	16	14	7	

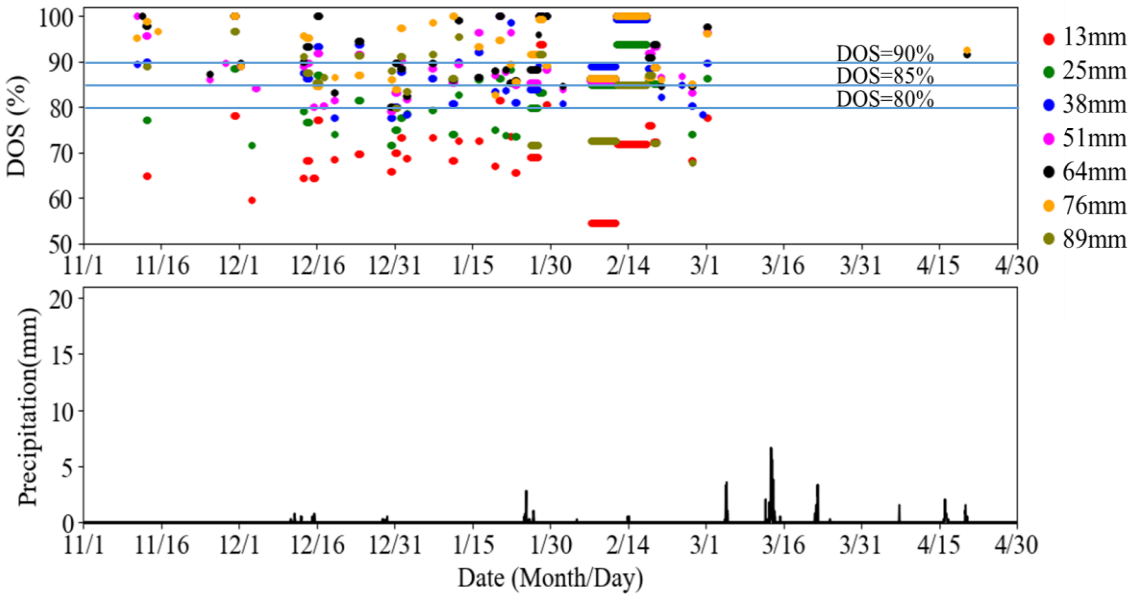

Figure 5-10. Freeze-thaw cycles detection of #5 in Kansas at different depths from 11/2020 to 4/2021.

Table 5-11. Freezing summary of #6 in Kansas from 11/2020 to 4/2021.

Depth from the surface (mm)	Avg. air T(°C)	Avg. air RH(%)	Total Precip. (mm)	Avg. Wind Speed (m/s)	Air T < 0°C
	4.5	73.3	545.6	4.6	129
	Freezing events	Freezing events with DOS > 80%	Freezing events with DOS > 85%	Freezing events with DOS > 90%	
13	54	42	19	0	
25	53	53	47	17	
38	51	51	51	30	
51	60	60	60	59	
64	69	65	60	58	
76	61	61	60	55	
89	63	63	57	57	

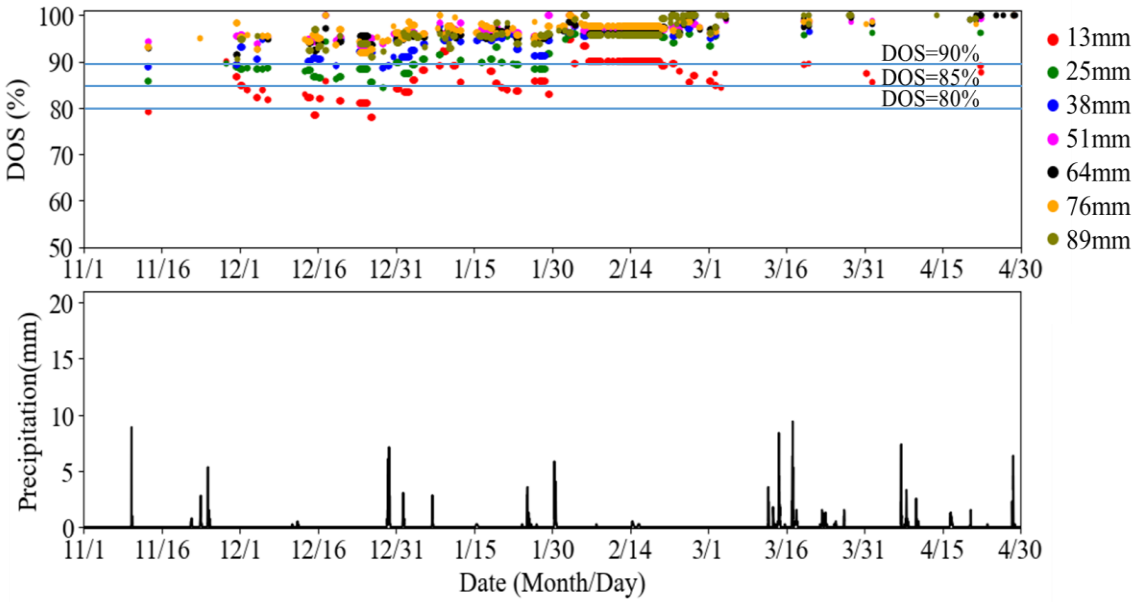

Figure 5-11. Freeze-thaw cycles detection of #6 in Kansas at different depths from 11/2020 to 4/2021.

Figure 5-12 shows the maximum effective freeze-thaw cycles for each sample measured when the DOS is greater than 85%. This occurs at 51mm from the surface for locations 1 to 5 and 89mm for location 6.

In Figure 5-12, locations 3 and 4 are both from Nebraska. However, location 3 has almost twice the effective freeze-thaw cycles of location 4. Their relative humidity (68.8% in location 3 and 65.6% in location 4) and average air temperature (1.8°C in location 3 and 2.0°C in location 4) are close. But the total amount of precipitation in location 3 is over 5 times of location 4 (550.9mm in location 3 and 104.4mm in location 4) and so the higher amount of precipitation is important in determining the number of critical freeze-thaw cycles.

Similarly, locations 5 and 6 are both in Kansas, but the effective freeze-thaw cycles in location 6 are 50% more than in location 5. The average temperature in location 6 is 50% higher than location 5 (3.1°C in location 5 and 4.5°C in location 6) and its relative humidity is 30% higher

than location 5 (58.1% in location 5 and 73.3% in location 6). Furthermore, the total precipitation in location 6 is over 4 times of location 5 (121.7mm in location 5 and 545.6mm in location 6). As a result, location 6 has more effective freeze-thaw cycles. The comparison between locations 3 and 4, locations 5 and 6 indicates that the east side of Nebraska and Kansas is much more susceptible to freeze-thaw damage because of a higher amount of precipitation.

Locations 4 and 5 are both on the western side of their state and have similar longitudes but different latitudes. The number of effective freeze-thaw cycles is 50% less in location 5. The total precipitation (104.4mm in location 4 and 121.7mm in location 5) and relative humidity (65.6% for location 4 and 58.1% in location 5) are similar, but the average temperature at location 5 is 50% greater than location 4 (2°C for location 4 and 3.1°C for location 5). This might be the reason that location 5 has less effective freeze-thaw cycles than location 4.

Similarly, location 1 has 13% less effective freeze-thaw cycles than location 5. The total precipitation in location 1 is higher than in location 5 (276.9mm in location 1 and 121.7mm in location 5) and the relative humidity is also higher in location 1 (60.9% in location 1 and 58.1% in location 5). But the average temperature is 35% lower in location 5 (4.7°C in location 1 and 3.1°C in location 5), which might be the reason that location 5 has more effective freeze-thaw cycles than location 1. The same comparison can also be found in locations 6 and 3. Location 3 has 80% more effective freeze-thaw cycles than location 6. Their relative humidity (68.8% in location 3 and 73.3% in location 6) and the total precipitation (550.9mm in location 3 and 545.6mm in location 6) are similar, but the temperature in location 3 is 60% lower in location 3 (1.8°C in location 3 and 4.5°C in location 6).

Location 2 has the least freeze-thaw cycles overall. This is because it has the lowest DOS of the locations investigated. This can be observed in Figure 5-7. Besides, Figure 5-4 (b) also shows that the DOS of the concrete in location 2 is decreasing over time even though precipitation is

occurring. However, more details are needed to explain why location 2 has the lowest DOS because its total precipitation is the highest (1001.5mm) and its relative humidity is the second highest (71.7%). The average temperature is the second-highest in location 2 (4.2°C). But none of the above entries explains why the DOS is low for this location.

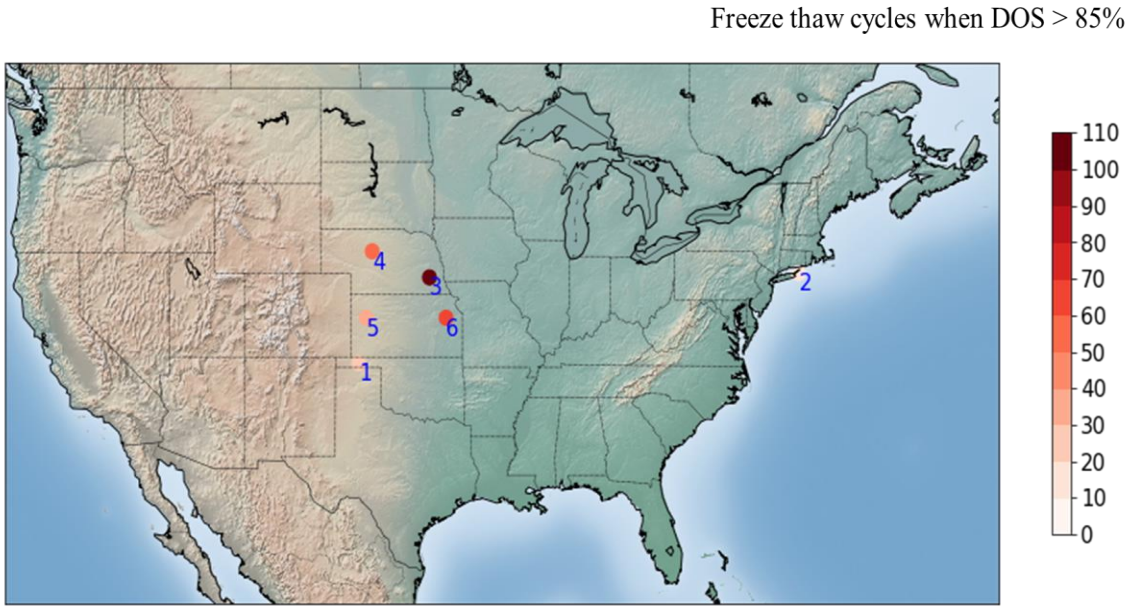

Figure 5-12. Freeze-thaw cycles when DOS > 85% in the locations in Table 5-4.

5.3.4 Prediction of Freeze-thaw Cycles using Weather Station Data

From the Local Climatological Data (LCD), the temperature over time can be obtained. Assuming the temperature is the concrete temperature, given the DOS of concrete, the freeze-thaw cycles can be obtained using Equation 5-2.

The method of calculating the freeze-thaw cycles using weather station data is as follows: (1) in each cycle when the weather station temperature is below 0°C, the DOS of the concrete right before the temperature goes below 0°C is calculated through linear interpolation using the measured DOS from the field instrument. (2) the freezing temperature (T_{freeze}) of the DOS in the previous step is calculated using Equation 5-2. (3) in each cycle where the weather station

temperature is below 0°C, the lowest temperature within this cycle is determined as T_{low}. (4) if T_{low} is lower than T_{freeze}, then the concrete is determined to freeze in this cycle, otherwise, it is determined to not freeze.

Using the above method, the freeze-thaw cycles at the 51mm depth of the six locations are estimated using the weather station temperature. The 51mm depth is used because it is typically the depth that has the most freeze-thaw cycles in the 6 locations. Table 5-12 shows the summary of the calculated freeze-thaw cycles. The measured freeze-thaw cycles are also added to show a comparison with the method using weather station data.

It can be noted from Table 5-12 that the evaluation using weather station data gives a close estimation of the measured freeze-thaw cycles in half of the locations (locations 1,2 and 6) and the evaluation is not as close in the other locations.

In location 3, the evaluated freeze-thaw cycles are 30% less than the measured value. This is because the weather station temperature didn't reflect the temperature change inside the concrete as shown in Figure 5-13. The weather station is 11.2 km away from the field instrument. In Figure 5-13 (a), from January 2nd to 29th, the weather station temperature is continuously below 0°C, as a result, this time range is calculated as 1 freeze-thaw cycle. However, there were 8 times the concrete temperature went above 0°C from the field measurement and this resulted in 8 more freeze-thaw cycles of the measured value than the weather station value. Besides, on January 30th, the weather station temperature was above 0°C, however, the concrete temperature was measured below 0°C and reached the freezing point which added another freeze-thaw cycle to the measured value.

In location 4, the weather station is 3.7km away from the concrete samples, and the evaluated freeze-thaw cycles are 20% more than the measured value. As shown in Figure 5-14, this is because, from the weather station temperature, in some cycles, when the temperature is below

0°C (for example, on March 4th, 5th, and 17th), the lowest temperature from the weather station is lower than the concrete temperature and passed the freezing point. This results in more freeze-thaw cycles using weather station data. Similarly, in location 5, the weather station is 35km away from the concrete samples, and the number of evaluated freeze-thaw cycles is almost twice the measured value. This is also because the weather station temperature is lower than the concrete temperature. As shown in Figure 5-15, on November 10th, 12th, 15th, and 16th, the weather station temperature is lower than the concrete temperature and exceeded the freezing point, which results in 4 more calculated freeze-thaw cycles in the selected time range.

Table 5-12. Summary of freeze-thaw cycles at 51mm depth from 11/2020 to 4/2021 calculated using the weather station temperature.

Location	Freezing events at 51 mm		Freezing events with DOS > 80%		Freezing events with DOS > 85%		Freezing events with DOS > 90%	
	Measured	Weather station	Measured	Weather station	Measured	Weather station	Measured	Weather station
#1	50	43	50	43	2	1	0	0
#2	69	52	69	52	11	18	0	0
#3	108	73	108	73	108	71	103	63
#4	58	72	58	72	57	71	2	5
#5	40	79	39	78	30	53	15	12
#6	60	59	60	59	60	59	59	59

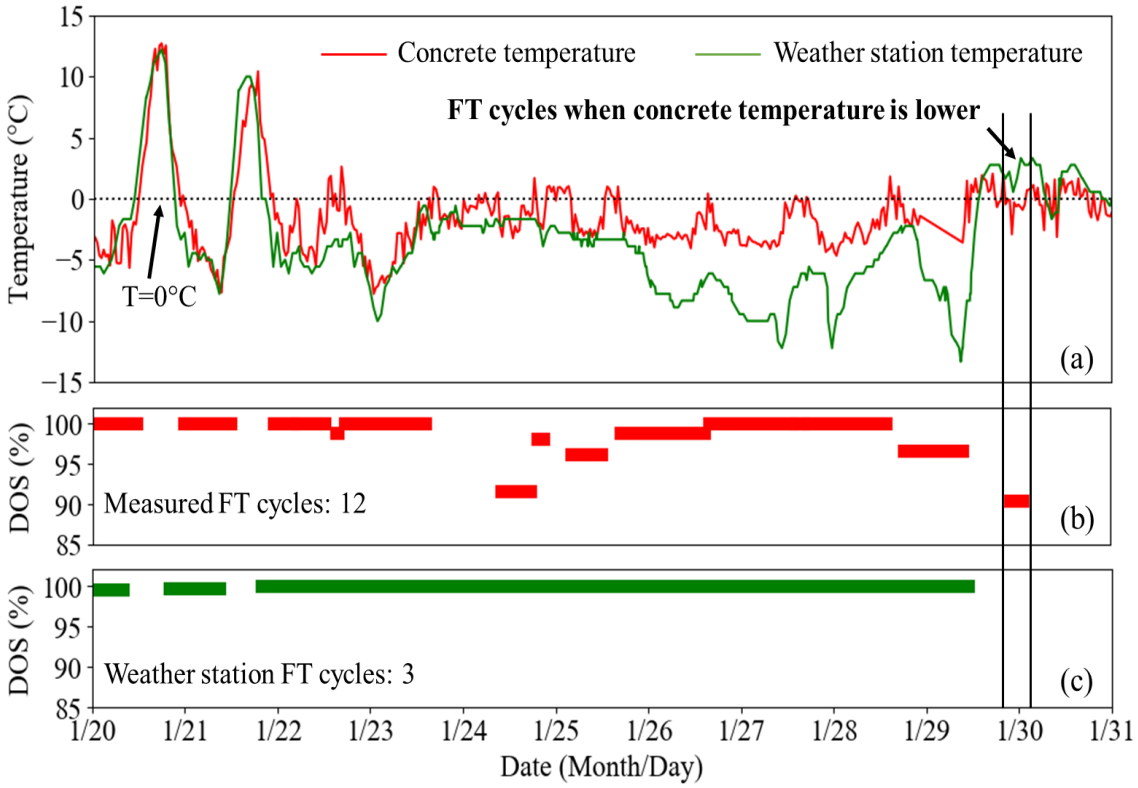

Figure 5-13. Freeze-thaw cycles at 51mm depth from the weather station data compared with the measured freeze-thaw cycles of the field instrument in location 3 from 1/20/2021 to 1/31/2021: (a) temperature over time, (b) DOS when concrete is measured to freeze, (c) DOS when concrete is predicted to freeze from the weather station.

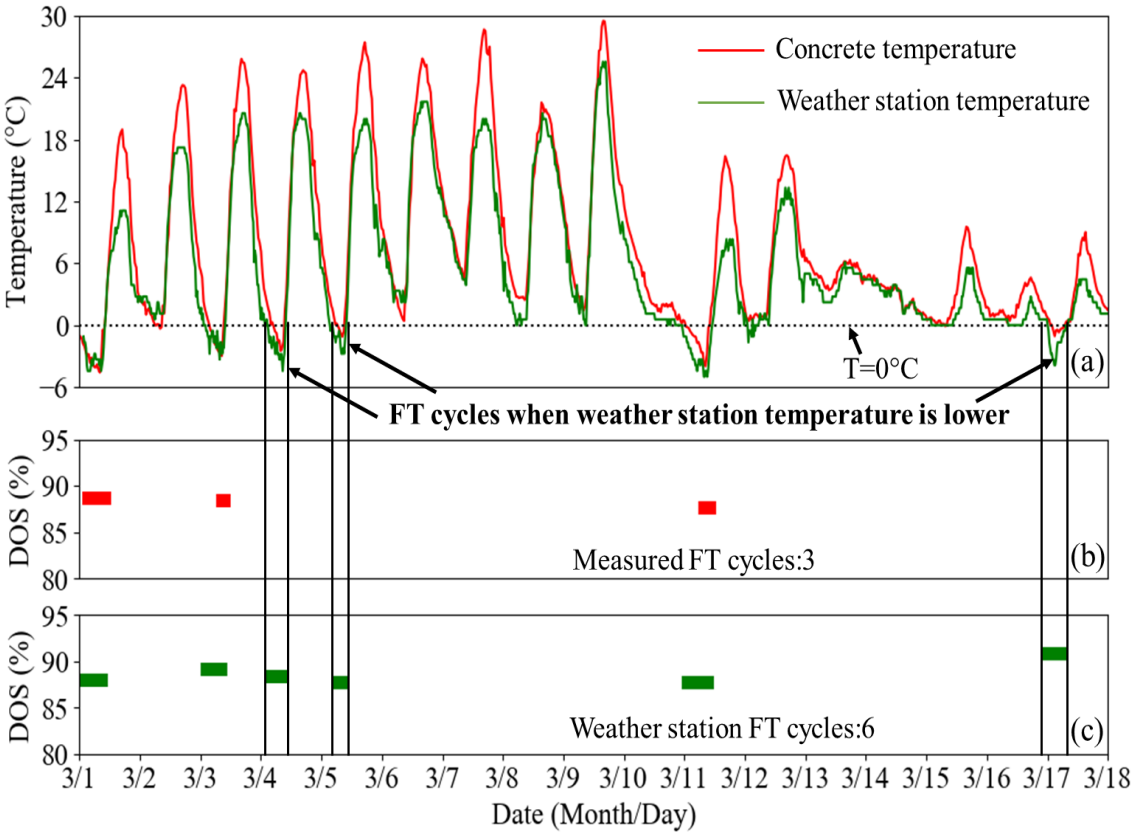

Figure 5-14. Freeze-thaw cycles at 51mm depth from the weather station data compared with the measured freeze-thaw cycles of the field instrument in location 4 from 3/1/2021 to 3/18/2021: (a) temperature over time, (b) DOS when concrete is measured to freeze, (c) DOS when concrete is predicted to freeze from the weather station.

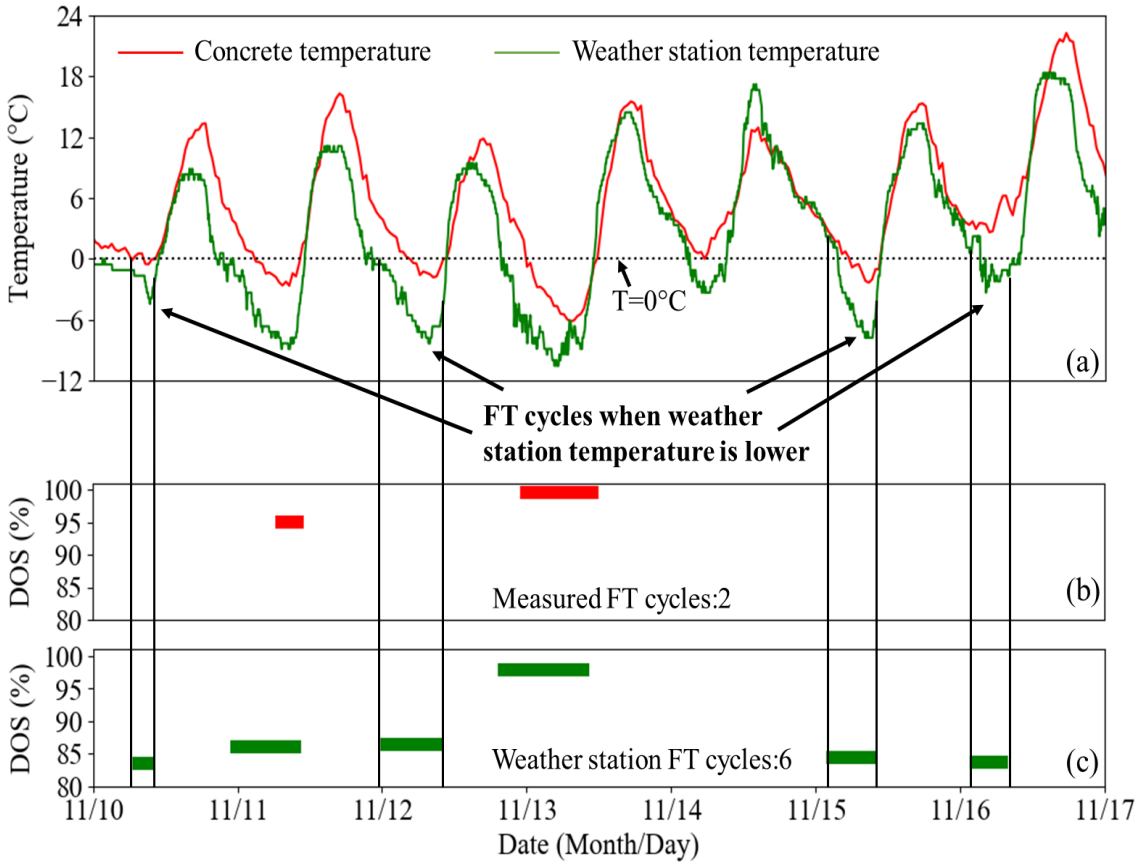

Figure 5-15. Freeze-thaw cycles at 51mm depth from the weather station data compared with the measured freeze-thaw cycles of the field instrument in location 5 from 11/10/2021 to 11/17/2021: (a) temperature over time, (b) DOS when concrete is measured to freeze, (c) DOS when concrete is predicted to freeze from the weather station.

5.4 Practical Significance

This chapter continues the work of the previous chapter and extends the method of determining freeze-thaw cycles using Equation 5-2 in another 6 different geological locations. This work proves the usability of using Equation 5-2 to determine to freeze-thaw cycles of concrete in different locations, and it is important to better understand how effective freeze-thaw cycles vary in different geographic conditions. A method of using weather station data to determine freeze-thaw cycles is presented and the method shows good predictions when the weather station is close

to the concrete and represents the temperature change of concrete. This method could establish a procedure to allow local weather conditions to predict the number of freeze-thaw cycles in the field.

5.5 Conclusions

In this study, the experimental method has been extended to examine the field data from 6 different locations and presented a method to predict the freeze-thaw events using weather station data. The following observations can be drawn:

- The 13mm depth is sensitive to the wetting and drying from precipitation in all the locations. The depth at 51mm is not as sensitive but is sometimes modified by precipitation events.
- In all the locations, resistivity increases as a freezing event are detected in the field samples and this generates the abnormal change of DOS within freeze-thaw cycles.
- In all the locations, the field samples formed ice more often in the middle depths (51 mm from the sample surface) of the sample and this is because the DOS is higher at this depth than the others.
- Locations in the east of Nebraska and Kansas have more precipitation and also more effective freeze-thaw cycles than on the western side.
- The average air temperature is also an indication of the number of freeze-thaw cycles.
- Small changes in the temperature can make a significant difference in the predicted number of effective freeze-thaw cycles.
- The air temperature from the weather station can be used to predict freeze-thaw cycles in the concrete samples if the air temperature closely matches the temperature in the concrete samples.

The work presented in this paper continues the work to establish a procedure to determine the relative number of effective freeze-thaw cycles based on local weather conditions. This study shows the potential of using weather station temperature to predict freeze-thaw cycles of concrete. This method is being extended to a larger number of locations and brings more insights into effective freezing events in the field.

CHAPTER VI

CONCLUSIONS

6.1 Overview

The main tasks of this research were to:

- Chapter 2: Use electrical resistivity to make direct measurements of concrete over the first 72h of hydration with air, sealed, and wet curing methods at different depths of a mortar sample. Determine a correlation between resistivity and DOS, tensile strength, and porosity. Establish resistivity as a method that can be used to determine the effectiveness of different curing methods and provide insights into the properties of the sample.
- Chapter 3: Investigate the influence of wet curing applied at different times in different evaporative environments using electrical resistivity, DOS, porosity, and the diffusion coefficient. This work examines the measurements in evaporation rates between 0.15 kg/m2/h and 0.85 kg/m2/h, which are commonly observed in practice. This work provides guidance on the allowable delay in applying the wet curing before the properties of the concrete are compromised.

- Chapter 4: Develop a novel method to simultaneously measure the DOS, ice formation, and temperature at different depths of a concrete sample in the field. An equation for calculating the temperature when ice forms and thaws for samples with different DOS was obtained using calibration samples. This method is first applied to the field samples in 2 locations in Oklahoma and makes several important observations based on the gathered data. It presents a practical approach to making widespread measurements of the number of effective freeze-thaw cycles in field concretes.
- Chapter 5: Apply the above method to 6 different locations and prove that the method of determining DOS and freeze-thaw cycles is applicable for other locations with different weather conditions. A method of using weather station temperature is proposed to predict the concrete freeze-thaw cycles and the result is compared with the field measurements.

The conclusion from each chapter is included below.

6.2 Using Electrical Resistivity to Predict Early Age DOS and Tensile Strength of Mortar

A new technique of comparing curing effects using electrical resistivity at different depths was investigated in this study. The electrical resistivity was compared between wet curing, sealed curing, and air curing methods, at different depths within the sample and at different hydration times. These measurements are compared to the porosity, DOS, and tensile strength of the sample, and a linear relationship between resistivity and DOS is created for these materials. The following conclusions can be drawn for mortar between 12h and 72h:

- Resistivity corresponds to the degree of saturation, porosity, and tensile strength of a mortar mixture.

- A linear relationship is developed between resistivity and degree of saturation and this relationship changes as hydration proceeds.

- A bi-linear relationship exists between resistivity and porosity at a fixed DOS that is high enough to promote hydration.

- Wet curing samples showed uniform moisture gradients and had the highest degree of saturation and tensile strength of the samples measured. These samples also showed a 0.5% increase in the mass over the first 20 h of hydration.

- The air cured sample at 23°C and 50% relative humidity environment showed a significant drying gradient over the top 85 mm and the refinement of the pore structure stopped after 48 h. This sample also showed a 0.78% decrease in the mass over the first 70 h of hydration.

- The sealed sample showed a uniform moisture gradient and had a degree of saturation, porosity, and tensile strength that is between the wet cured and air ured samples. This sample showed only a slight change in mass during hydration which is likely from an imperfect seal.

- A porosity gradient was observed in all the mixtures regardless of the curing method used. This gradient is likely caused by differences in curing and also bleeding.

This work establishes a systematic method to use resistivity to rapidly and economically measure the in situ degree of saturation, porosity, and provide insights into the tensile strength of the concrete. This could provide a useful scientific and practical measurement technique for future work.

6.3 Early Age Hydration Investigation on Concrete with Wet Curing at Different Times

The influence of wet curing at different times was investigated in this study. The experiments were conducted under three different evaporation conditions for the first 72h of hydration. The diffusion coefficient, porosity, DOS, and resistivity of the sample were measured and compared between curing methods. The following conclusions can be drawn:

- The electrical resistivity measurements can show the loss in moisture over time in all three drying environments. When wet curing was applied to the surface after 9h of drying for the samples in the 0.15 kg/m^2/h and 0.55 kg/m^2/h evaporation rate, the resistivity decreased to values similar to the sample was never allowed to dry. However, in the 0.85 kg/m^2/h evaporation rate for at least 2h, the resistivity did not decrease to the same level as the sample continuously wet cured.

- At the 0.15 kg/m^2/h evaporation rate environment, delaying the wet curing for 6h did not impact the porosity of the sample. The diffusion coefficient was not impacted when the wet curing was delayed for 9h.

- At the 0.55 kg/m^2/h evaporation rate environment, delaying the wet curing for 3h did not impact the porosity of the sample. The diffusion coefficient was not impacted until the wet curing was delayed for 9h.

- The average porosity at 20 mm in depth is related to the resistivity gradient right before the application of curing in the 0.85 kg/m^2/h evaporation rate. The resistivity gradient was also useful in predicting the change in the diffusion coefficient in the 0.85 kg/m^2/h evaporation rate. This shows that the resistivity gradient in the sample during curing could be used to track changes in the surface porosity and the diffusion coefficient from drying.

This work would benefit from additional testing done in the field to verify the measurements and also to compare the predicted performance with a wider range of materials; however, the results show promise for establishing a method to measure the impacts of delaying wet curing in different environments on the porosity and diffusion coefficient of concrete.

6.4 Measuring Effective Freeze-Thaw Cycles in the Field

In this study, a method has been established to determine the temperature and DOS in mortar samples at varying depths that are surrounded by concrete and placed on soil. This process was calibrated with laboratory studies on a single mixture to establish ice formation and this was validated in the field. These processes can then be used to evaluate the DOS of the mortar when ice formation occurs. This information can be used to determine the number of damaging or effective freeze-thaw cycles by assuming the critical DOS based on previous studies. The following observations can be drawn from this work:

- The measured temperatures in the mortar samples show a good agreement with local air temperature measurements with the average difference being 1.7° C.

- The DOS at 12.7 mm from the surface was impacted by the wetting and drying of a rain event. The DOS at 25 mm lagged did not change until 20 h after the event and sometimes the DOS at 25 mm did not change after a rain event.

- By using the resistivity and temperature, the ice formation and the melting temperature has been established for a large mortar sample with different DOS with a polynomial regression equation. for the mixture and sample size in this work. These results show that mortars with DOS closer to 100% or greater than 90% will freeze closer to 0^{o} C and that mortars with DOS lower than 75% freeze at -5^{o} C. These laboratory results match field measurements of ice formation made with resistivity and temperature measurements.

- The number of times the air temperature around a sample went below 0^{o}C only roughly correlates with the number of freeze-thaw cycles observed. This highlights the importance of understanding the combination of DOS and temperature when determining the number of freezing events.

- The number of freezing events measured is approximately the same at each depth for two different field locations. This means that the insulation provided by the ground or the depth of the mortar didn't reduce the number of freezing events in the 178 mm thick samples.

- Because the DOS is typically lower at the surface, there were practically zero effective freezing events for the two locations between the surface and 25 mm in depth. For these two locations, the DOS at 51 mm is always greater than 85% and so each freezing event created an effective freeze-thaw cycle. The moisture gradients are important to understand the number of effective freeze-thaw cycles at different depths.

The work presented in this paper is an early step to establishing a procedure to determine the relative number of effective freeze-thaw cycles based on local weather conditions. This method is being extended to a larger number of locations and seasons to bring more insights into effective freezing events in the field.

6.5 Field Effective Freeze-thaw Cycles Monitoring and Comparison

In this study, the experimental method has been extended to examine the field data from 6 different locations and presented a method to predict the freeze-thaw events using weather station data. The following observations can be drawn:

- The 13mm depth is sensitive to the wetting and drying from precipitation in all the locations. The depth at 51mm is not as sensitive but is sometimes modified by precipitation events.

- In all the locations, resistivity increases as a freezing event are detected in the field samples and this generates the abnormal change of DOS within freeze-thaw cycles.
- In all the locations, the field samples formed ice more often in the middle depths (51 mm from the sample surface) of the sample and this is because the DOS is higher at this depth than the others.
- Locations in the east of Nebraska and Kansas have more precipitation and also more effective freeze-thaw cycles than on the western side.
- The average air temperature is also an indication of the number of freeze-thaw cycles.
- Small changes in the temperature can make a significant difference in the predicted number of effective freeze-thaw cycles.
- The air temperature from the weather station can be used to predict freeze-thaw cycles in the concrete samples if the air temperature closely matches the temperature in the concrete samples.

The work presented in this paper continues the work to establish a procedure to determine the relative number of effective freeze-thaw cycles based on local weather conditions. This study shows the potential of using weather station temperature to predict freeze-thaw cycles of concrete. This method is being extended to a larger number of locations and brings more insights into effective freezing events in the field.

6.6 Further Research

This work of studying wet curing applications at different times would benefit from additional testing done in the field to verify the measurements and also to compare the predicted performance with a wider range of materials. The results of wet curing work show promise for

establishing a method to measure the impacts of delaying wet curing in different environments on the porosity and diffusion coefficient of concrete.

Examining the data of field instruments in all the other locations and comparing the freeze-thaw details of different locations will provide more information on examining the local freeze-thaw performance of concrete. It will also contribute to refining the model of predicting the freeze-thaw cycles using weather station data.

REFERENCES

[1] A. M. Neville, “Properties of concrete (vol. 4): Longman London,” 1995.

[2] M. Safiuddin, S. N. Raman, and M. F. M. Zain, “Effect of different curing methods on the properties of microsilica concrete,” *Australian Journal of Basic and Applied Sciences*, vol. 1, no. 2, pp. 87–95, 2007.

[3] N. Gowripalan, “Effect of curing on durability,” *Concrete International*, vol. 12, no. 2, pp. 47–54, 1990.

[4] S. Zhutovsky and K. Kovler, “Effect of internal curing on durability-related properties of high performance concrete,” *Cement and concrete research*, vol. 42, no. 1, pp. 20–26, 2012.

[5] S. H. Kosmatka, W. C. Panarese, and B. Kerkhoff, “Design and control of concrete mixtures (Vol. 5420, pp. 60077-1083),” *Skokie, IL: Portland Cement Association*, 2002.

[6] A. A. Ramezanianpour and V. M. Malhotra, “Effect of curing on the compressive strength, resistance to chloride-ion penetration and porosity of concretes incorporating slag, fly ash or silica fume,” *Cement and concrete composites*, vol. 17, no. 2, pp. 125–133, 1995.

[7] F. R. Montgomery, P. A. M. Basheer, and A. E. Long, “Influence of curing conditions on the durability related properties of near surface concrete and cement mortars,” *Special Publication*, vol. 131, pp. 127–138, 1992.

[8] M. F. M. Zain and Y. Matsufuji, “The influence of curing methods on the physical properties of high strength concrete exposed to medium temperature (20–50 ^{o}C),” presented at the the Proceedings of the Fifth International Conference on Concrete Engineering and Technology, Kuala Lumpur, Malaysia, 1997.

[9] M. F. M. Zain, M. Safiuddin, and K. M. Yusof, “Influence of different curing conditions on strength and durability of high-performance concrete,” *ACI Special Publications*, vol. 193, pp. 275–292, 2000.

[10] A. Hajibabaee, M. K. Moradllo, A. Behravan, and M. T. Ley, “Quantitative measurements of curing methods for concrete bridge decks,” *Construction and Building Materials*, vol. 162, pp. 306–313, 2018.

[11] M. Mainguy, O. Coussy, and V. Baroghel-Bouny, “Role of air pressure in drying of weakly permeable materials,” *Journal of engineering mechanics*, vol. 127, no. 6, pp. 582–592, 2001.

[12] G. Fagerlund, “Critical degrees of saturation at freezing of porous and brittle materials,” Doctoral Thesis (monograph), Tid. Institutionen för byggnadsteknik, Tekniska högskolan i Lund, 1973.

[13] W. Li, M. Pour-Ghaz, J. Castro, and J. Weiss, “Water absorption and critical degree of saturation relating to freeze-thaw damage in concrete pavement joints,” *Journal of Materials in Civil Engineering*, vol. 24, no. 3, pp. 299–307, 2012.
[14] ASTM C666/C666M-15, *Standard Test Method for Resistance of Concrete to Rapid Freezing and Thawing*. 2015. Accessed: Mar. 16, 2022. [Online]. Available: https://www.astm.org/c0666_c0666m-15.html
[15] A. Hajibabaee and M. T. Ley, “Impact of Wet and Sealed Curing on Curling in Cement Paste Beams from Drying Shrinkage.,” *ACI Materials Journal*, vol. 112, no. 1, 2015.
[16] B. J. Christensen *et al.*, “Impedance spectroscopy of hydrating cement-based materials: measurement, Interpretation, and application,” *Journal of the American Ceramic Society*, vol. 77, no. 11, pp. 2789–2804, 1994.
[17] P. Gu, Z. Xu, P. Xie, and J. J. Beaudoin, “Application of AC impedance techniques in studies of porous cementitious materials:(I): influence of solid phase and pore solution on high frequency resistance,” *Cement and Concrete Research*, vol. 23, no. 3, pp. 531–540, 1993.
[18] W. J. McCarter and A. B. Afshar, “Monitoring the early hydration mechanisms of hydraulic cement,” *Journal of materials science*, vol. 23, no. 2, pp. 488–496, 1988.
[19] Z. Li, X. Wei, and W. Li, “Preliminary interpretation of Portland cement hydration process using resistivity measurements,” *Materials Journal*, vol. 100, no. 3, pp. 253–257, 2003.
[20] L. Xiao, “Interpretation of hydration process of concrete based on electrical resistivity measurement,” PhD Thesis, Hong Kong University of Science and Technology, Hong Kong, 2007.
[21] P. Ghoddousi and L. A. Saadabadi, “Study on hydration products by electrical resistivity for self-compacting concrete with silica fume and metakaolin,” *Construction and Building Materials*, vol. 154, pp. 219–228, 2017.
[22] D. S. McLachlan, M. Blaszkiewicz, and R. E. Newnham, “Electrical resistivity of composites,” *Journal of the American Ceramic Society*, vol. 73, no. 8, pp. 2187–2203, 1990.
[23] D. S. McLachlan *et al.*, “The temperature and volume fraction dependence of the resistivity of granular Al-Ge near the percolation threshold,” *Journal of Physics: Condensed Matter*, vol. 5, no. 27, p. 4829, 1993.
[24] J. Zhang and Z. Li, “Application of GEM equation in microstructure characterization of cement-based materials,” *Journal of materials in civil engineering*, vol. 21, no. 11, pp. 648–656, 2009.
[25] ASTM, C305, *Standard Practice for Mechanical Mixing of Hydraulic Cement Pastes and Mortars of Plastic Consistency*. 2020. Accessed: Mar. 16, 2022. [Online]. Available: https://www.astm.org/c0305-20.html
[26] E. Tazawa, S. Miyazawa, and T. Kasai, “Chemical shrinkage and autogenous shrinkage of hydrating cement paste,” *Cement and concrete research*, vol. 25, no. 2, pp. 288–292, 1995.
[27] ASTM, C642, *Standard Test Method for Density, Absorption, and Voids in Hardened Concrete*. 2021. Accessed: Mar. 16, 2022. [Online]. Available: https://www.astm.org/c0642-21.html

[28] T. C. Powers, “A discussion of cement hydration in relation to the curing of concrete,” in *Highway Research Board Proceedings*, 1948, vol. 27.
[29] L. E. Copeland and R. H. Bragg, “Self-desiccation in Portland cement pastes,” ASTM Bulletin No. 204, 1955.
[30] L. J. Parrott, “Load induced dimensional changes of hardened cement paste,” PhD Thesis, King’s College London, 1973.
[31] R. G. Patel, D. C. Killoh, L. J. Parrott, and W. A. Gutteridge, “Influence of curing at different relative humidities upon compound reactions and porosity in Portland cement paste,” *Materials and Structures*, vol. 21, no. 3, pp. 192–197, 1988.
[32] V. Baroghel-Bouny, P. Mounanga, A. Khelidj, A. Loukili, and N. Rafaï, “Autogenous deformations of cement pastes: part II. W/C effects, micro–macro correlations, and threshold values,” *Cement and Concrete Research*, vol. 36, no. 1, pp. 123–136, 2006.
[33] R. J. Flatt, G. W. Scherer, and J. W. Bullard, “Why alite stops hydrating below 80% relative humidity,” *Cement and Concrete Research*, vol. 41, no. 9, pp. 987–992, 2011.
[34] B. Robertson, E. McArtor, M. Dickey, D. Cook, and M. T. Ley, “Development of concrete mixtures to mitigate bridge deck cracking,” Oklahoma Department of Transportation (ODOT), Oklahoma City, OK, ODOT SP&R Item Number 22742274, 2020.
[35] M. Dickey, “Additives to Improve the Performance of Concrete,” School of Civil and Environmental Engineering, Oklahoma State University, Stillwater, OK, 2021.
[36] ACI Committee 305, “ACI 305R-20, Guide to Hot Weather Concreting,” *Technical Documents*, Oct. 2020.
[37] L. Chen and M. T. Ley, “Real Time Measurement of Degree of Saturation and Tensile Strength of Mortar with Electrical Resistivity,” *Cement and Concrete Composites. (Submitted)*, 2021.
[38] M. K. Moradllo and M. T. Ley, “Quantitative measurement of the influence of degree of saturation on ion penetration in cement paste by using X-ray imaging,” *Construction and Building Materials*, vol. 141, pp. 113–129, 2017.
[39] M. K. Moradllo and M. T. Ley, “Comparing ion diffusion in alternative cementitious materials in real time by using non-destructive X-ray imaging,” *Cement and Concrete Composites*, vol. 82, pp. 67–79, 2017.
[40] M. K. Moradllo, Q. Hu, and M. T. Ley, “Using X-ray imaging to investigate in-situ ion diffusion in cementitious materials,” *Construction and Building Materials*, vol. 136, pp. 88–98, 2017.
[41] M. K. Moradllo *et al.*, “Using micro X-ray fluorescence to image chloride profiles in concrete,” *Cement and Concrete Research*, vol. 92, pp. 128–141, 2017.
[42] K. C. Hover, “After Two Hundred Years of Estimating Evaporation, It Is Still a Mystery,” *Special Publication*, vol. 338, pp. 10–28, 2020.
[43] M. Kosior-Kazberuk and W. Jezierski, “Surface scaling resistance of concrete modified with bituminous addition,” *Journal of Civil Engineering and Management*, vol. 10, no. 1, pp. 25–30, 2004.
[44] S. Jacobsen, “Calculating liquid transport into high-performance concrete during wet freeze/thaw,” *Cement and Concrete Research*, vol. 35, no. 2, pp. 213–219, 2005.

[45] J. J. Beaudoin and C. MacInnis, “The mechanism of frost damage in hardened cement paste,” *Cement and Concrete Research*, vol. 4, no. 2, pp. 139–147, 1974.
[46] D. P. Bentz, M. A. Ehlen, C. F. Ferraris, and E. J. Garboczi, “Sorptivity-based service life predictions for concrete pavements,” in *7th International Conference on Concrete Pavements*, 2001, vol. 1, pp. 9–13.
[47] L. Sutter, T. Van Dam, K. R. Peterson, and D. P. Johnston, “Long-term effects of magnesium chloride and other concentrated salt solutions on pavement and structural Portland cement concrete,” *Transportation research record*, vol. 1979, no. 1, pp. 60–68, 2006.
[48] Z. Sun, D. Kumpf, and G. W. Scherer, “Kinetics of ice growth in concrete,” *Proc. 12th Int. Cong. Cement Chemistry. Paper W4-07.1. Beaudoin, J. J, Makar, J. M., Raki, L. Ed., National Research Council of Canada, Montreal, Canada*, 2007.
[49] C. Leech, D. Lockington, R. D. Hooton, G. Galloway, G. Cowin, and P. Dux, “Validation of Mualem’s conductivity model and prediction of saturated permeability from sorptivity,” *ACI Materials Journal*, vol. 105, no. 1, p. 44, 2008.
[50] D. H. Bager and E. J. Sellevold, “Ice formation in hardened cement paste, part I—Room temperature cured pastes with variable moisture contents,” *Cement and Concrete Research*, vol. 16, no. 5, pp. 709–720, 1986.
[51] Y. Farnam, H. Todak, R. Spragg, and J. Weiss, “Electrical response of mortar with different degrees of saturation and deicing salt solutions during freezing and thawing,” *Cement and Concrete Composites*, vol. 59, pp. 49–59, 2015.
[52] V. R. Schaefer and K. Wang, “Mix design development for pervious concrete in cold weather climates,” Iowa. Dept. of Transportation. Highway Division, 2006.
[53] K. Wang, V. R. Schaefer, J. T. Kevern, and M. T. Suleiman, “Development of mix proportion for functional and durable pervious concrete,” in *NRMCA concrete technology forum: focus on pervious concrete*, 2006, pp. 1–12.
[54] Z. Yang, H. Brown, and A. Cheney, “Influence of moisture conditions on freeze and thaw durability of Portland cement pervious concrete,” in *Concrete Technology Forum: Focus on Pervious Concrete*, 2006, pp. 24–25.
[55] V. Henderson and S. Tighe, “Evaluation of pervious concrete pavement performance in cold weather climates,” *International Journal of Pavement Engineering*, vol. 13, no. 3, pp. 197–208, 2012.
[56] Y. Shimizu, “An electrical method for measuring the setting time of portland cement,” *Mill Section of Concrete*, vol. 32, no. 5, pp. 111–113, 1928.
[57] W. J. McCarter and P. N. Curran, “The electrical response characteristics of setting cement paste,” *Magazine of Concrete research*, vol. 36, no. 126, pp. 42–49, 1984.
[58] A. A. Ramezanianpour, A. Pilvar, M. Mahdikhani, and F. Moodi, “Practical evaluation of relationship between concrete resistivity, water penetration, rapid chloride penetration and compressive strength,” *Construction and Building Materials*, vol. 25, no. 5, pp. 2472–2479, 2011.
[59] L. Tang, L.-O. Nilsson, and P. M. Basheer, *Resistance of concrete to chloride ingress: Testing and modelling*. CRC Press, 2011.
[60] L. Lemoine, F. Wenger, and J. Galland, “Study of the Corrosion of Concrete Reinforcement by Electrochemical Impedance Measurement,” in *Corrosion Rates of Steel in Concrete*, ASTM STP 1065, 1990, pp. 118–133.

[61] N. Wiwattanachang and P. H. Giao, “Monitoring crack development in fiber concrete beam by using electrical resistivity imaging,” *Journal of Applied Geophysics*, vol. 75, no. 2, pp. 294–304, 2011.
[62] M. Niemuth, “Using impedance spectroscopy to detect flaws in concrete,” *Master of Science, Purdue University, West Lafayette, IN*, 2004.
[63] T. Sato and J. J. Beaudoin, “An AC impedance spectroscopy study of freezing phenomena in wollastonite micro-fibre reinforced cement paste,” in *Proceedings of the international symposium on role of cement science in sustainable development, Scotland, UK, Sep*, 2003, pp. 3–4.
[64] R. T. Coverdale, B. J. Christensen, T. O. Mason, H. M. Jennings, and E. J. Garboczi, “Interpretation of the impedance spectroscopy of cement paste via computer modelling,” *Journal of materials science*, vol. 29, no. 19, pp. 4984–4992, 1994.
[65] Y. Sang and Y. Yang, “Assessing the freezing process of early age concrete by resistivity method,” *Construction and Building Materials*, vol. 238, p. 117689, 2020.
[66] H. Cai and X. Liu, “Freeze-thaw durability of concrete: ice formation process in pores,” *Cement and concrete research*, vol. 28, no. 9, pp. 1281–1287, 1998.
[67] F. Rajabipour, J. Weiss, J. D. Shane, T. O. Mason, and S. P. Shah, “Procedure to interpret electrical conductivity measurements in cover concrete during rewetting,” *Journal of materials in civil engineering*, vol. 17, no. 5, pp. 586–594, 2005.
[68] W. Morris, E. I. Moreno, and A. A. Sagüés, “Practical evaluation of resistivity of concrete in test cylinders using a Wenner array probe,” *Cement and concrete research*, vol. 26, no. 12, pp. 1779–1787, 1996.
[69] R. P. Spragg, J. Castro, T. Nantung, M. Paredes, and J. Weiss, “Variability analysis of the bulk resistivity measured using concrete cylinders,” *Advances in Civil Engineering Materials*, vol. 1, no. 1, pp. 1–17, 2012.
[70] R. Spragg, C. Villani, K. Snyder, D. Bentz, J. W. Bullard, and J. Weiss, “Factors that influence electrical resistivity measurements in cementitious systems,” *Transportation research record*, vol. 2342, no. 1, pp. 90–98, 2013.
[71] Y. Liu and F. Presuel-Moreno, “Effect of Elevated Temperature Curing on Compressive Strength and Electrical Resistivity of Concrete with Fly Ash and Ground-Granulated Blast-Furnace Slag.,” *ACI Materials Journal*, vol. 111, no. 5, 2014.
[72] S. Kang, M. T. Ley, Z. Lloyd, and T. Kim, “Using the Particle Model to predict electrical resistivity performance of fly ash in concrete,” *Construction and Building Materials*, vol. 261, p. 119975, 2020.
[73] J.-K. Kim and C.-S. Lee, “Prediction of differential drying shrinkage in concrete,” *Cement and Concrete Research*, vol. 28, no. 7, pp. 985–994, 1998.
[74] ASTM, E104, *Standard Practice for Maintaining Constant Relative Humidity by Means of Aqueous Solutions*. 2020. Accessed: Mar. 20, 2022. [Online]. Available: https://www.astm.org/e0104-20a.html
[75] A. T. Coyle, R. P. Spragg, P. Suraneni, A. N. Amirkhanian, M. Tsui-Chang, and W. J. Weiss, “Activation Energy of Conduction for Use in Temperature Corrections on Electrical Measurements of Concrete,” *Advances in Civil Engineering Materials*, vol. 8, no. 1, pp. 158–170, 2019.

[76] G. Sant, F. Rajabipour, and J. Weiss, “The influence of temperature on electrical conductivity measurements and maturity predictions in cementitious materials during hydration,” 2008.
[77] M. Nokken, A. Boddy, X. Wu, and R. D. Hooton, “Effects of temperature, chemical, and mineral admixtures on the electrical conductivity of concrete,” *Journal of ASTM International*, vol. 5, no. 5, pp. 1–9, 2008.
[78] Y. A. Villagrán Zaccardi, J. Fullea García, P. Huélamo, and A. A. Di Maio, “Influence of temperature and humidity on Portland cement mortar resistivity monitored with inner sensors,” *Materials and corrosion*, vol. 60, no. 4, pp. 294–299, 2009.
[79] J. Cao and D. D. L. Chung, “Damage evolution during freeze–thaw cycling of cement mortar, studied by electrical resistivity measurement,” *Cement and Concrete Research*, vol. 32, no. 10, pp. 1657–1661, 2002.
[80] NOAA, “Local climatological data (LCD),” 2019. https://www.ncdc.noaa.gov/cdo-web/datatools/lcd (accessed Mar. 20, 2022).
[81] D. P. Bentz, M. A. Peltz, A. Duran-Herrera, P. Valdez, and C. A. Juarez, “Thermal properties of high-volume fly ash mortars and concretes,” *Journal of Building Physics*, vol. 34, no. 3, pp. 263–275, 2011.
[82] M. E. Schmalko, R. O. Morawicki, and L. A. Ramallo, “Simultaneous determination of specific heat capacity and thermal conductivity using the finite-difference method,” *Journal of Food Engineering*, vol. 31, no. 4, pp. 531–540, 1997.
[83] Devices, A. (2007). AD5933 Datasheet. Available: http://www. analog. com/media/en/technical-documentation/data-sheets/AD5933. pdf.
[84] Device, A. (2008). AD8531 Datasheet. Available: https://www.analog.com/media/en/technical-documentation/data-sheets/AD8531_8532_8534.pdf
[85] Device, A. (2015). ADG725 Datasheet. Available: https://www.analog.com/media/en/technical-documentation/data-sheets/ADG725_731.pdf
[86] Sullivan, J. F. (1998). Technical Physics. Wiley.
[87] Robertson, B., McArtor, E., Dickey, M., Ley, MT., Cook, D. (2020). Development of Concrete Mixtures to Mitigate Bridge Deck Cracking. Oklahoma Department of Transportation (ODOT). ODOT SP&R Item Number 2274. Final Report. Oklahoma City, OK.
[88] Dickey, M. (2021). Additives to Improve the Performance of Concrete. Thesis requirements for the degree of Master of Science, School of Civil and Environmental Engineering, Oklahoma State University at Stillwater, OK.
[89] INTEGRATED, M. (2015). MAX31855-Cold-Junction Compensated Thermocouple-to-Digital Converter.

APPENDICES

APPENDIX A: Seal the edge of the mortar sample

The steps of sealing the mortar sample edge are shown in **Figure A.** 1 (a). Wrap the mold top with plastic. Two layers of plastic were used on each sample. (b) Tighten the plastic with rubber bands. Five rubber bands were used for each sample. (c) Fold the plastic into the mold along the mold edge. (d) Cover the plastic with fresh mortar from the same mixture. The coverage of mortar formed a concentric circle with an inner diameter of 102 mm. and an outer diameter of 152 mm.

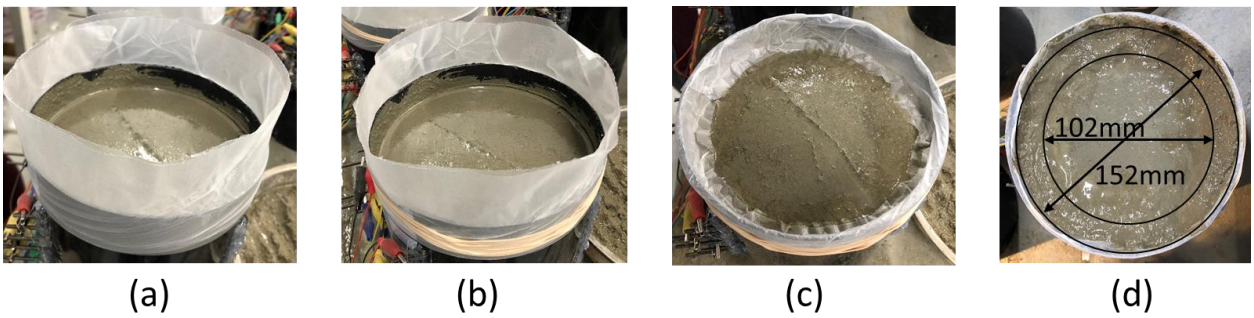

Figure A. 1. Steps of sealing the sample edge: (a) wrap the mold top with plastic, (b) tighten the plastic with rubber bands, (c) fold the plastic along the mold edge, and (d) cover the plastic with mortar.

APPENDIX B: Additional information on resistivity measurement

B.1: Supplementary hardware for the apparatus

Since the resistivity of the mortar samples at the early age of hydration was relatively low, it is necessary to adjust the AD5933 to the right range for the measurement. This is achieved by attenuating the excitation voltage from the AD5933 to reduce the signal current. As the result, an amplifier AD8531 was added to the circuit. An amplifier circuit can either amplify or attenuate the circuit signal. The purpose of the amplifier circuit is to ensure the AD5933 system is within the linear range when measuring the small resistivity of the mortar sample. As a result, the external amplifier attenuates the peak-to-peak voltage at the output point of the AD5933 circuit, thereby reducing the signal current flowing through the sample and minimizing the effect of the output series resistance in the resistivity calculations [83-84].

An AD5933 chip contains one input and output channel, which is only able to measure the resistivity value of one pair of rods. Therefore, a dual 16-to-1 channel, serial controlled analog multiplexer ADG725 was used in the circuit to upgrade the measuring ability of the AD5933 from 1 dual-channel to 16 dual channels [85]. Five multiplexers were used in the circuit for this study. This allows 80 channels to be measured at once. As a result, 11 mortar samples with 7 layers in each sample were able to be measured at the same time. An SD card recorder was combined into the circuit to record the data.

B.2: Resistivity raw data process

The first step of calculating the resistivity value is to get the magnitude of the DFT on AD5933 at the known frequency point. The magnitude of the DFT is given by ***Equation A. 1***, where R and I are the real and imaginary impedance obtained from the real and the imaginary data register

respectively on the AD5933. To convert the magnitude into an impedance, the magnitude needs to be multiplied by a scaling factor called the gain factor. The gain factor was obtained during the calibration of the apparatus with a known impedance connected with the circuit. In this study, a calibration resistor of 100 ohms and a frequency of 30 kHz was used and the gain factor was 8.54E-7 calculated from ***Equation A. 2***, where Magnitude calibration is the magnitude number obtained during calibration. With the gain factor, the unknown impedance at each depth of the mortar sample was calculated according to ***Equation A. 3***.

$$Magnitude = \sqrt{R^2 + I^2} \qquad \textbf{Equation A. 1}$$

$$Gain\ factor = (1 / 100\ ohms) / Magnitude_{\ calibration} \qquad \textbf{Equation A. 2}$$

$$Impedance = 1 / (Gain\ factor \times Magnitude_{\ unknown}) \qquad \textbf{Equation A. 3}$$

Since the frequency range selected has forced the imaginary impedance to close to 0, the measured impedance is also called the bulk resistance of the mortar sample.

APPENDIX C: Coefficient of determination of the linear regression between resistivity and DOS

Table A. 1. Parameters of the linear regression between resistivity and DOS in Figure 2-8.

Hydration time	12h	24h	48h	72h
R^2	0.82	0.96	0.98	0.96
Slope(% / (KΩ*cm))	-411.07	-572.67	-498.77	-443.00
Intercept(%)	105.29	120.71	127.60	128.89

APPENDIX D: Load to strength calculation

The schematic of the free body diagram is shown in Figure A. 2.

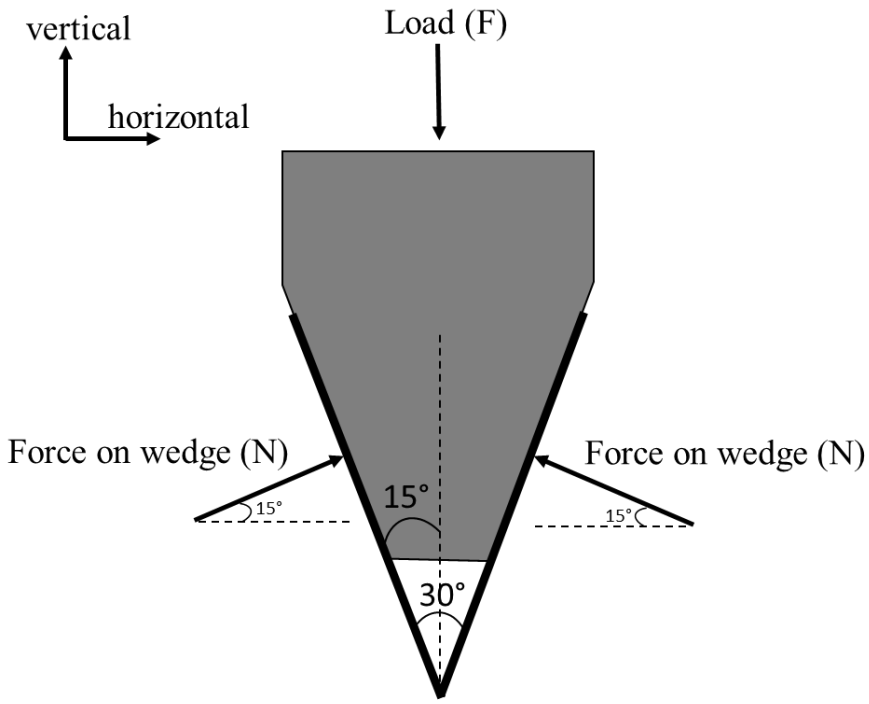

Figure A. 2. Schematic of the free body diagram.

Because there is no sliding observed during the test there is assumed to be no friction between the wedge and the load platen [86-88]. If the forces are summed in the vertical direction the force on the wedge (N) is equal to 1.93F. This horizontal component of this force is 1.86F and since there is a wedge on the top and the bottom of the beam the total horizontal force is 3.72F. The tension stress in the beam can be found by dividing this load by the effective area at the point of the crack. The diameter of the cylinder is 152.4 mm and the depth of each notch is 25.4 mm. This means the width of the sample is 101.6 mm. Since each sample is 76.2 mm deep, the cross-sectional area is 7741.9 mm^2. An image of the sample is shown in Figure A. 3.

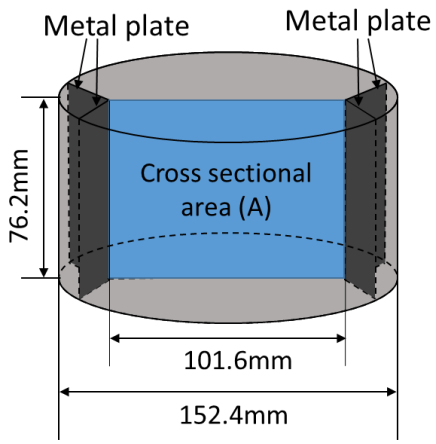

Figure A. 3. Schematic of the cross sectional area of the mortar sample for splitting test.

APPENDIX E: Top porosity vs the resistivity gradient in the same graph.

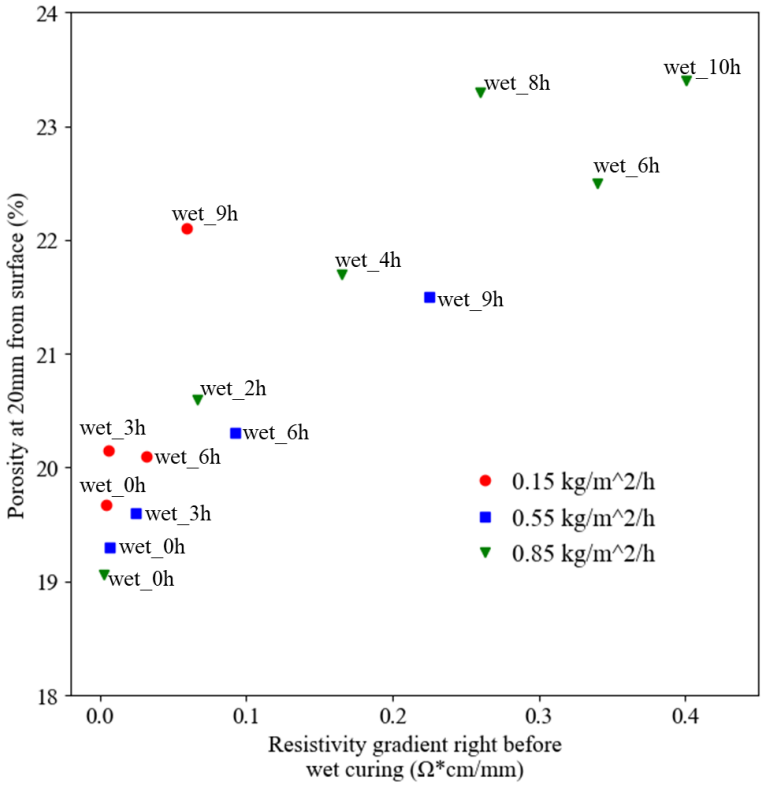

Figure A. 4. Porosity at 20 mm from the surface versus the resistivity gradient right before wet curing is applied for different drying environments.

APPENDIX F: Resistivity and temperature calculation

F.1: Resistivity calculation

A 12-Bit impedance converter AD5933 was the sensor used in this study for measuring resistivity. The AD5933 chip is an impedance converter system with high precision. It's a combination of an on-board frequency generator with a 12-bit, 1 Mega sample per second (MSPS), analog-to-digital converter (ADC). After initial calibrating with resistors of 560 ohms and 2000 ohms respectively, the magnitude and the relative phase of the impedance at the designated frequency are easily calculated [83].

After the AD5933 starts to work, the response signal from the mortar mix is sampled by its onboard ADC, and a discrete Fourier transform (DFT) is processed by its onboard digital signal processing (DSP) engine. The real (R) and imaginary (I) impedance are returned by the DFT algorithm at the designated frequency.

The first step of calculating the impedance value is to get the magnitude of the DFT on AD5933 at the known frequency point. The magnitude of the DFT is given by ***Equation A. 1***, where R and I are the real impedance and imaginary impedance obtained from the real data register and the imaginary data register respectively on the AD5933. To convert the magnitude number into an impedance, the magnitude needs to be multiplied by a scaling factor called the gain factor. The gain factor was obtained during the calibration of the apparatus with a known impedance connected with the circuit. In this study, a calibration impedance of 560 ohms and 2000 ohms at the frequency of 4KHz was used and the gain factors are 1.43E-7 and 4.84E-8 respectively calculated from ***Equation A. 2***, where Magnitude calibration is the magnitude number obtained during calibration. With the gain factor, the unknown impedance of each layer of the mortar

sample was calculated according to ***Equation A. 3***, where the Magnitude unknown is the DFT magnitude of each mortar layer calculated from ***Equation A. 1***.

F.2: Temperature calculation

A thermocouple-to-digital converter MAX31855T is the specific chip for measuring temperature. The MAX31855 is a sophisticated thermocouple-to-digital converter with a built-in 14-bit analog-to-digital converter (ADC). The MAX31855T performs cold-junction compensation sensing and correction and is available in several versions to digitize the signal from different types of thermocouples. The T-type thermocouple was used in this research. Signal-conditioning hardware is included in the MAX31855 to convert the thermocouple's signal into a voltage compatible with the input channels of the ADC. The two ends of the thermocouple wire T+ and T- connected to the data logger help reduce the introduced noise errors. The MAX31855 assumes a linear relationship between temperature and voltage to the device's output data. For a T-type thermocouple, the voltage changes by about 52.18µV/°C, which approximates the thermocouple characteristic based on ***Equation A. 4***, where VOUT is the thermocouple output voltage (µV), TR is the temperature of the remote thermocouple junction (°C), and T_{AMB} is the temperature of the device (°C) [89].

$$V_{OUT} = (52.18\mu V/°C) \times (T_R - T_{AMB}) \qquad \textit{Equation A. 4}$$

APPENDIX G: relationship between resistivity, temperature, and DOS for the mortar samples

The DOS is shown as a function of resistivity at different temperatures 49 to -18°C in Figure A. 5 below.

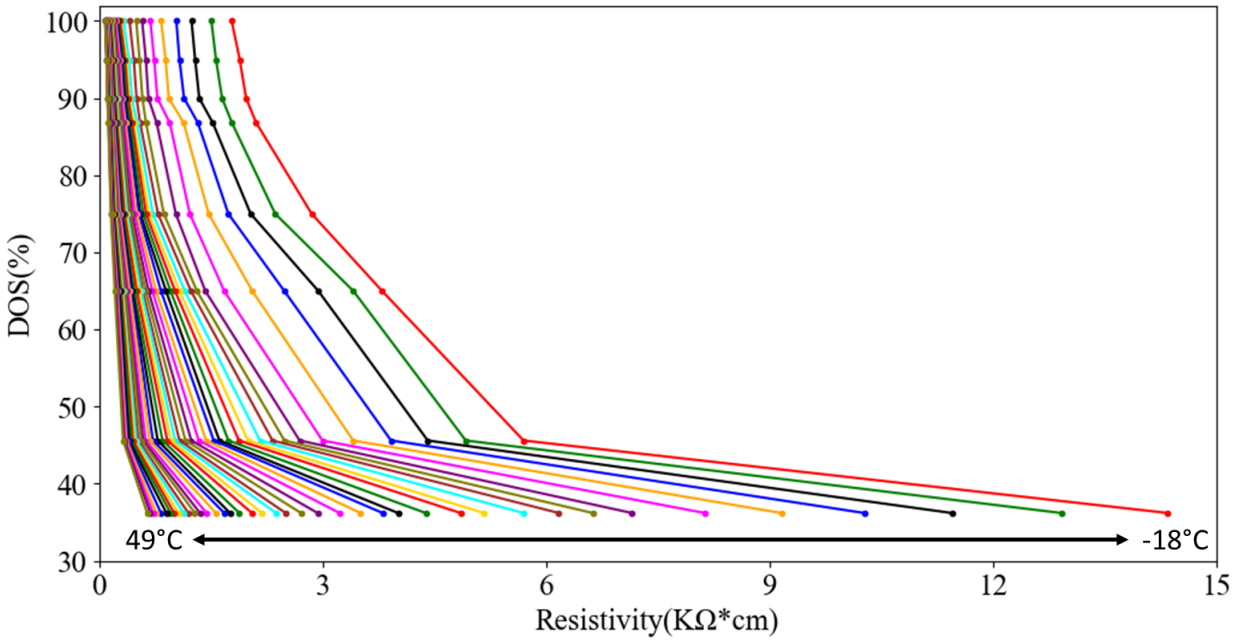

Figure A. 5. DOS represented as a function of resistivity at temperatures from 49°C to -18°C.

With the data set from the calibration samples, if given the temperature and resistivity, the DOS of a sample can be evaluated through 2 steps of linear interpolation. For example, Figure A. 6 shows an isotherm of 20°C obtained through linear interpolation between 21°C and 17°C. With the isotherm of 20°C, given a resistivity value of 0.4 KΩ*cm, the DOS can be evaluated as 70% through another step of linear interpolation.

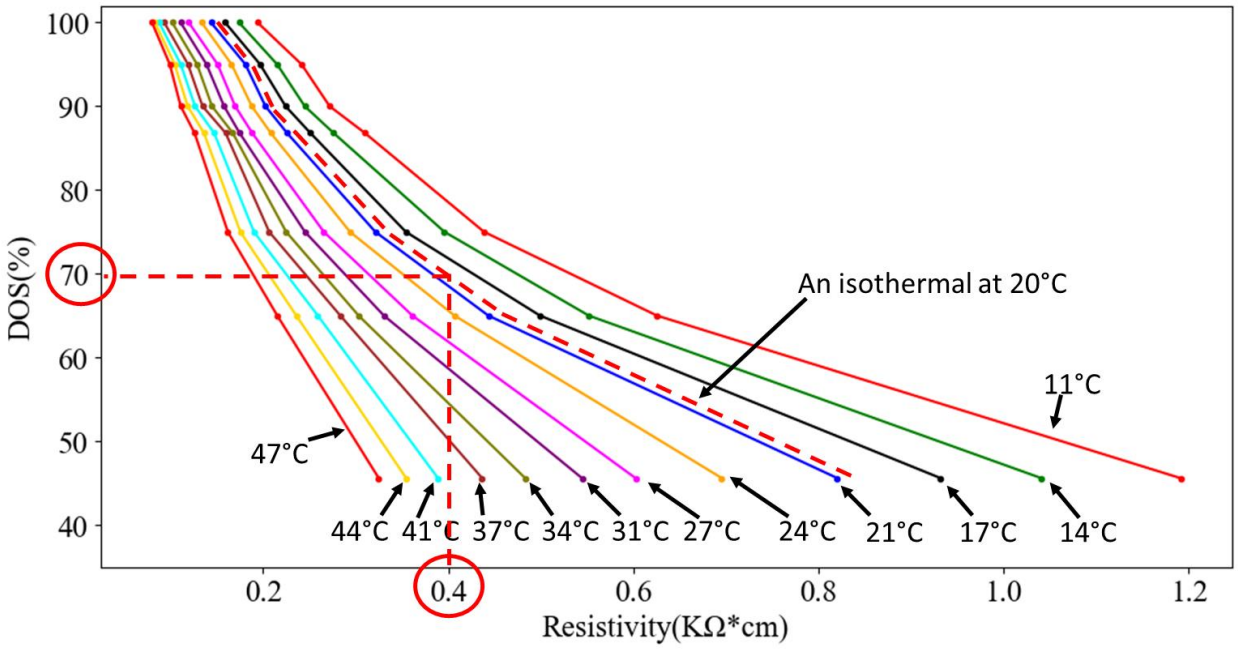

Figure A. 6. Evaluation of DOS using 2 steps of linear interpolation.

APPENDIX H: RH and precipitations of locations A and B from the weather station.

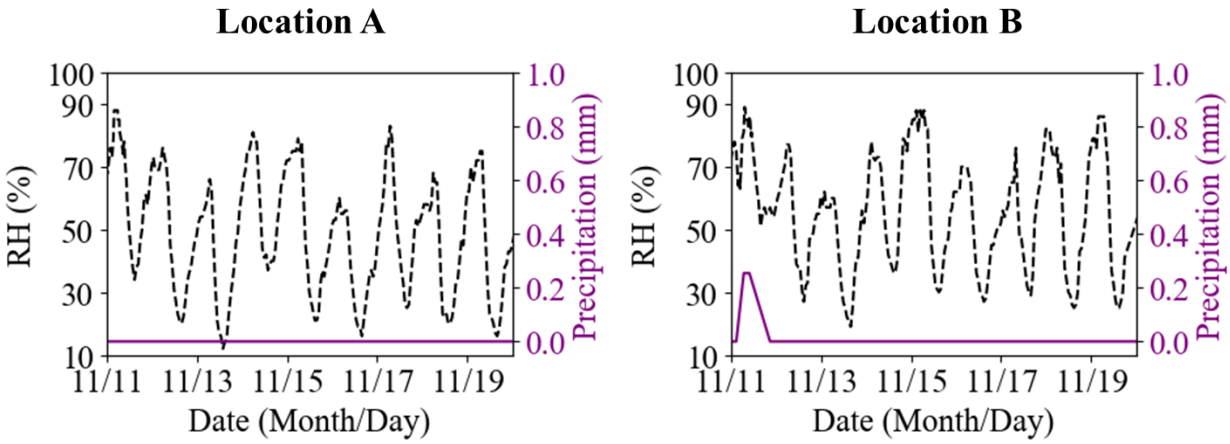

Figure A. 7. RH and precipitations of locations A and B from the weather stations from November 11th to 19th, 2019.

APPENDIX I: Temperature, DOS, and resistivity curve within the freeze-thaw cycles

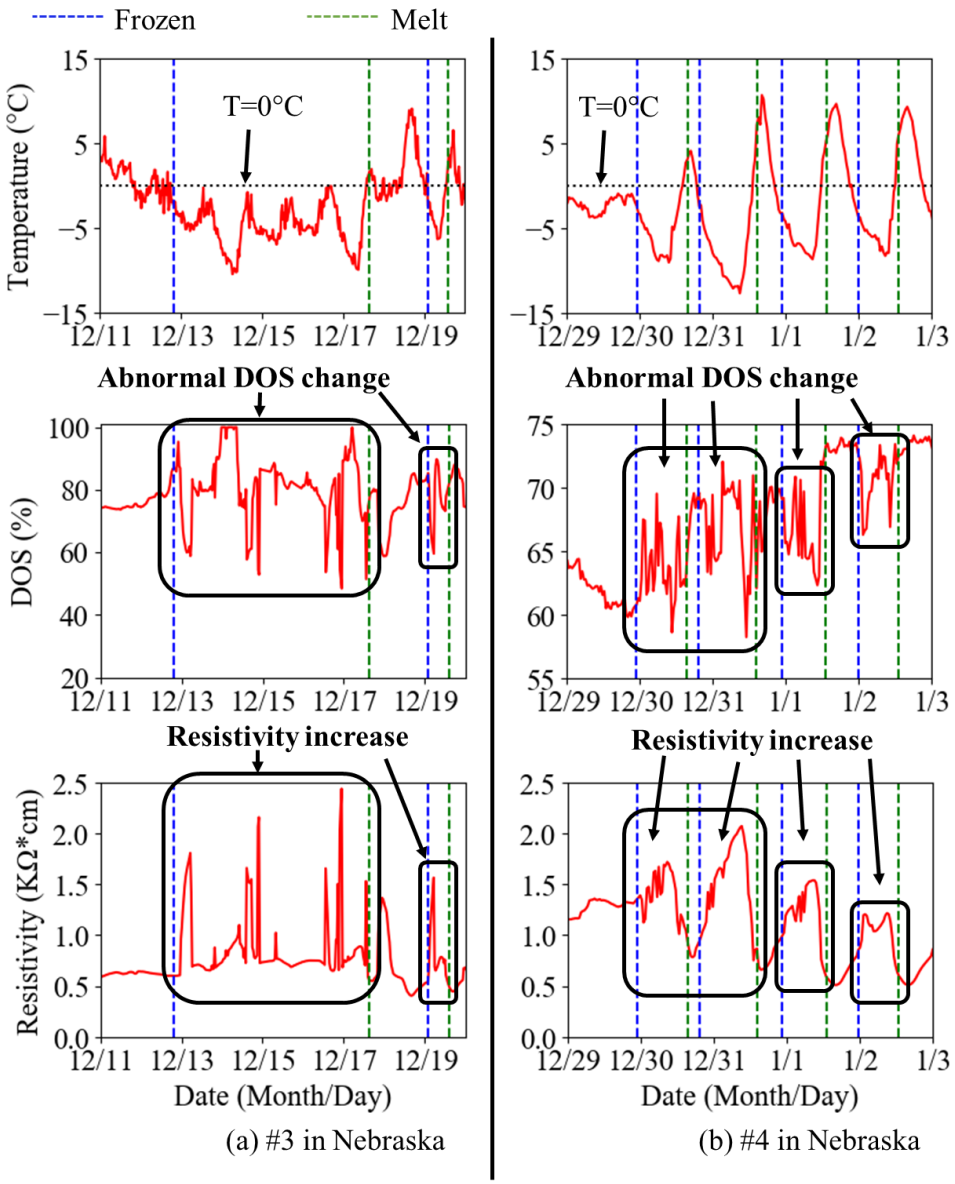

Figure A. 8. Temperature, DOS, and resistivity curve within the freeze-thaw cycles detection at 13mm depth of the field samples in locations #3 and #4 in Table 5-4.

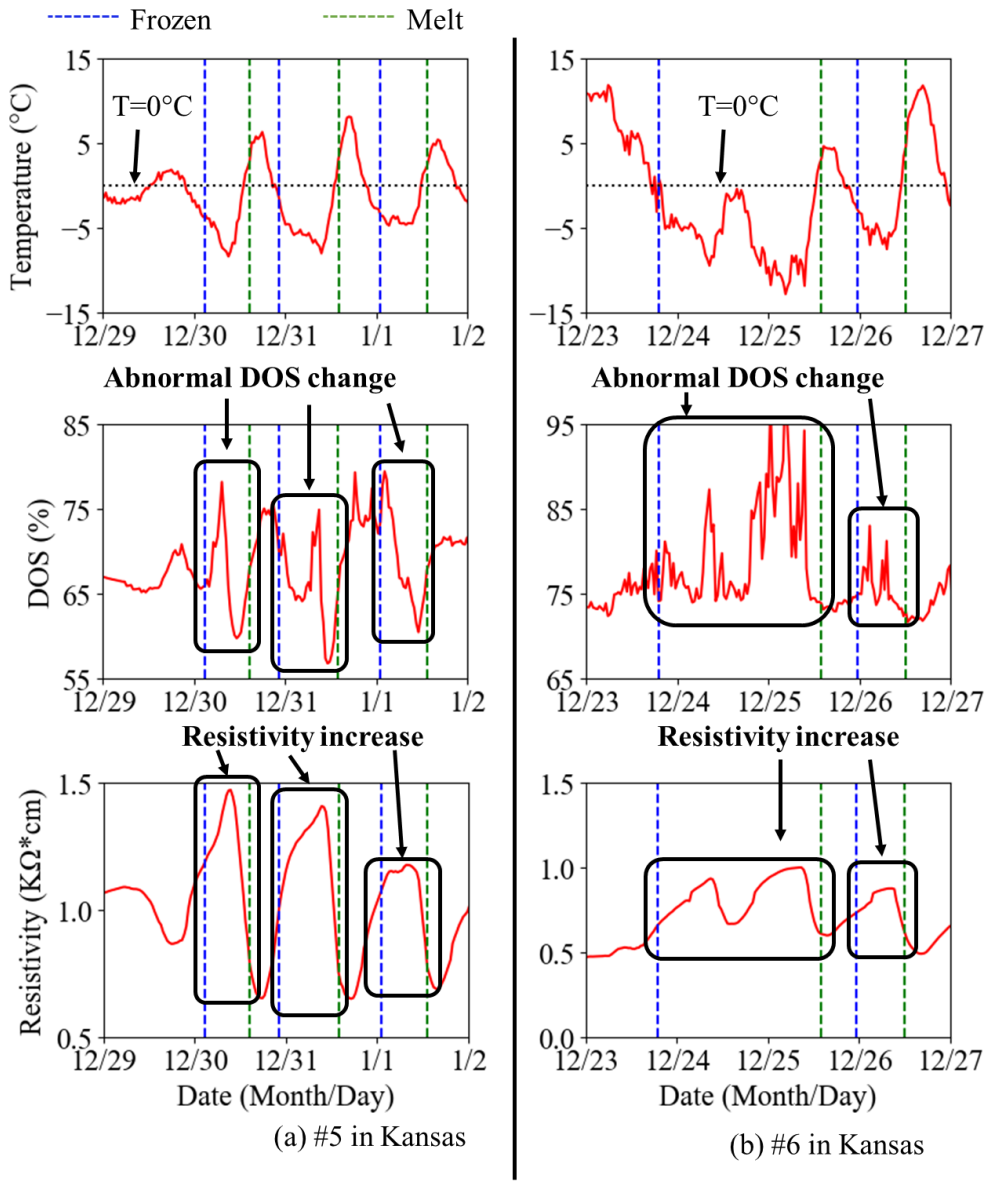

Figure A. 9. Temperature, DOS, and resistivity curve within the freeze-thaw cycles detection at 13mm depth of the field samples in locations #5 and #6 in Table 5-4.

VITA

Lichun Chen

Candidate for the Degree of

Doctor of Philosophy

Dissertation: NOVEL METHODS OF QUANTIFYING CURING INFLUENCE AND FREEZE THAW CYCLES IN THE FIELD

Major Field: Civil Engineering

Biographical:

Education:

Completed the requirements for the Doctor of Philosophy in Civil Engineering at Oklahoma State University, Stillwater, Oklahoma in May, 2022.

Completed the requirements for the Master of Engineering in Civil Engineering at Shanghai Jiao Tong University, Shanghai, China in 2016.

Completed the requirements for the Bachelor of Science in Civil Engineering at Shanghai Jiao Tong University, Shanghai, China in 2013.